IDENTIFICATION OF THE VISCOUS SUPERLAYER ON THE LOW SPEED SIDE OF A SINGLE STREAM SHEAR LAYER

By

Jason Anthony Peabody

A THESIS

Submitted to
Michigan State University
in partial fulfillment of the requirements
for the degree of

MASTER OF SCIENCE

Mechanical Engineering

2010

ABSTRACT

IDENTIFICATION OF THE VISCOUS SUPERLAYER ON THE LOW SPEED SIDE OF A SINGLE STREAM SHEAR LAYER

By

Jason Anthony Peabody

Image pairs (elevation/plan views) have been acquired of a smoke streakline originating in the irrotational region on the low-speed side of the high Re single-stream shear layer of Morris and Foss (2003a). The viscous superlayer (VSL) is identified as the terminus of the streak; 1800 such images provide VSL position statistics. Hot-wire data acquired concurrently at the shear layer edge and interior are used to investigate the relationship between these velocity magnitudes and the large-scale motions. Distinctive features (plumes) along the streakline are tracked between images to provide discrete irrotational region velocity magnitudes and material trajectories. A non-diffusive marker, introduced in the separating (high speed) boundary layer and imaged at $x/\theta_o = 351.6$, has revealed an unexpected bias in the streak-defined VSL locations. The interpretation of this bias clarifies the induced flow patterns in the entrainment region. The observations are consistent with a conception of the large-scale shear layer motions as “billows” of vortical fluid separated by re-entrant “wedges” of irrotational fluid, per Phillips (1972).

TABLE OF CONTENTS

LIST OF FIGURES

KEY TO SYMBOLS OR ABBREVIATIONS

η ....Dimensionless transverse coordinate of shear layer.

x, y, z ....Streamwise, transverse and span-wise (respectively) lab coordinates.

$y_{1/2}$ .... Transverse location at which streamwise velocity is 1/2 its free-stream value.

θ ....Local momentum thickness of shear layer.

U_o ....Free-stream velocity.

$\bar{U}, \bar{V}$ ....Time-averaged velocity components in x and y directions.

L ....Length of "soda-straw" flow-conditioning elements.

$\langle U \rangle, \langle V \rangle, \langle W \rangle$ ....Ensemble-averaged velocity components in x, y and z-directions.

D ....Diameter of "soda-straw" flow-conditioning elements.

θ_o ....Momentum thickness of separating boundary layer at $x = 0$.

Re_D ....Reynolds number of incense stick mounting wire, based on its diameter.

Re_θ ....Reynolds number based on momentum thickness.

u_τ ....Friction velocity.

C_f..............................Skin friction coefficient.

ρ ....Density of air.

υ ....Kinematic viscosity of air.

τ_{wall} ....Shear stress at wall.

u^+ ....Streamwise velocity component in boundary layer, normalized by friction velocity.

y^+ ....Transverse coordinate as normalized by "inner scales" of boundary layer.

V_e ....Mean velocity of entrainment flow on low-speed side of shear layer.

U, V, W ....Velocity components in x, y and z.

t ....Time.

Q ....Velocity magnitude in x, y plane.

$\vec{\omega}$ ....Vorticity vector.

$\vec{U}$ ....Velocity vector, with components U, V, W.

Δ ....Difference or change in a quantity.

ω_z ....Vorticity component in z-direction.

I ....Intermittency function.

$\bar{I}$ ....Intermittency factor.

D_w, L_w ....Diameter and length of "active" region of hot-wire sensor.

Q_{ref} ....Reference velocity used in calibration of hot-wire.

V_B ...."Bernoulli" velocity determined from measurement of a differential pressure assuming negligible viscous effects.

p ....Pressure.

R ....Ideal gas constant of air.

p_{atm} ....Atmospheric (barometric) pressure.

T_a ....Ambient temperature.

Q_{post}, Q_{pre} ....Velocity magnitudes indicated using pre-calibration and post-calibration of hot-wire, respectively.

γ ....Flow angle in x, y plane.

E ....Bridge voltage of hot-wire anemometer.

n ....Exponent used in hot-wire calibrations.

Q_{ind} ....Velocity magnitude indicated by calibrated hot-wire.

T_s ....Temperature of hot-wire sensor.

$\hat{E}$ ....Temperature-compensated bridge voltage of hot-wire anemometer.

E_a, E_b ....Bridge voltages associated with inclined sensors in the x-array.

Q_a, Q_b ....Velocity magnitudes indicated by inclined sensors in the x-array.

Q_x ....Velocity magnitude jointly indicated by both sensors in the x-array.

E_1, E_2 ....Bridge voltages associated with straight sensors in the vorticity probe.

Q_1, Q_2 ....Velocity magnitudes indicated by straight sensors in the vorticity probe.

Q_{conv} ....Convective velocity used to define contributions to the length of micro-circulation domain.

$Q^{d, e}$ ....Velocity magnitude interpolated in-between samples d and e.

$\delta S^{d, e}$ ....Convected distance in-between samples d and e.

f_s ....Sampling frequency.

U_1, U_2 ....Streamwise velocity components indicated by straight sensors in the vorticity probe.

$U^{d,e}$ ....Streamwise velocity component interpolated in-between samples d and e.

U_{conv} ....Convective velocity used to define contributions to the streamwise length of the micro-circulation domain.

$\delta x^{d,e}$ ....Convected streamwise distance in-between samples d and e.

N ....Number of samples in complete micro-circulation domain.

Δy ....Separation between straight sensors in the vorticity probe.

ΔS ....Length of completed micro-circulation domain.

Δx ....Streamwise length of completed micro-circulation domain.

Γ ....Circulation around micro-circulation domain.

$\vec{V}$ ....Velocity vector in (x, y) plane.

$\hat{\mathbf{i}}, \hat{\mathbf{j}}, \hat{\mathbf{k}}$ ....Unit vectors in (x, y, z) coordinate directions.

$\vec{s}$ ....Unit vector tangent to curve defining micro-circulation domain and traversing it in counter-clockwise direction.

V_1, V_2 ....y-direction velocity components indicated by the straight sensors in the vorticity probe.

V^h ....y-direction velocity component at sample h.

A ....Area of micro-circulation domain.

$\underline{\omega}_z$ ....Value of ω_z averaged over the area of the micro-circulation domain.

U_{max} ....Maximum expected velocity in data record.

f_s^{min} ....Minimum sampling frequency required to ensure that aspect ratio of micro-circulation domains is ~1.

σ ....Moving RMS of vorticity time series.

z_k ....z-location of kth calibration image for vertical camera.

x_k, y_k ....Indicated x and y location for a given point identified using kth calibration image.

t_o ....Time of acquisition of image.

t_1 ....Time of acquisition of previous image.

t_{-1} ....Time of acquisition of next image.

$\vec{x}$ ....Position vector of plume.

η_{WF} ....Dimensionless transverse coordinate of Wygnanski and Fiedler.

x_o ....Virtual origin of shear layer used to form η_{WF}.

η_{VSL} ....Dimensionless transverse location of VSL.

$\vec{\nabla}$ ....Gradient operator, $\frac{\delta}{\delta x}\hat{\mathbf{i}} + \frac{\delta}{\delta y}\hat{\mathbf{j}} + \frac{\delta}{\delta z}\hat{\mathbf{k}}$.

$R_{\alpha\alpha}$ ....Auto-correlation function for quantity $\alpha(t)$.

$R_{\alpha\beta}$ ....Cross-correlation function for quantities $\alpha(t)$ and $\beta(t)$.

τ_{peak}^{auto} ....Time-lag to first peak of auto-correlation function

τ_{peak}^{cross} ....Time-lag to first peak of cross-correlation function

f_m ....Characteristic frequency of large-scale motions.

St ....Strouhal number.

U_c ....Convective velocity of large-scale motions.

1.0 Introduction

1.1 Motivation

The present study was undertaken in order to identify the instantaneous location of the viscous superlayer (VSL) on the low speed side of a single-stream shear layer. The VSL represents a thin boundary between vortical (turbulent) and non-vortical fluid. Measurement of its instantaneous location is difficult since its location varies in a random-like fashion over a spatial extent that is many times its actual thickness. Hot-wire based methods for determining the intermittency function:

$$I(t) = \begin{cases} 0 \text{ if flow is non-vortical at time } t \\ 1 \text{ if flow is vortical at time } t \end{cases} \qquad \textbf{1.1}$$

can be used to infer when the VSL has passed the location of the sensor, but these methods cannot be reliably employed in regions of the flow where the velocity fluctuations are larger than their mean value. In such regions, the directional insensitivity of a hot-wire sensor renders multi-sensor arrays useless, and a method for reliably discriminating between vortical and non-vortical fluid based on measurements from a single-sensor probe has yet to be determined.

Particle image velocimetry (PIV) cannot be used in the present facility owing both to its large spatial scale and to the extensive flow conditioning that has been provided for the entrainment fluid stream (discussed in Section 2.0). The large spatial scale makes it difficult to obtain sufficient intensity of the light scattered by the seeding particles. The seeding particles are also widely dispersed by the time they arrive at the measurement region from their point of introduction to the flow. Due to the volume of entrainment fluid which requires seeding, the disturbances introduced by the seeding process would be significant, and would compromise the "pristine" $\vec{\omega} = 0$ condition that is provided by the extensive flow conditioning on this fluid stream. Seeding upstream of this flow conditioning would result in its becoming clogged.

For the present study, a method was developed for determining the instantaneous VSL location by imaging the smoke streakline from a stick of incense using two synchronized cameras. This introduces minimal disturbance into the flow.

1.2 Description of the VSL

A "free" turbulent flow is one in which a region of turbulent fluid is bounded, at least in part, by a region of non-turbulent fluid. Canonical examples of free, turbulent shear flows include jets, wakes and shear layers. When the bounding non-turbulent fluid can be considered irrotational (non-vortical), by necessity a viscous superlayer (VSL) is indicated at the interface between it and the turbulent (vortical) fluid. This feature was first proposed by Corrsin (1943). The term "superlayer" implies that it has a counterpart in the viscous sublayer that exists very near the solid boundary in a turbulent boundary layer. Indeed, both are regions, albeit small, in which viscosity plays the dominant role in the transport of vorticity within the material. Bisset, Hunt and Rogers (2002) emphasize that the VSL is only the outermost part of the turbulent/non-turbulent interface, which is itself a turbulent layer of fluid that is statistically distinguishable from the turbulent fluid in its interior.

The location of the VSL is understood to be a continuous function of space and time, though highly unsteady and "random-like". Phillips (1972) predicted analytically that the VSL should tend to exhibit distinctive large scale features, namely rounded "billows" where it extends into the region of non-vortical fluid and sharp "wedges" where it tends to extend into the region of vortical fluid. This conception of the VSL "topography" is considered below.

1.3 Entrainment

Closely related to the concept of the VSL is the concept of entrainment, whereby fluid from the bounding non-vortical regions is incorporated into the region of mean shear occupied by the vortical fluid. This process of recruitment is associated with a significant change in the recruited fluid's streamwise momentum when compared to an initial state far from the vortical region. In a laminar shear flow, the process may be understood as a simple "dragging along" of the non-vortical fluid, i.e. the momentum is transferred to/from the non-vortical fluid strictly by viscous diffusion. In a fully turbulent shear flow, however, the transfer of streamwise momentum from or to the bounding fluid need not be viscous, although it can be expected that fluid drawn into the region of mean shear will eventually be acted on by viscosity via the VSL.

Dimotakis and Brown (1976) acquired images from a flow-visualization in a two stream shear layer which strongly implied that entrainment in a turbulent shear layer is driven by the large motions and that diffusion of vorticity into this fluid generally occurs after it is well "involved" in the shear layer. Dimotakis (1986) obtained a simple analytical result for shear layers that accurately predicted the ratio of entrainment rates from the two non-vortical streams for a number of experimental studies that were performed at different velocity and density ratios. His analysis was based on a shear layer model using only a simplified representation of the large structures and their spacing in the streamwise direction, further underscoring the importance of large-scale motions with respect to entrainment in the shear layer.

1.4 The Single Stream Shear Layer

The subject flow for this study is a single-stream shear layer. This flow has been well-studied by a number of authors since Liepmann and Laufer (1947) performed their seminal study. Wygnanski and Fiedler (1970) were the first to address the subject of the turbulent/non-turbulent interface in this flow by incorporating measurements that were conditionally sampled based on the value of the intermittency function.

The shear-layer is distinctive in that even at high Reynolds numbers, organized large scale motions can be observed with correlation length scales that are significantly longer in the span-wise direction of the flow than in the transverse direction. This has been confirmed in studies by e.g. Browand and Trout (1980) as well as numerous others. These motions tend to dominate the movement of the VSL and, as noted earlier, appear to be responsible for driving the process of entrainment as well.

The shear layer facility used in this study is distinctive in its scale (9.75 m long test section, 2 m span-wise extent), so that concerns regarding probe interference and spatial resolution are minimized. Also distinctive is the fact that both streams of bounding non-vortical fluid are heavily conditioned to remove disturbances and allowed to "settle" for relatively long times before reaching the test section. These long settling times allow smaller scales of free-stream turbulence to decay so that the flow reaches the test section in a "pristine" non-vortical condition.

The self-similarity of the flow in this facility has already been well-documented by Morris (2002) and Hellum (2006). Non-dimensional data from differing streamwise locations can be seen to collapse onto the "similarity variable," η; see Figure 1.1.

$$\eta \equiv \frac{y - y_{1/2}(x)}{\theta(x)} . \qquad \textbf{1.2}$$

Here, $y_{1/2}(x)$ is the tranverse location at which the streamwise velocity component is equal to half its free-stream value and $\theta(x)$ is the local momentum thickness, defined as:

$$\theta(x) = \int_{-\infty}^{\infty} \frac{\overline{U}(x,y)}{U_o}\left(1 - \frac{\overline{U}(x,y)}{U_o}\right) dy \quad . \qquad \textbf{1.3}$$

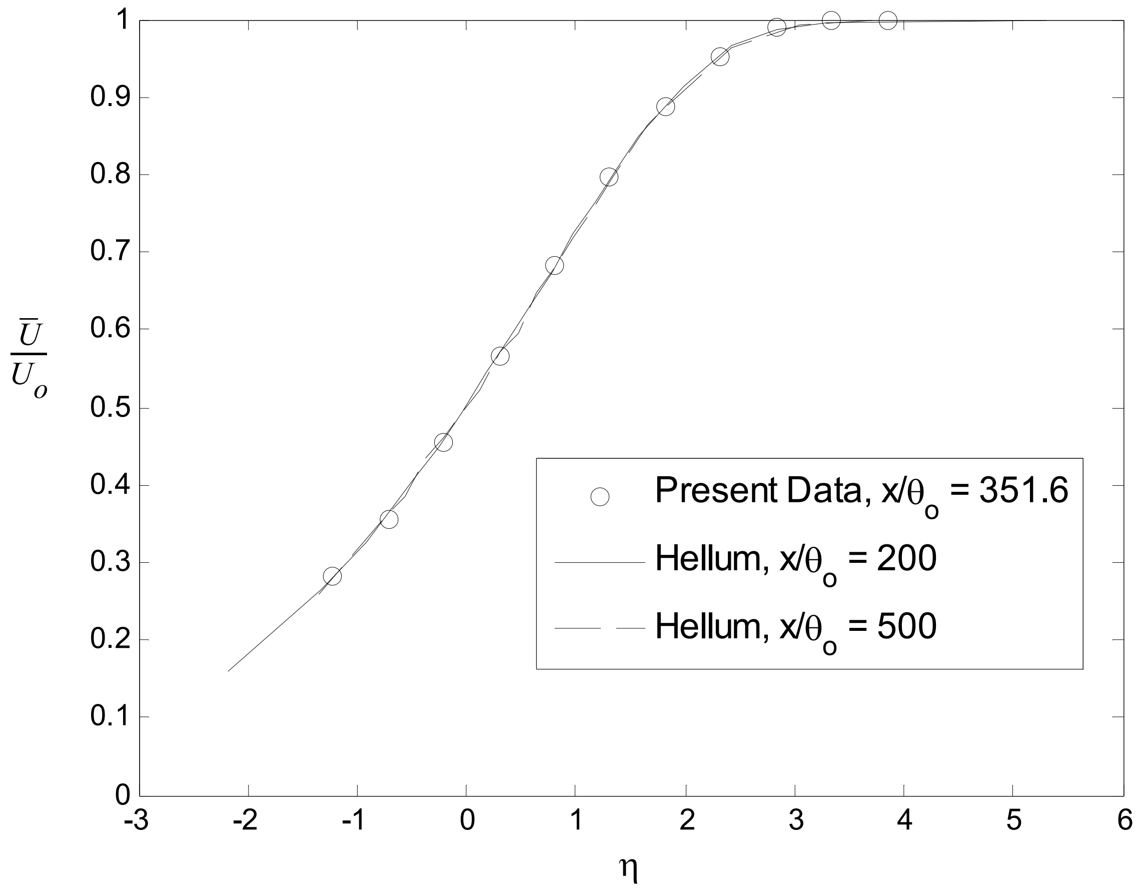

Figure 1.1 Self-Similarity of the mean velocity profile at different streamwise locations.

2.0 Experimental Setup and Procedure

2.1 Facility

Experiments were carried out in the large single stream shear layer (SSSL) facility, located in the Turbulent Shear Flows Lab at Michigan State University; see Morris and Foss (2003a) for its description. This facility delivers two distinct streams of fluid, designated as the “primary flow” and the “entrainment flow,” to the test section. Figure 2.1 provides its schematic representation. The primary flow is labelled “1” and the entrainment flow is labelled “2.” The working fluid is air that is ingested from the laboratory. In the chosen coordinate system, x is designated as the streamwise direction, y as the transverse direction, and z as the span-wise direction. Note that the positive z-direction is downward, i.e. in the direction of gravity.

2.1.1 Primary Flow

Air for the primary flow is ingested from the laboratory by a large $(\text{diameter} = 1.0 \text{ m})$, axial fan at ground level and delivered to a horizontal, 2 m x 2 m flow passage. It is then passed through two sets of 90-degree turning vanes. The first set directs the flow vertically upwards and the second set directs it horizontally again, opposite its original direction, at a centerline distance of 3.1 m above ground level. Furnace filters are mounted just upstream of the first set of turning vanes in order to smooth the highly non-uniform velocity profile from the fan and to capture any dust ingested from the laboratory; see Figure 2.2.

After the second set of turning vanes, the flow corresponds to the “primary inflow” indicated in Figure 2.1. It passes though a 2 m x 2 m panel of “honeycomb” flow conditioning to remove the large-scale motions. The honeycomb is made of short lengths of “soda straws” whose sides have been pressed together. The straws have a length, *L*, of 2.54 cm in the direction of the flow and diameter, *D*, such that $L/D = 8$. Following this are three sheets of stretched steel wire mesh, spaced 10.4 cm apart in the direction of the flow. The mesh has a wire spacing of 0.76 mm and an open area of 80%.

The flow is then accelerated through a contraction that reduces the width of the passage from 2 m to 1.1 m; see Figure 2.3. The boundary layer that forms on the curved wall of the contraction is discarded by splitting the flow with a plate and returning the boundary-layer fluid to the laboratory. The boundary layer surface that leads to the test section is fitted with an elliptical leading-edge in order to minimize any flow disturbance, and a new boundary layer develops along its length. This new boundary layer is tripped 30 cm downstream of the elliptical leading edge by a 3/4” strip of velcro tape around the perimeter of the flow passage. The trip is to ensure a consistent transition location for the turbulent boundary layer.

The free-stream velocity of the primary flow at separation, U_o, is approximately 7.5 m/s. The pressure difference between a tap located in the upstream portion of the contraction and a tap located at the separation plane $(x = 0)$ was calibrated against the velocity indicated by a sharp-edged stagnation probe located in the primary fluid so that U_o could be monitored with every experiment. Variations in U_o were within 1% over an 8-month period.

The separating boundary layer is fully turbulent, with a momentum thickness of $\theta_o = 11.0\ \mathrm{mm}$. This value is somewhat larger than the value of 9.96 mm obtained by Hellum (2006) in this same facility. This difference may be a result of upgrades that were made to the construction of the contraction. Specifically, the contraction used by Hellum was constructed of linoleum flooring material that was stapled to wooden support members, and it was observed to vibrate substantially during tunnel operation. The linoleum was therefore replaced by more rigid particle board (thickness = 0.125 in.) for this study. The particle board was bent to shape over the support members and fastened using screws and silicone adhesive. This assembly did not vibrate noticeably during tunnel operation.

The momentum thickness was determined by forming the momentum thickness integrand:

$$\left(\frac{\bar{U}}{U_o}\right)\left(1-\frac{\bar{U}}{U_o}\right). \qquad \mathbf{2.1}$$

See Figure 2.4. As the free-stream velocity appears mildly non-uniform at the edge of the boundary layer, U_o was defined by averging the values of $\bar{U}$ obtained at the 7 highest velocity locations; a similar technique was employed by Hellum (2006). The profile was then integrated using “trapezoidal” integration, i.e. the data points were treated as if connected by straight line segments. The Reynolds number of the separating boundary layer, based on the momentum thickness, is $Re_\theta = 5470$.

The friction velocity, u_τ, was determined using a correlation between Re_θ and the friction factor,

$$C_f \equiv \frac{2\tau_{wall}}{\rho U_o^2} = 2\left(\frac{u_\tau}{U_o}\right)^2 \qquad \mathbf{2.2}$$

that was obtained from Johnson (1998). In Equation 2.2, τ_{wall} is the wall shear stress.

The mean velocity profile, when represented in "wall coordinates" $u^+ \equiv \overline{U}/u_\tau$ and $y^+ \equiv (yu_\tau)/\upsilon$, agrees very well with that for a classical zero-pressure-gradient, flat-plate turbulent boundary layer; see Figure 2.5. The standard fit for the "log region" is also shown:

$$u^+ = 2.44\log(y^+) + 4.9. \qquad \textbf{2.3}$$

2.1.2 Entrainment Flow

Air for the entrainment flow is ingested by four large axial fans mounted at the same height as the test section. Each fan exists within its own enclosure, and delivers the air through a layer of quilt batting to a common "mixing plenum." This air is then passed through a panel of honeycomb flow conditioning and three sets of steel mesh screens, identical to those used for the primary flow. The entrainment fans were driven by 4 synchronous AC motors, all driven by a single AC motor controller with variable drive frequency to control their speed. The fans' speed was set to provide a mean entrainment velocity, V_e, equal to $0.035U_o$. This value for V_e has been indicated in a number of zero-pressure-gradient single stream shear-layer studies, notably Morris (2002), Ali (1985) and Champagne et al. (1976).

V_e was set by measuring the entrainment velocity magnitude with an array of 4 single hot-wire probes such as the one shown in Figure 2.7. The probes were located at x = 2, 3, 4 and 5 m with their sensor axes oriented parallel to the z-direction, about 10 cm downstream of the final mesh screen; see Figure 2.6. The speed of the entrainment fans was varied over a wide-enough range to include the desired operating condition. This was done three times, with the sensors positioned at 25%, 50% and 75% of the span-wise (z-direction) extent of the facility. It is worth noting that the entrainment velocity was quite uniform over the area measured for each fan setting.

2.2 Overview of Experimental Measurements

Time series measurements were obtained of the x and y velocity components, $U(t)$ and $V(t)$; their joint magnitude, $Q(t) = \sqrt{U(t)^2 + V(t)^2}$; and span-wise vorticity, $\omega_z(t)$ using constant-temperature hot-wire anemometry (CTA). A traverse was performed in the y-direction at the streamwise location: $x/\theta_o = 351.6$. The measurements of $\omega_z(t)$ were additionally used to form the intermittency function, where the presence of ω_z above a threshold signifies $I = 1$ and its absence is registered as $I = 0$.

The instantaneous location of the VSL was measured by imaging a smoke streakline using two cameras; the technique is described in sections 2.4.1 through 2.4.5. The measurements were made in the domain: $320.4 \le x/\theta_o \le 382.7$, $-91.5 \le y/\theta_o \le -15.6$. Note that the hot-wire traverse described above was performed at the streamwise center of this domain. The y-range corresponds to $-5.91 \le \eta \le -0.35$ at this location. Hot-wire measurements were also made concurrently with these data and are described in Section 2.4.6.

A measurement was also made to determine the maximal extent to which a non-diffusive quantity would spread into the entrainment region. This measurement was made by introducing theatrical "fog" into the primary fluid and directing a laser beam across the shear layer. A single camera was used to collect images of the laser light that was reflected by the fog. This measurement is described in Section 2.5. This measurement was also made at the streamwise center $(x/\theta_o = 351.6)$ of the VSL location measurement domain.

Additional velocity statistics within the irrotational fluid were obtained by tracking plumes of smoke that would occasionally form along the streakline. These plumes are discussed in Section 2.4.2. They could be followed from image to image in order to provide discrete estimates of the velocity, as well as material trajectories (pathlines).

2.3 Hot-wire Techniques and Processing

2.3.1 Equipment

Disa/Dantec model 55M01 CTA units were used with an overheat resistance ratio of 1.7 for all hot-wire measurements. Single-sensor probes were used for measurements of Q. A four-sensor probe, as shown in Figures 2.8 and 2.9, was used to measure U, V and ω_z. This probe design was originally introduced in Foss and Haw (1990). The coordinate system indicated in Figures 2.8 and 2.9 was aligned with the SSSL coordinate system during measurements.

2.3.1.1 Probe Construction

All hot-wire probes were fabricated in-house, using stainless-steel mounting broaches spaced 3 mm apart. The tips of the broaches were etched with hydrochloric acid and "tinned" with a small amount of solder to facilitate mounting of the sensor wires.

Tungsten sensor wires of diameter $D_w = 5\ \mu\text{m}$ were used. The ends of the sensor wire were plated with copper to a diameter of roughly 50 μm, leaving an unplated "active region" in the middle with nominal length $L_w = 1\ \text{mm}$; see Figure 2.7. This active region is so-called because the copper plating on the sensor ends lowers their electrical resistance by several orders of magnitude, while also increasing their thermal mass. Thus only the unplated central portion of the sensor is brought to an elevated temperature by the anemometer, ensuring that the measured velocities are essentially not contaminated by aerodynamic effects from the broaches to which the sensor is mounted. The copper also allows the sensor to be mounted to the tinned ends of the broaches by soldering. The transient thermal characteristics of such a sensor and their influence on the sensor's frequency response can be found in numerous references. That by Morris and Foss (2003b) is particularly relevant to the present probes.

L_w was occasionally slightly longer than 1 mm but not shorter, providing the condition: $L_w / D_w \geq 200$. This is shown by Champagne et. al (1967) to ensure that a uniform temperature profile exists over part of the active region.

2.3.2 Calibration

Hot-wire calibrations were made in a special "suction-side" calibration facility, shown in Figure 2.10. A small centrifugal fan was used to bring the interior of the facility to a sub-atmospheric pressure, causing air to be induced from the lab environment. The air was delivered through a screen of quilt batting into a plenum made from a piece of PVC pipe with an inner-diameter of 13 cm. It was then delivered to the interior of the calibration facility through a nozzle with an exit diameter of 1.9 cm. The hot-wire sensor array was located at the exit plane of this nozzle. The calibration reference velocity, Q_{ref}, was defined as the “Bernoulli velocity” V_B obtained by measuring the static pressure difference across the nozzle, Δp:

$$Q_{ref} \equiv V_B = \sqrt{\frac{2\Delta p}{\rho}}. \qquad \textbf{2.4}$$

The density of the air, ρ, was determined using the ideal gas law as $\rho = p_{atm}/(RT_a)$, where p_{atm} is the local barometric pressure, R is the ideal gas constant for air, and T_a is the ambient temperature in the calibration facility. T_a was measured with either a thermocouple or an LM34 integrated-circuit temperature sensor. No adjustment was made to p_{atm} to account for the subatmospheric pressure in the facility, but for a typical calibration this pressure difference would be less than 0.06% of p_{atm}.

All calibrations were made under “quasi-steady-state” conditions, in which a single calibration time series is acquired at a given incidence angle while the velocity varies continuously over the calibration range. This was accomplished by means of a motor-controlled gate in the calibration facility that acted as a throttle to vary the calibration velocity; see Figures 2.10 and 2.11. The designation “quasi-steady-state” indicates that the rate-of-change of the calibration velocity is slow enough, relative to the noise and transient response of the transducers, to allow each sample to be considered as occurring at steady-state. The validity of this method has been confirmed by Hellum (2006).

All hot-wire data were acquired by calibrating the sensor immediately before the data set and immediately after the data set, providing “pre” and “post” calibrations. The data were then processed with both the pre and post calibrations, and these were compared in order to assess the effect of sensor "drift." Drift was defined as $\frac{Q_{post} - Q_{pre}}{Q_{pre}} \times 100$,

where Q_{post} is the velocity magnitude obtained using the post calibration, and Q_{pre} is the velocity magnitude obtained using the pre calibration. For all reported hot-wire data, drift was found to be less than 2%; a value of about 1.2% was typical.

2.3.2.1 X-Array and Vorticity Probe Calibration

The four sensors of the vorticity probe are comprised of two parallel "straight" sensors and two "inclined" sensors. The two inclined sensors comprise an "x-array" capable of measuring the velocity magnitude and angle, Q and γ, in the (x, y) plane that is nominally in-between them. U and V are then recovered as $U = Q\cos(\gamma)$ and $V = Q\sin(\gamma)$. Some uncertainty is introduced by the fact that the inclined sensors are not exactly co-planar; they are separated by a distance of approximately 1 mm in the z-direction. The straight sensors' axes are perpendicular to this plane.

The calibration facility was outfitted with a mount, shown in Figure 2.10, that allowed the probe to be accurately positioned at different angles to the approach flow. 13 calibrations were acquired for all four sensors at different values of γ, ranging from -36° to 36° in 6° increments. The chosen range: $-36° \le \gamma \le 36°$ is referred to as the "acceptance cone." Specifically, angles outside this range can not be reliably measured due to the effects of tangential cooling on the inclined sensors. The data processing using these calibrations is described later; see Section 2.3.3.1.

2.3.2.2 Low-Speed Calibrations for Measurement of Entrainment Velocity

Due to the extremely low velocities involved, the hot-wires used to measure V_e could not be calibrated by reference to a "Bernoulli velocity," as the dynamic pressures involved would be too low to measure. Rather, a swinging-arm apparatus was constructed which allowed a probe to be mounted with its sensor at a known distance from the axis of rotation and then swung through quiescent air inside a large box. The relative velocity between the sensor and the air was determined by measuring the angular velocity of the pivot using an optical encoder and multiplying by the distance from the pivot to the sensor. This was used as the reference velocity for the calibration.

2.3.2.3 Calibration Fitting

The hot-wire bridge voltage, E^2, was related to Q as $E^2 = f(Q^n)$. If a linear function is used for f, the "modified King's Law" suggested by Collis and Williams (1959) is recovered with $n = 0.45$. As a further refinement, an iterative process was used to determine the value of n resulting in the smallest RMS error between the fit and the calibration data. This value was typically between 0.40 and 0.45.

It was found, however, that such a linear fit did not always go through the "center" of the E^2 versus Q^n calibration data pairs, especially for the inclined sensors of the x-array. Figures 2.12 and 2.13 show a typical calibration data set obtained for an inclined sensor, with the best fit line shown in white. It can be seen in Figure 2.12 that the calibration data points "wander" around the line of best fit. This is behavior is more apparent in Figure 2.13, which shows the difference between the velocities indicated by the calibrated sensor, Q_{ind}, and the reference velocities, Q_{ref} for each calibration data point. While this is apparent to the eye of an observer, it is difficult to recognize using a processing algorithm. The wandering of the fit always occurs at the lower velocities of the calibration and is worse when the sensor is more parallel to the flow, suggesting that it may be a result of the very low velocity component normal to the sensor.

This calibration behavior was determined to be a contributing factor to anomalous behavior in the time series of γ that were obtained from the x-array. Namely, it was observed that γ was not correctly predicted when the calibration time series (taken at a known value of γ) were processed as decribed in Section 2.3.3.1. Figure 2.14 shows time series of Q and γ measured by the calibrated x-array, with γ fixed at -18º in the calibration facility. The systematic "wandering" of the measured γ about its actual value is clear for Q below approximately 2 m/s in this case, and in other cases was apparent at velocities as high as 4 m/s.

Instead of using a linear function for $E^2 = f(Q^n)$, a 5th-order polynomial was used to try to mitigate the wandering behavior of the fit for calibrations of the inclined sensors. This was shown to work well, as indicated by Figures 2.15, 2.16 and 2.17. These three figures represent the same calibration data as Figures 2.12, 2.13 and 2.14, respectively. It can be seen that γ is now well-predicted down to approximately 0.9 m/s. It should be noted that the polynomial calibration did not always eliminate the wandering behavior of the calibrations, but it did greatly improve most of them, and did not make any of them worse.

2.3.2.4 Temperature Compensation

All hot-wire data were corrected to account for variation in the ambient temperature of the fluid, T_a, by using a simple "linear" correction similar to that described in Abdel-Rahman *et al* (1987). At a fixed velocity, and for a fixed sensor temperature T_s, E^2 is assumed to vary linearly with $T_s - T_a$. This assumption is valid provided that variations in T_a are not large enough to cause substantial changes in the fluid properties, i.e. it is equivalent to assuming a constant convective heat transfer coefficient for the sensor at a fixed velocity. Variations in T_a can therefore be corrected by scaling the bridge voltage as $\frac{E^2}{T_s - T_a} \equiv \hat{E}^2$ for calibration and processing.

2.3.2.5 Master-Wire Calibration of Vorticity Probe

Calibration of the vorticity probe was further refined by using a "master wire" calibration scheme. In this scheme, the four sensors of the probe were calibrated as normal against the Bernoulli velocity, V_B. For each of the 13 calibration angles, the straight sensor with the lowest RMS deviation from its calibration fit was designated as the "master wire." The other sensors were then re-calibrated against the velocity measured by the master wire, using its calibration, instead of V_B. Since a hot-wire can respond faster than the pressure transducer that is used to measure Δp, the master wire can better "track" fluctuations in the velocity of the calibration flow. This method thus provides the other sensors in the probe with a more reliable reference velocity. The second benefit derives from the condition that all four sensors are used to determine ω_z. Hence, the master-wire ensures maximal relative agreement of the four voltages.

2.3.3 Processing of X-Array and Vorticity Probe Data

2.3.3.1 X-array Processing

Processing of a datum point from the x-array was carried out as follows: For a given point in the data time series, the two sensors of the x-array provided (temperature-compensated) bridge voltages $\hat{E}_a^2$ and $\hat{E}_b^2$. Each voltage was processed using the 13 calibrations acquired for that sensor. This yielded 13 values of velocity magnitude, Q_a and Q_b, for each sensor at 13 different values of γ. This is shown in Figure 2.18. These (γ, Q_a) and (γ, Q_b) values would describe an increasing curve for one sensor and a decreasing curve for the other. As long as this increase and decrease were monotonic for both curves, their intersection would identify a unique combination of γ and Q, which were then retained as the measured values γ and Q_x. This scheme was introduced by Browne et al. (1989).

To determine where this intersection occurs is identical to determining the value of γ for which the quantity $Q_a(\gamma) - Q_b(\gamma) \equiv \Delta Q(\gamma)$ is equal to zero. Cubic spline fits were determined for $Q_a(\gamma)$ and $Q_b(\gamma)$ over all 13 values of γ, and their coefficients were subtracted from one another to provide a spline describing $\Delta Q(\gamma)$. The zero of this fit was then determined, identifying the measured value of γ. The value of Q_x could then be obtained by evaluating either of the two fits, $Q_a(\gamma)$ or $Q_b(\gamma)$, at the measured value of γ.

If $\Delta Q(\gamma)$ had no zeros in the range $-36° \leq \gamma \leq 36°$, corresponding to a case for where γ lay outside the “acceptance cone” of the array, the point was “flagged” as bad and excluded from the statistics. The percentage of bad points in the time series obtained at each transverse location increased dramatically towards the low-speed side, as more velocities below the calibration range and more flow angles outside the acceptance cone were encountered. These data will be shown in Section 3.

Occasionally it was also found that $\Delta Q(\gamma)$ would have multiple zeros in the range $-36° \leq \gamma \leq 36°$. This was determined to occur when either Q_a, Q_b or both were not monotonic functions of γ, and was typically observed at lower velocities and more extreme angles. For perfectly straight sensors, this would be unexpected in that the velocity component normal to an inclined sensor will be monotonic with γ for any γ within the acceptance cone. This normal velocity component may be roughly regarded as an effective cooling velocity, which is directly related to the bridge voltages, $\hat{E}_a$ and $\hat{E}_b$. However, the active regions of the sensors were seldom perfectly straight, and this may be expected to complicate the directional-sensitivity of their convective heat transfer characteristics, especially for the inclined sensor that is more parallel to the flow. Where multiple zeros were obtained for $\Delta Q(\gamma)$, the point was “flagged” as bad and excluded from statistics.

2.3.3.2 Vorticity Probe Processing

After the determination of Q_x and γ, the x-array of the vorticity probe was no longer used. The calculation of ω_z was carried out using γ and the velocity magnitudes, Q_1 and Q_2, provided by the two straight sensors.

Since the straight sensors are also slightly sensitive to γ, processing of a given straight sensor was carried out as follows: for a given point in the data time series, the (temperature-compensated) squared bridge voltage of the sensor, $\hat{E}_1^2$ or $\hat{E}_2^2$, was processed using the 13 calibrations acquired for that sensor. This yielded 13 values of velocity magnitude for Q_1 and Q_2, at 13 different values of γ. Cubic splines were fit for $Q_1(\gamma)$ and $Q_2(\gamma)$ over all 13 values of γ, and then evaluated at the measured value of γ. Note the assumption that the angle, γ, acts on both straight sensors. This necessary assumption will be made for the remainder of the vorticity processing.

In order to calculate ω_z, it was necessary to first estimate a convected distance in-between adjacent samples in the time series. The following discussion is in reference to Figure 2.19. Consider adjacent samples, d and e. Between these samples, the estimated value of Q_1 was defined as $Q_1^{d,e} = (Q_1^d + Q_1^e)/2$. The value of Q_2 was estimated similarly as $Q_2^{d,e} = (Q_2^d + Q_2^e)/2$. An estimated convection velocity was then formulated as $Q_{conv}^{d,e} = (Q_1^{d,e} + Q_2^{d,e})/2$. Finally, the convected distance between samples d and e was formulated as $\delta S^{d,e} = Q_{conv}^{d,e}/f_s$, where f_s is the sampling frequency.

The convected x-distance between adjacent samples was also needed. For samples d and e, the x-direction velocity components from each sensor, $U_1 = Q_1 \cos\gamma$ and $U_2 = Q_2 \cos\gamma$, were estimated as $U_1^{d,e} = (U_1^d + U_1^e)/2$ and $U_2^{d,e} = (U_2^d + U_2^e)/2$. The x-direction convection velocity was then formulated as $U_{conv}^{d,e} = (U_1^{d,e} + U_2^{d,e})/2$ and the convected x-distance between samples d and e as $\delta x^{d,e} = U_{conv}^{d,e}/f_s$.

Each sample in the time series was used to define the center of a "micro-circulation domain." Each domain was further defined to include the N samples acquired immediately before and after its center sample. The value of N was determined iteratively for each domain, starting with $N = 0$. With each iteration, N was increased by 1 and the domain was expanded to include one more sample on either side of its center sample. This was repeated until ΔS, the sum of the convected lengths between the $2N + 1$ samples, was equal to or greater than the separation between the straight sensors, Δy (nominally 1 mm). The sum of the convected x-distances, Δx, was also calculated for later use. Note that N will be at least 1 for a completed micro-circulation domain, so that all domains will contain at least 3 samples.

The micro-circulation domain can then be concieved of as the region in space that is bounded by $IJKL$ in Figure 2.19. In general this region is shaped like a parallelogram, and more ideally like a rhombus since it is desired that $\Delta S/\Delta y \approx 1$. Each of the 5 black dots represents fluid that currently occupies, has occupied or will occupy the space directly between the straight sensors during the acquisition of the associated samples d, e, f, g and h.

As the name “micro-circulation domain” suggests, ω_z was not determined by directly estimating its velocity-gradient components:

$$\omega_z \equiv \frac{\partial V}{\partial x} - \frac{\partial U}{\partial y} . \qquad \textbf{2.5}$$

Rather, the values of γ, Q_1 and Q_2 associated with the samples that defined each micro-circulation domain were used to estimate the circulation, Γ, around the domain. Stoke’s Theorem can be used to show that Γ is equal to the area of the domain, A_{IJKL}, multiplied by the area-averaged value of ω_z within it:

$$\Gamma = \oint_{IJKL} \vec{V} \bullet d\vec{s} = \iint \omega_z dA_{IJKL} = \underline{\omega_z} A_{IJKL} . \qquad \textbf{2.6}$$

In Equation 2.6, $\vec{V} = U\hat{\mathbf{i}} + V\hat{\mathbf{j}}$ is the “in-plane” velocity vector with x and y-direction unit vectors $\hat{\mathbf{i}}$ and $\hat{\mathbf{j}}$, respectively. $\vec{s}$ is the unit vector tangent to the boundary of $IJKL$ and traversing it counter-clockwise. Note that $|\vec{V}| = Q$.

The analysis that follows makes use of the micro-circulation domain depicted in Figure 2.19. Specifically, $N = 2$ so that the domain is defined by 5 samples, designated d, e, f, g and h. The analysis may be generalized for domains containing more or fewer samples.

As previously discussed, both straight sensors are considered to be exposed to the same flow angle, γ. Since they are also represented by a common convection velocity, the individual line segments that comprise JK and LI are parallel and of the same length.

The contribution to Γ from $\oint_{JK} \vec{V} \bullet d\vec{s}$ was approximated as $\sum_{* = d, e}^{g, h} (Q_1^* \times \delta S^*)$ [1]. Similarly, the contribution from $\oint_{LI} \vec{V} \bullet d\vec{s}$ was approximated as $\sum_{* = d, e}^{g, h} (Q_2^* \times -\delta S^*)$. The negative sign indicates that the velocity vector, $\vec{V}$ and the unit vector $d\vec{s}$ point in opposite directions along JK.

The contribution to Γ from $\oint_{KL} \vec{V} \bullet d\vec{s}$ was approximated as $V^h \times \Delta y$. V^h is the average of V_1^h and V_2^h, the y-direction velocity components provided by sensors 1 and 2 at sample h. Similarly, the contribution to Γ from $\oint_{IJ} \vec{V} \bullet d\vec{s}$ was approximated as $V^d \times -\Delta y$. Note again the negative sign, indicating that $\vec{V}$ and $d\vec{s}$ point in opposite directions along $.IJ$

1. The summation is made over the values that were interpolated in-between the samples, as discussed on page 20. The first term is $Q_1^{d, e} \times \delta S^{d, e}$, in-between samples d and e. The second term is $Q_1^{e,f} \times \delta S^{e,f}$, in-between samples e and f, and so on. The last term is $Q_1^{g, h} \times \delta S^{g, h}$.

These contributions to Γ were summed together and divided by the area of the micro-circulation domain, $A_{IJKL} = \Delta x \times \Delta y$, to yield $\underline{\omega_z}$. This operation can be written out as:

$$\underline{\omega_z} = \frac{[V^h - V^d] \times \Delta y + \sum_{* = d, e}^{g, h} ([Q_1^* - Q_2^*] \times \delta S^*)}{\Delta x \times \Delta y} \qquad \textbf{2.7}$$

and re-arranged to yield:

$$\underline{\omega_z} = \frac{V^h - V^d}{\Delta x} - \frac{\frac{1}{\Delta x} \times \sum_{* = d, e}^{g, h} ([Q_2^* - Q_1^*] \times \delta S^*)}{\Delta y}. \qquad \textbf{2.8}$$

Note that in the second term on the right-hand side of Equation 2.8, the Δx term is represented in the numerator. Recognizing that $\frac{1}{\Delta x} \times \sum_{* = d, e}^{g, h} \delta S^* = \frac{\Delta S}{\Delta x} \approx 1$, one may note that the two terms on the right-hand side of Equation 2.8 are similar to the spatial derivatives, $\frac{\partial V}{\partial x}$ and $\frac{\partial U}{\partial y}$, from the definition of ω_z given in Equation 2.5. For this reason, they are referred to as "the $\frac{\partial V}{\partial x}$ term" and "the $\frac{\partial U}{\partial y}$ term" when discussing the vorticity data in more detail.

Note that if a domain with the minimum of 3 samples is to satisfy the requirement that $\Delta S \approx \Delta y$, the maximum expected velocity in the experiment, U_{max}, implies a minimum sampling frequency, $f_s^{min} = \frac{3U_{max}}{\Delta y}$. Taking $U_{max} = U_o = 7.5$ m/s and using the nominal value $\Delta y = 1$ mm, the indicated value for f_s^{min} is 22.5 kHz. The present value, 20 kHz, was used based on earlier studies in this facility and only allows for 2.66 samples/mm in the high-speed fluid. For this reason, domains formed on the high-speed side of the shear layer may be expected to be somewhat elongated in the streamwise direction. This is not expected to influence the measurement results significantly.

2.3.3.3 Determination of Δy for Vorticity Probe

The separation between the straight sensors of the vorticity probe, Δy, is important for accurate determination of the vorticity. Nominally Δy is equal to 1 mm, which is the spacing between the mounting broaches for the straight sensors. The manner in which the sensors are mounted, however, can change this quantity by a significant percentage. In order to obtain an accurate value for Δy, the probe was traversed across the steep mean-velocity gradient on one side of a small slit-jet, just downstream from the opening. The axes of the straight sensors were oriented normal to the direction of traverse. The mean velocity profiles measured by each sensor were plotted as a function of the distance traversed, and the separation between the curves provided the value of Δy for that probe. See Figure 2.20 for a depiction of this.

The probe used in this study had a value of Δy equal to 0.65 mm. Note that this is significantly smaller than the nominal value of 1 mm, and illustrates the position variation that is possible for a mounted hot-wire sensor.

2.3.4 Determination of Intermittency Function

The intermittency function, $I(t)$, is a binary-valued function defined so that $I = 0$ if the fluid is irrotational, and $I = 1$ if the fluid is vortical. The "activity intermittency" employed by Hellum and Foss (2007) was used in this study. In this method, the "moving RMS" of the vorticity time series is defined as:

$$\sigma(t) = \sqrt{\frac{1}{2\Delta t}\int_{(t-\Delta t)}^{(t+\Delta t)} (\omega_z(\tau) - \bar{\omega}_{z,m}(\tau))^2 d\tau} \qquad \textbf{2.9}$$

where

$$\bar{\omega}_{z,m}(t) \equiv \frac{1}{2\Delta t}\int_{(t-\Delta t)}^{(t+\Delta t)} \omega_z(\tau) d\tau . \qquad \textbf{2.10}$$

The flow is designated as "vortical" if $\sigma(t)$ is greater than some threshold value. The value of Δt was chosen to be equal to the transverse Taylor microscale at the shear layer center $(\eta = 0)$ for consistency with Hellum and Foss (2007). The threshold was determined using $\sigma(t)$ obtained in the predominantly irrotational fluid on the high-speed side of the shear layer $(\eta = 3.85)$. Turbulent bursts at this location were rare and were manually removed by visual inspection of the time series. The PDF of $\sigma(t)$ was then examined and the threshold set at $36\mathrm{s}^{-1}$. Note that in irrotational fluid $\omega_z(t) = 0$ always, by definition, so that $\sigma(t) = 0$ always as well. The value: $\sigma = 36\mathrm{s}^{-1}$ is the lowest value of σ that can reliably be measured, and represents the combined effects of residual, small scale vortical motions in the primary fluid and electrical noise in the hot-wire probe and anemometer circuitry.

A "dwell time" was also implemented for the $I(t)$ signal, requiring that a transition from one state to the other persist for some minimum period of time in order to be valid. This ensures that "false positives" do not occur. The dwell time was chosen to be twice the local transverse Taylor microscale, again for consistency with Hellum and Foss (2007).

2.3.5 Calculation of Shear Layer Momentum Thickness and $y_{1/2}$

The hot-wire data acquired at $x/\theta_o = 351.6$ were used to determine $y_{1/2}$ and θ at this location so that the VSL location data could be expressed in terms of the similarity coordinate, η; see Section 1.4. The value of θ was determined to be 15.02 cm, and $y_{1/2}$ was determined to be -11.92 cm at this location.

The value of $y_{1/2}$ was determined by linearly interpolating in-between the two values of $\overline{U}/U_o$ bracketing the condition: $\overline{U}/U_o = 0.5$. The value of θ was determined by first calculating the momentum-thickness integrand (Equation 2.1) for y-locations where $\overline{U}/U_o > 0.25$. It was judged that the mean value of $\overline{U}$ could not be reliably measured by the x-array below this value. At these lower y-locations the integrand can be expected to decrease monotonically to zero with decreasing y. The remainder of the integrand was therefore approximated with a Gaussian function. This function was fit to the measured data on the low-speed side of the peak in the integrand and the nearest point on the high speed side; see Figure 2.21.

The measured values of the integrand were integrated using trapezoidal integration, and the Gaussian fit was integrated *only* over the remaining region on the low-speed side. The two values obtained were then added together. The "robustness" of this method was assessed by using it to determine θ for two velocity profiles obtained by Hellum (2006) at different streamwise locations. All three velocity profiles were then plotted using their resulting similarity scaling, as in Figure 1.1. The present data were also plotted with θ altered by $\pm 5\%$; see Figure 2.22. This variation of $\pm 5\%$ in θ can be seen to cause a significant change compared to the differences between the present data and those of Hellum. This provides confidence that the Gaussian curve fit described above behaves similarly between the multiple data sets.

Within the streamwise extent of the measurement volume for the VSL position $320.4 \le x/\theta_o \le 382.7$, it was necessary to $y_{1/2}$ and θ were estimated using their values , θ was determined assuming $\frac{d\theta}{dx} = 0.035$. Note that $\frac{d\theta}{dx} = \frac{V_e}{U_o}$ for a zero pressure-gradient single-stream shear layer, and the condition $\frac{V_e}{U_o} = 0.035$ was directly measured as described in Section 2.1.2. The value for $y_{1/2}$ was assumed to be directly proportional to x, although this is only approximately correct.

The vorticity, or maximum-slope, thickness, is another common measure of shear layer thickness and is defined as:

$$\delta_\omega \equiv \frac{\Delta U}{\left.\frac{\delta \bar{U}}{\delta y}\right|_{max}}. \qquad \textbf{2.11}$$

Here, ΔU is the velocity difference across the shear layer and $\left.\frac{\delta\bar{U}}{\delta y}\right|_{max}$ is the maximum value of the transverse gradient in the mean streamwise velocity. For a single stream shear layer , $\Delta U = U_o$. Since the mean velocity profile is self-preserving, δ_ω can be expressed as a constant multiple of θ, and for this flow it was determined that $\delta_\omega = 4.40\theta$.

2.4 VSL Location Measurements and Processing

The instantaneous location of the VSL was measured by using two cameras to obtain pairs of simultaneous images: i) plan view and ii) elevation view, of the smoke streakline produced by a lit stick of incense. The "vertical" (plan view) camera was oriented to look along the z-axis, while the "horizontal" (elevation view) camera was oriented to look upstream along the x-axis. The incense stick was located well within the non-vortical (non-turbulent) region of the entrainment flow, providing a "solid," continuous and easily-visible smoke trace. The streakline was illuminated using several flood lights placed on the floor of the SSSL facility. A descriptive representation of the setup is shown in Figure 2.23.

Where the streakline fluid interacted with vortical fluid from the shear layer, i.e., at the VSL, the streakline would become visibly more diffuse or disappear altogether due to turbulent diffusion by the vortical fluid. The location at which this would occur was often quite distinct and spatially localized, although some ambiguities were encountered as detailed in Section 2.4.5. A Matlab routine was written that allowed a user to view a pair of simultaneous images, one from each camera. In each image, the apparent location of the VSL was selected by the user and returned as a pair of 2-D “image coordinates.” Spatial calibration of the two cameras’ images allowed the two pairs of image coordinates to be mapped to 3-D “laboratory coordinates.” 1800 image pairs were acquired at a rate of 60 per second, providing 30 seconds worth of data. This image rate corresponds to a period of 16.7 ms $= 0.833\frac{\theta}{U_o}$ between images, where θ is the momentum thickness of the shear layer at the streamwise center of the measurement region $(x/\theta_o = 351.6)$. In other words, the primary fluid would travel, on average, 0.833 local momentum thickness between successive image pairs.

2.4.1 Equipment

Sony model XC-75 CCD cameras were used in both the vertical and horizontal camera positions. The XC-75 provides an analog output signal formatted per the EIA television standard, which specifies 29.97 full frames per second. Each full frame is comprised of two interlaced fields that are sent one-after-the-other. As the second field’s exposure begins and ends 1/60th of a second after the first field’s exposure does, a “full” image frame does not actually represent an instantaneous snapshot of the region being imaged, leading to unacceptable motion artifacts in regions of rapid streakline movement. For this reason, the individual fields and not full frames were captured and digitized into images. Thus, the vertical resolution was decreased by a factor of two as compared with a full (about 480 TV lines) EIA frame.

Since the images to be acquired were of moving objects, it was desirable to operate the cameras with as short an exposure as practical. This can be accomplished through the use of an electronic shutter, but this also comes at a cost to light sensitivity. Another way to shorten the exposure time is to set the charge accumulation mode of the camera to "field" mode, as opposed to "frame" mode. In field mode the CCD array only accumulates charge over the duration of one field period (1/60th of a second), as opposed to one frame period (1/30th of a second). The advantage of this over an electronic shutter is that the camera then compensates for the decrease in sensitivity by using row-pair summation (also called pseudo-interlacing, Holst 1996). For a full, interlaced frame, row-pair summation reduces the vertical resolution to about 350 TV lines. However, since only individual fields were digitized in this study, there was no additional loss of vertical resolution.

The vertical camera was outfitted with a Toyo 12.5 mm - 75 mm TV zoom lens, while the horizontal camera was outfitted with a Navitar Zoom 7000 18 mm - 108 mm Macro Zoom lens. The close-up (macro) lens of the Navitar was removed so that it functioned similarly to the Toyo TV lens. The cameras' apertures were fully open, with the Toyo set at f/1.8 and the Navitar set at f/2.0.

Two laptop computers, both running Windows XP, were each outfitted with a VCE-Pro image capture card manufactured by Imperx. Each computer/capture card setup was used to acquire, digitize and store the video output from one camera as a series of 8-bit, monochrome bitmap images. The images were digitized to 640 x 480 pixels, which is typical for digitization of EIA format frames. Image acquisition was begun by triggering the two cards with a single 0-5V pulse from a function generator. The two cameras were synchronized as described in Section 2.4.1.1, ensuring that corresponding images stored on the two computers had been exposed simultaneously by their respective cameras.

The vertical camera was located on top of the SSSL facility (out of the flow), and imaged through a glass window installed in the ceiling of the facility; see Figure 2.23. The horizontal camera was positioned at the test section exit, at $x/\theta_o \approx 830$.

The incense stick was mounted to a taut length of steel wire (diameter = 1.59 mm) that was oriented parallel to the z-direction at the location: $x/\theta_o = 335.1$, $y/\theta_o = -133.5$. This location corresponds to $\eta = -9.42$. The steel wire was anchored to the steel structure of the SSSL facility at both of its ends, and placed under slight tension to ensure that it did not vibrate. The incense sticks were selected based on their small diameter (approximately 2 mm) in order to prevent shedding, which would disrupt the streakline and "contaminate" the non-vortical entrainment fluid with vorticity. The Reynolds number of the flow around the incense stick was approximately 38, based on the mean entrainment fluid velocity of 0.28 m/s and the incense stick diameter. This is just below the critical value of 40-44 at which vortex shedding begins. As the entrainment fluid velocity in the vicinity of the incense stick was highly unsteady, the Reynolds number was certainly higher than 40 at times, however shedding was still not observed in the resulting streakline. This is possibly due to the increased kinematic viscosity at higher temperatures, which would be expected near the end of the lit incense stick.

The streakline was illuminated with three floodlights, positioned on the floor as shown in Figure 2.23.

2.4.1.1 Camera Synchronization

The cameras were synchronized to one another by supplying the video output of the horizontal camera to the Video/Sync input of the vertical camera. That the cameras were synchronized was then verified by acquiring images of a digital clock running on a third laptop computer screen and noting the agreement between the hundredths second place in each image; see Figure 2.24. Distinct numerals are not apparent for two reasons 1) the screen had a refresh rate of 60 Hz, and 2) there was no synchronization between the screen refresh rate and the cameras. Nonetheless, the hundredths place appears visibly identical for each image pair despite these effects, and demonstrates that the image pairs acquired by the cameras are simultaneous to within at worst 10 ms (a field period is 16.7 ms). 10 ms is likely a grossly conservative value, as the XC-75 specifications indicate that jitter is less than ± 50 ns for these cameras.

Some type of synchronization was also needed so that individual image exposures could be associated with corresponding portions of the concurrent hot-wire time-series. This proved difficult, since the capture cards and software for the image acquisition were only capable of recognizing interlaced, continuous (analog) video input. Hence, the restart/reset image mode of the video cameras, which can be used to start an image exposure upon a random external trigger signal, could not be used.

Instead, the horizontal camera was externally driven using a third camera (NEC TI-24A). The vertical drive signal, which has a definite relation to the start of an image exposure, was buffered with a unity-gain amplifier, then digitally sampled along with the hot-wire data. Since the vertical drive signal is a negative-going pulse, from 5V to ~1V, the signal is 5V over most of the image exposure and could be used (with the buffer amplifier) to illuminate two LEDs. An LED was placed in view of each camera, at a location where it would neither be obscured by nor interfere with the streakline; see Figure 2.23. The signal to the LEDs could be switched on and off manually, and this was also digitally sampled along with the hot-wire data and the uninterrupted vertical drive signal. The time series was sampled at a frequency of 15kHz in order to make certain that several samples would capture the low portion of the drive signal, which was 0.6 ms in duration.

Data acquisition and synchronization to the images were then carried out as follows: 1) The time series acquisition was begun with the signal to the LED switched off. 2) The image series acquisition was begun, and the signal to the LED was switched on and off, manually, several times throughout the acquisition. 3) In the image series, images in which the LED appeared illuminated were identified. 4) In the time series, vertical drive pulses for which the signal to the LED was switched on were identified. 5) Care was taken to ensure that the signal to the LED was switched on and off for different lengths of time, so that the LED was not on or off for the same number of images each time. In this way, a correspondence could be confidently made between groups of images where the LED was illuminated and groups of vertical drive pulses where the signal to the LED was switched on.

2.4.2 Image Calibration

A 2-D calibration grid of crosses was drawn, laminated and mounted to rigid foam board as shown in Figure 2.25. The crosses were spaced 7.62 cm apart in both directions on the grid. After the cameras were set in their final positions, the grid was imaged by each camera at several distances, in increments of 7.62 cm to match the cross spacing. Seven calibration images were acquired in plan view by the vertical camera, covering the range: $-38.1\text{ cm} \le z \le 7.62\text{ cm}$. Similarly, 10 calibration images were acquired in elevation view by the horizontal camera, covering the range: $352.4\text{ cm} \le x \le 421.0\text{ cm}$.

A Matlab routine was written that allowed a user to manually click the center of each cross in a given calibration image. The location of a cross center was returned by the program as a pair of 2-D image coordinates. These image coordinates were based on the pixel row and column indices in the image, although they were not restricted to integer values. The lab coordinates of the crosses were known by their spacing on the grid, and the fact that the position of the grid was known. For each image, the image coordinates of the crosses were stored with their associated lab coordinates for use in processing.

The plane corresponding to $z = 0$ was defined as follows: With the primary flow off, the streakline was observed to attain a stable height about 5 cm higher than the incense stick, due to its initially elevated temperature upon leaving the stick. This height was defined to be $z = 0$. The extent of the z-range was then determined by turning the primary flow on and observing the extent of the streakline's excursions from this plane in the region of the VSL. It was decided that the range: $-38.1 \text{ cm} \le z \le 7.62 \text{ cm}$ would adequately contain most of these excursions.

The excursions occured, both directly and indirectly, as a result of entrainment fluid "buffeting" due to the passage of large-scale motions in the vortical region. Directly, the buffeting action resulted in unsteady displacement of the streakline in all three coordinate directions, with an (estimated) range of $\pm 7.62 \text{ cm}$ in the z-direction. Indirectly, the buffeting motion resulted in the formation of thermal "plumes" at intervals along the length of the streakline, as shown in the photograph of Figure 2.26. This was because the quasi-periodic, y-direction motion of the entrainment fluid caused some of the streakline fluid to spend more time in the vicinity of the heated tip of the incense stick. This fluid was accordingly heated more and would often rise into a plume as it was convected towards the shear layer, attaining a maximum (estimated) height of 38.1 cm above the plane $z = 0$.

2.4.3 Image Processing

Consider a pair of streakline images, one from each camera, in which the image coordinates of the VSL have been identified. For the vertical camera image there are 7 calibration planes, each with a different z-coordinate, within which x and y coordinates have been mapped to the image coordinates. For each calibration plane, identified by $z = z_k$, linear interpolation between the calibration point pairs was used to map the image coordinates of interest to lab coordinates (x_k, y_k). Thus, the (x, y) location of the VSL was established as a function of its z-location, as shown in Figure 2.27. Using a similar procedure for the horizontal camera image, the (y, z) location of the VSL was established as function of its x-location; see Figure 2.28.

The lenses were of sufficiently low-distortion that x and y were very nearly linear with z for the vertical camera, while y and z were very nearly linear with x for the horizontal camera. Thus, one could consider $x(z)$ and $y(z)$ to describe a line through space associated with the VSL position on the vertical camera image. Similarly, $y(x)$ and $z(x)$ described another line in 3-D space associated with the VSL position on the horizontal camera image. This is shown schematically in Figure 2.29. The intersection of these two lines would identify the actual location of the VSL: $(x, y, z)_{\mathrm{VSL}}$. The values: $\theta(x_{\mathrm{VSL}})$ and $y_{1/2}(x_{\mathrm{VSL}})$ were estimated for each observation as described in Section 2.3.5.

These were then used along with the measured value of y_{VSL} to determine the dimensionless transverse location of the VSL: η_{VSL}.

Errors could be introduced by several effects. Since the VSL was selected visually in both images, some skill was required on the part of the operator to ensure consistency of the selected image locations with one another; see Section 2.4.5 for a description of the visual selection process. Additionally, the linear interpolation used to map image coordinates to lab coordinates within each calibration plane and in-between different calibration planes is only an approximation. Due to these effects, the lines would not actually intersect. However, their closest points-of-passage to one another were easily determined from a two-parameter minimization problem (see Appendix A). The average of these two locations was taken as the locations of the VSL, while the distance between the two locations provided an estimate of uncertainty for the measurement.

Measurement uncertainty was also estimated by acquiring images with a stationary LED (diameter ≈ 4 mm) positioned in the measurement volume. The location of the LED was measured using the foregoing procedure at 6 different (known) locations throughout the measurement region. The two lines in space that were used to estimate the measured location passed within 1.9 mm of one another, on average, with a maximum disagreement of 2.7 mm. The distance between the measured locations and their known values was 7.4 mm, on average, with a max of 9.8 mm. For reference, the width of the shear layer is approximately $6\theta = 91.2$ cm at the center of the vertical camera's image.

2.4.4 Scaling of VSL Statistical Data

On occasion, the terminus of the streakline would occur outside one or both cameras' fields of view. Images in which the streakline terminus was out-of-sight in the x or z-direction were not considered part of the sample population. There were 253 such images in the record of 1800. If the streakline terminus was out-of-sight in the y-direction, shown in Figure 2.30, the image was still considered as part of the sample population for the purpose of scaling the statistical data. There were 109 such images in the record. Therefore, the sample population was considered to be comprised of $1800 - 253 = 1547$ images. Of these, the VSL was considered to exist in $1547 - 109 = 1438$ of them, or 93.0%. Therefore it is estimated that the highest 7% of η_{VSL} values were not observed. Note that the VSL was *considered* to exist in 1438 images; the number in which it was actually identified was considerably less than this: 444. In some images it was possible to identify the VSL at more than one location, so that the total number of VSL observations was equal to 492.

2.4.5 Visual Determination of VSL Location

It was initially believed that the streakline terminus, and hence the location of the VSL, would be apparent in each image. In some images, this terminus is indeed quite sharp; see Figure 2.31. In many others, the terminus was obscured by two main factors. First, a finite time was required for recently-sheared streakline fluid to be dispersed by vortical fluid, so that sheared fluid was not necessarily rendered "immediately" invisible in the images. Secondly, the streakline was sometimes substantially deformed within the irrotational fluid due to the increasingly small-scale, potential fluctations associated with the approaching VSL. These fluctuations are a result of the unsteady pressure field created by motions within the vortical fluid. Phillips (1955) obtained the result that the wavenumber content of these fluctuations falls off quickly with increasing distance from the VSL. For example, the “buffeting” of fluid in the vicinity of the incense stick, described in Section 2.4.2, is dominated by low wavenumber (large scale) motions within the vortical fluid. The irrotational fluctuations conversely exhibit increased high wavenumber (small scale) content closer to the VSL, so that the streakline could become significantly “kinked” and folded at smaller scales before actually being sheared. Since this effect was most pronounced closest to the VSL, the distinction between kinked versus sheared streakline fluid was difficult to make; see Figure 2.32. The VSL location was not identified in such images.

A slit-jet facility was constructed to provide more controlled conditions under which the behavior of the streakline could be observed. A plate of glass formed one of the span-wise boundaries so that the “training” images acquired could include a portion of the flow upstream of the jet outlet; see Figure 2.33. A streakline introduced well upstream could then be observed in the region of relatively high axial strain that exists from about one jet-width upstream to one jet-width downstream of the outlet. Another streakline was introduced from the side of the jet, just downstream of the outlet. This allowed the terminus of a sheared streakline to be observed in a region of strong, yet time-steady shear without additional complications due to unsteadiness or large scale motion. Images were taken at $U_o = 2$ m/s and 7 m/s for comparison with velocities in the shear layer.

From these images, it was realized that the location at which the streakline was sheared was obvious when the images were viewed as a video, but not when they were viewed as single images. Viewed as a video, the interaction of the streakline with sheared fluid could be clearly identified by a rapid “tearing” motion at the terminus of the streakline. The graphical user interface used for processing of the image pairs acquired in the shear layer facility was modified so that image pairs could be viewed in rapid succession. The VSL was then identified by looking for similar rapid, small-scale tearing motions at the end of the streakline, and these were taken to indicate shearing by the vortical fluid. In the record of images that is presented, 119 such small-scale tearing events were recorded for which the VSL could confidently be located. For each of these “confident” events, it was usually possible to also identify the VSL in several subsequent images, bringing the number of observations up to 492.

It can be noted in Figures 2.30, 2.31 and 2.32 that two incense streaklines are visible, especially in the vertical camera images. The flow around the tip of the incense stick resulted in distinct streaklines being released from each side. The upstream streakline was not easily visible towards the entrainment side of the horizontal camera images since it was occluded by the downstream streakline. It was more frequently visible towards the shear layer side since the two streaklines would then have had time to separate slightly in the z-direction. If VSL locations were identified along both streaklines, a proportionally greater number of observations might be made towards the shear layer; therefore only observations along the most downstream streakline were recorded.

2.4.6 Concurrent Hot-Wire Measurements

For the hot-wire measurements that were made concurrently with the VSL location data, five single-sensor probes were used. Two were designated as “reference sensors” and were used to indicate the passage of the large motions in the shear layer. Their sensors were located just upstream and downstream of the VSL location measurement region, at $x/\theta_o = 306.6$ and 382.7, and well-within the entrainment stream at $\eta = -4.6$. The remaining three probes comprised a "rake" that was located in the interior of the shear layer. Their sensors were placed at the same streamwise location as the downstream reference sensor, and their transverse positions were: $\eta = -1.5$, -2.18 and -2.86.

In order to keep the probe bodies from interfering with the horizontal camera's line of sight, x-array probes were used with only one operating sensor; see Figure 2.34. The sensor was oriented parallel to the z-axis so that the probe body would slope down and out of the horizontal camera's line of sight. This had the additional advantage of locating the majority of the probe body below the measurement domain to minimize interference with the flow. All sensors were positioned at $z = 0$, the nominal height of the steady streakline.

The reference sensors that were used to detect passing large motions were not calibrated, since only the qualitative features of their time-dependent voltages were utilized. The auto-correlation of each sensor's signal was formed as an indicator of the streamwise scale of the large motions, and the cross-correlation of the voltages from the two sensors was formed as an indication of their convection speed. The three sensors in the interior of the shear layer were calibrated to provide velocities.

2.4.7 Discrete Velocity Statistics of Plumes

Every new plume that appeared in the images was "assigned" a number and then tracked from image to image; see Figure 2.35. This was done until the plume was ingested by the shear layer, or until it was strained too much to confidently locate the same fluid between images. This provided material trajectories far within the entrainment fluid, and also allowed for the estimation of velocities. The velocities were formed by "centrally-differencing" the plume locations and then dividing by the twice the time between frames. For a given plume at time t_o, its velocity was estimated as

$$\vec{U}(t_o) = \frac{\vec{x}(t_1) - \vec{x}(t_{-1})}{(1/30)\ \mathrm{s}}, \qquad \mathbf{2.12}$$

where $\vec{x}$ is the position vector of the plume.

2.5 Measurements of Primary Fluid Maximal Extent

The maximal extent of the primary fluid was measured by seeding the primary fluid with fog particles from a Rosco theater fog generator. If the fog particles are sufficiently small (such that their slip velocities are "small"), they can be considered to be a "non-diffusive marker" for the fluid dynamic particles in which the droplets reside. Formally, for $D[\ ]/Dt$ as the Lagrangian transport term for a fluid dynamic particle with property [ ], $D[\ ]/Dt = k\nabla^2[\ ]$ can be used to describe the time variation of [ ] within the fluid dynamic particle where k is the diffusion coefficient. Since k is very small $(k \ll \nu)$ given the inability of the molecular constituents of air to force the motion of the oil fog droplet, it is acceptable to consider the "fog" to retain its marking of the fluid that passed $x = 0$ at $y > 0$ positions. The concentration of these particles is effectively a non-diffusive quantity, in contrast with vorticity. An argon-ion laser beam illuminated the fluid along a line oriented parallel to the y-direction at $x/\theta_o = 351.6$ and $z = 0$, the center of the VSL location measurement domain. The beam was imaged with the vertical camera. As fluid was swept through the beam, regions of high light intensity were apparent in the camera image along the beam axis, corresponding to the presence of seeded particles from $x < 0$, $y > 0$. An intensity threshold just above the background level was set so that pixels displaying an intensity greater than this were considered to be occupied by primary fluid. An example of such an image is shown below in Figure 2.36. For each image acquired, the maximal extent, towards the irrotational entrainment fluid, of pixels above the intensity threshold was recorded.

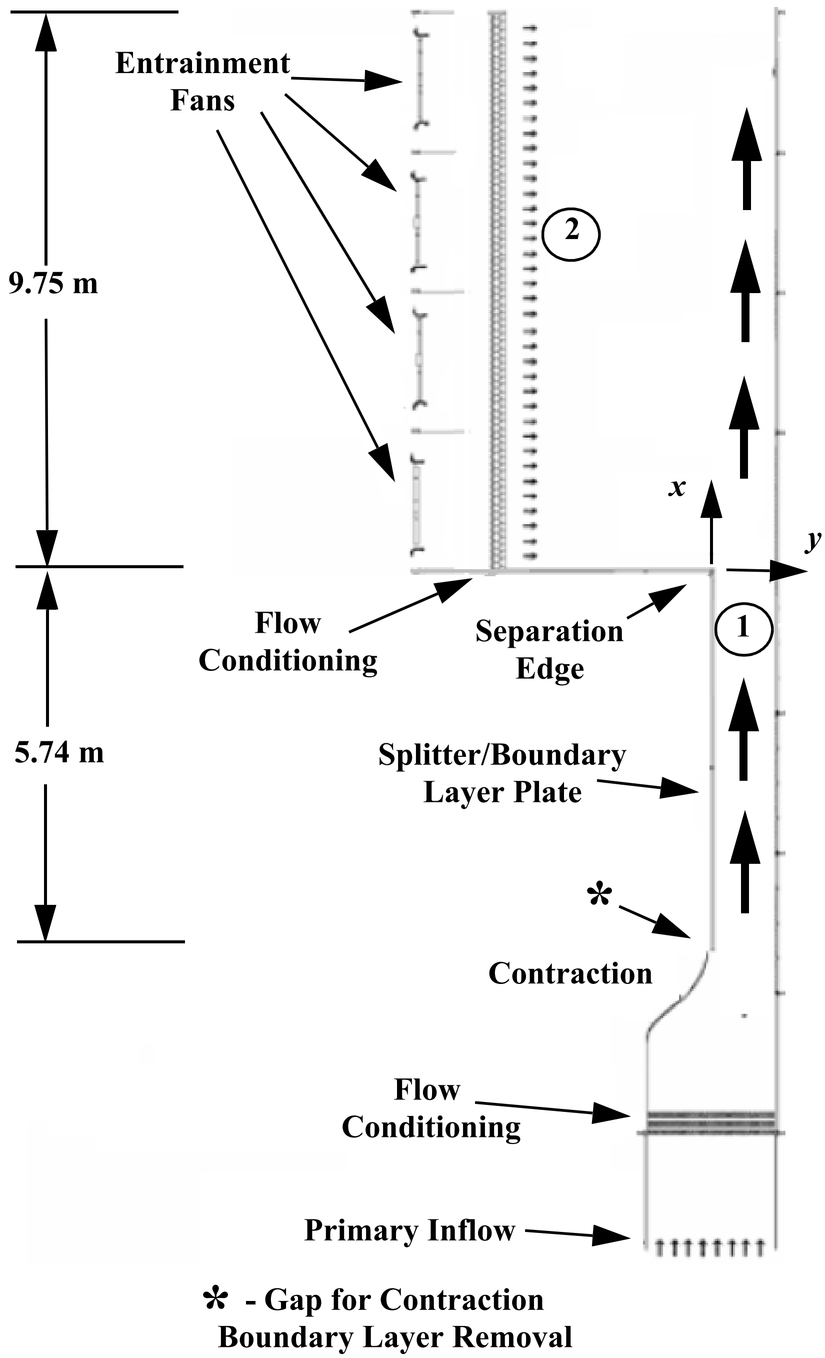

Figure 2.1 Schematic of the SSSL facility

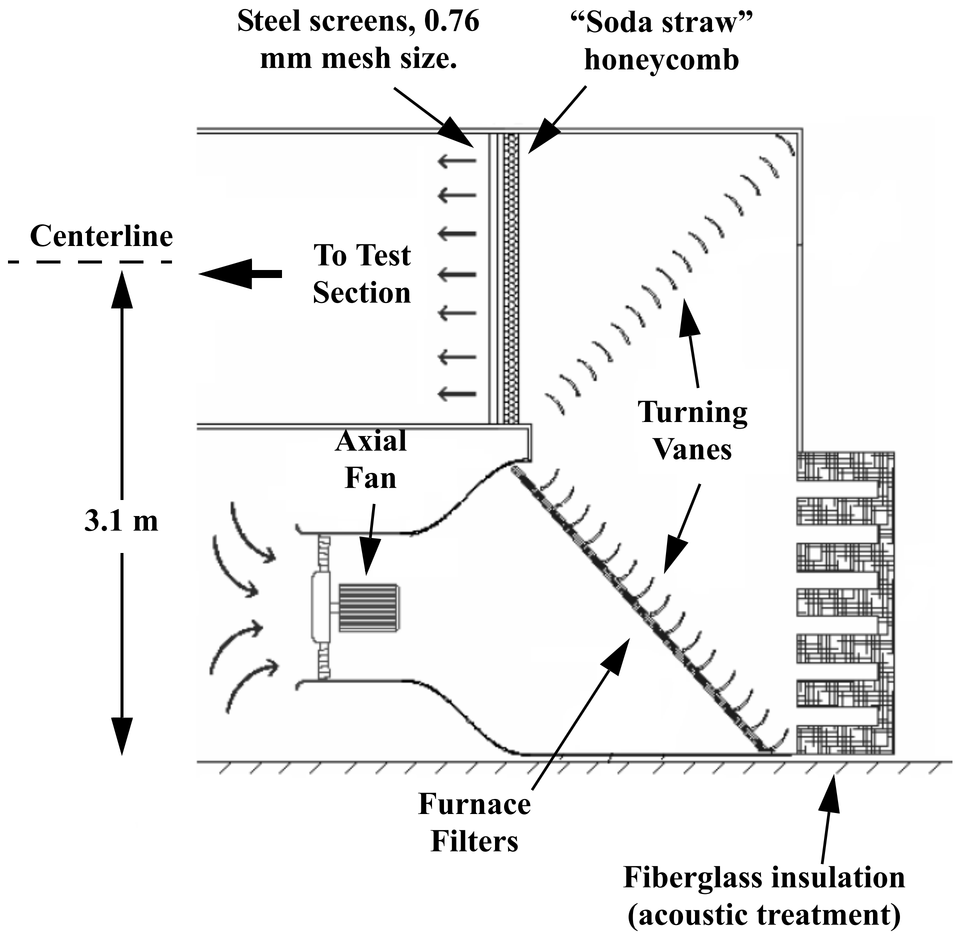

Figure 2.2 Cut-away view of primary-flow delivery system

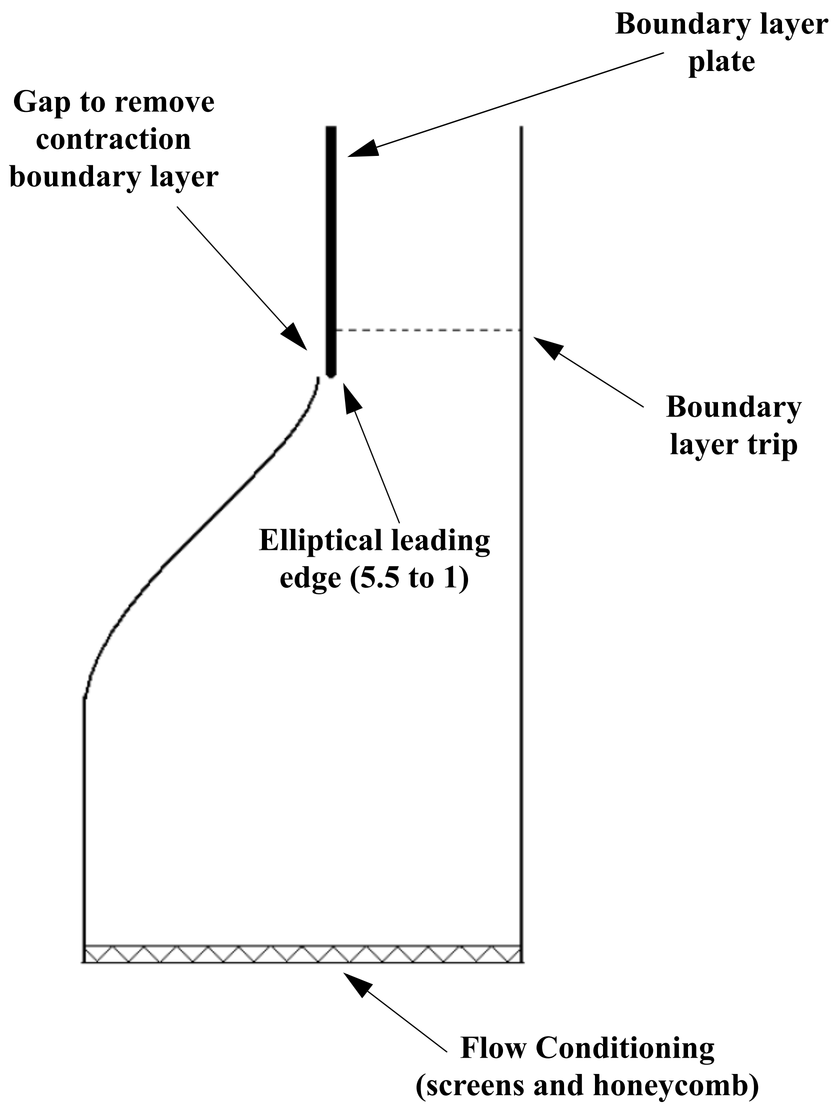

Figure 2.3 Schematic of contraction

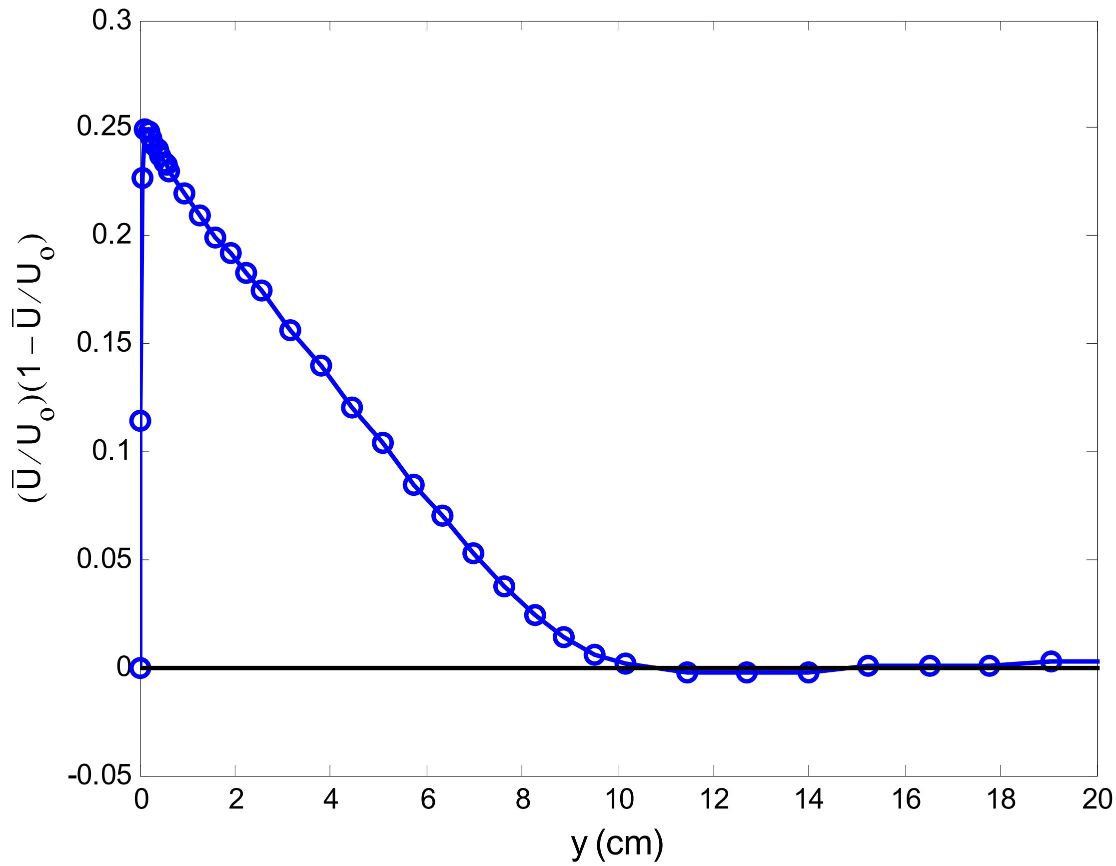

Figure 2.4 Momentum thickness integrand of the separating boundary layer. Note the approach to zero in the free stream and towards the wall, even though there are few data points near the wall.

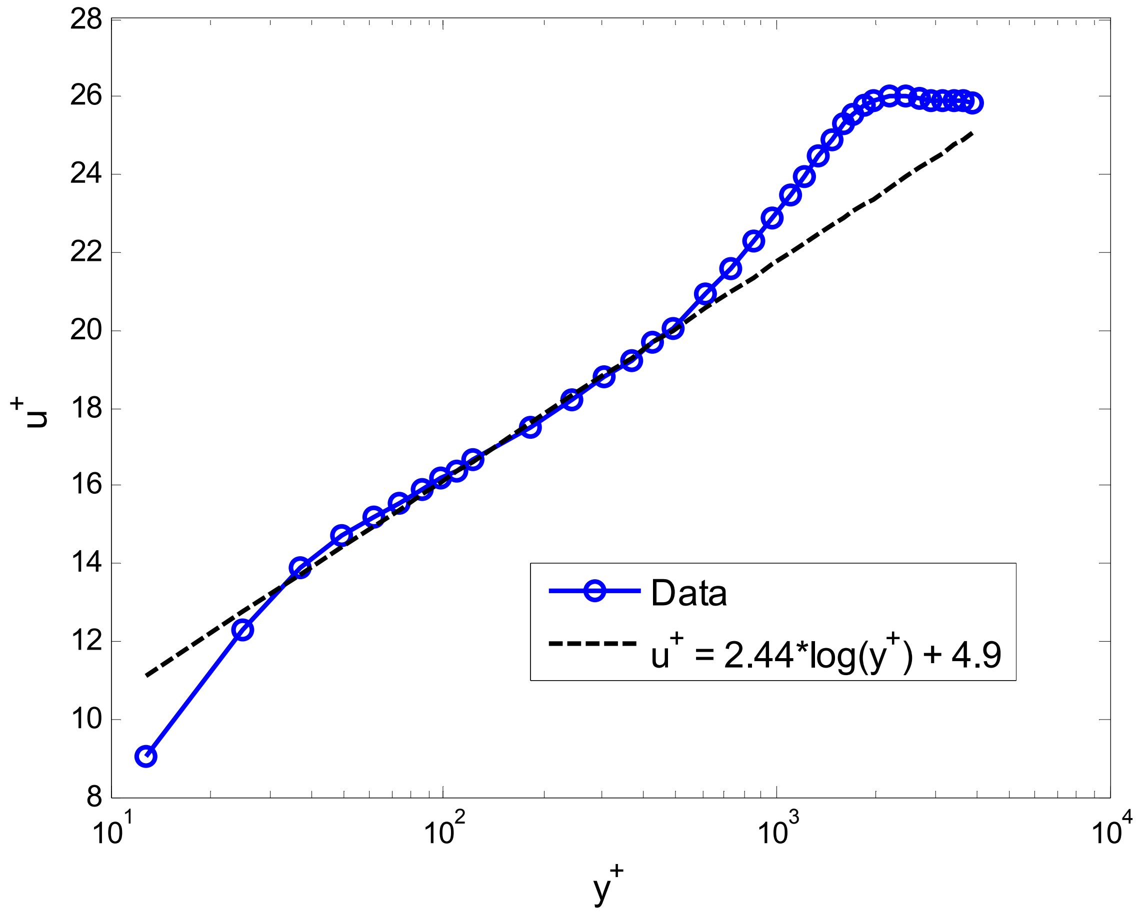

Figure 2.5 Mean velocity profile of separating boundary layer, in "wall coordinates."

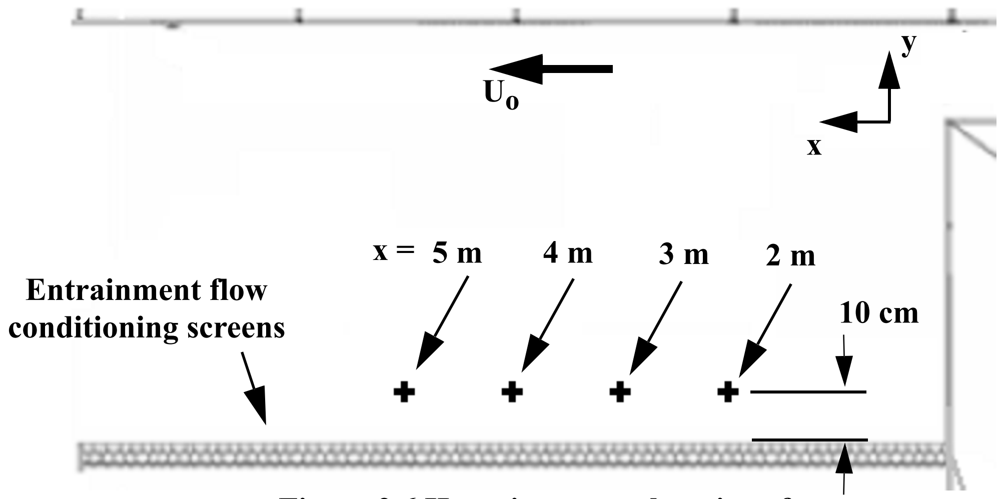

Figure 2.6 Hot-wire sensor locations for measurement of V_e to set entrainment fans.

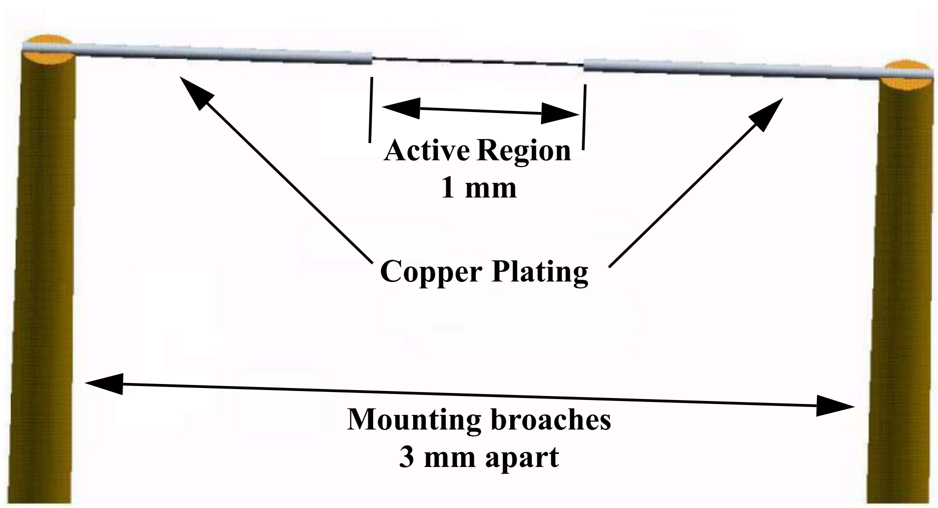

Figure 2.7 Schematic of a mounted, single hot-wire sensor.

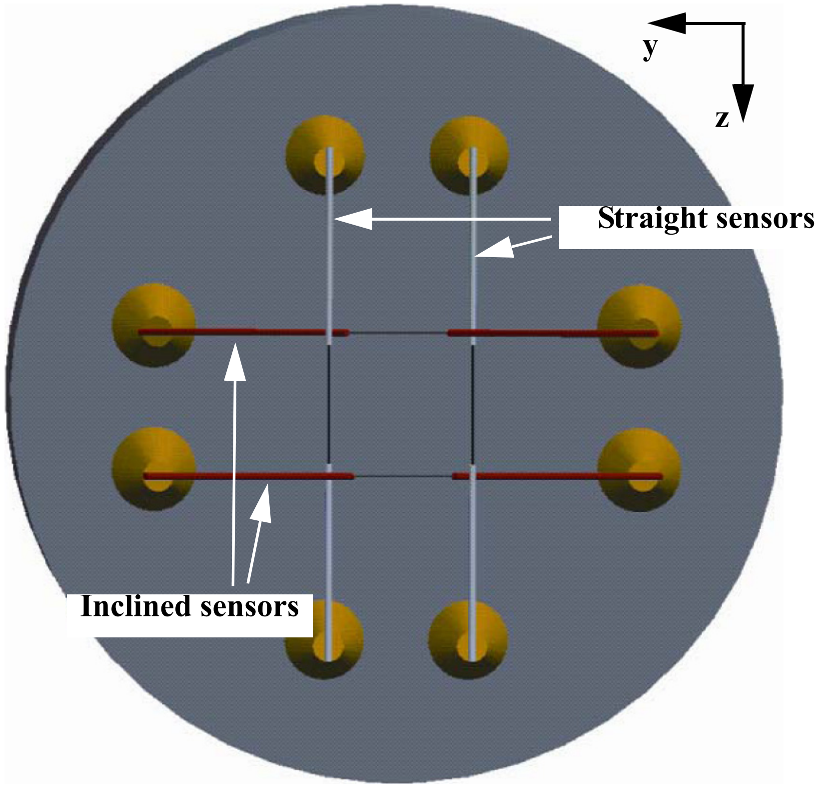

Figure 2.8 "Head-on" view of vorticity probe (looking downstream).

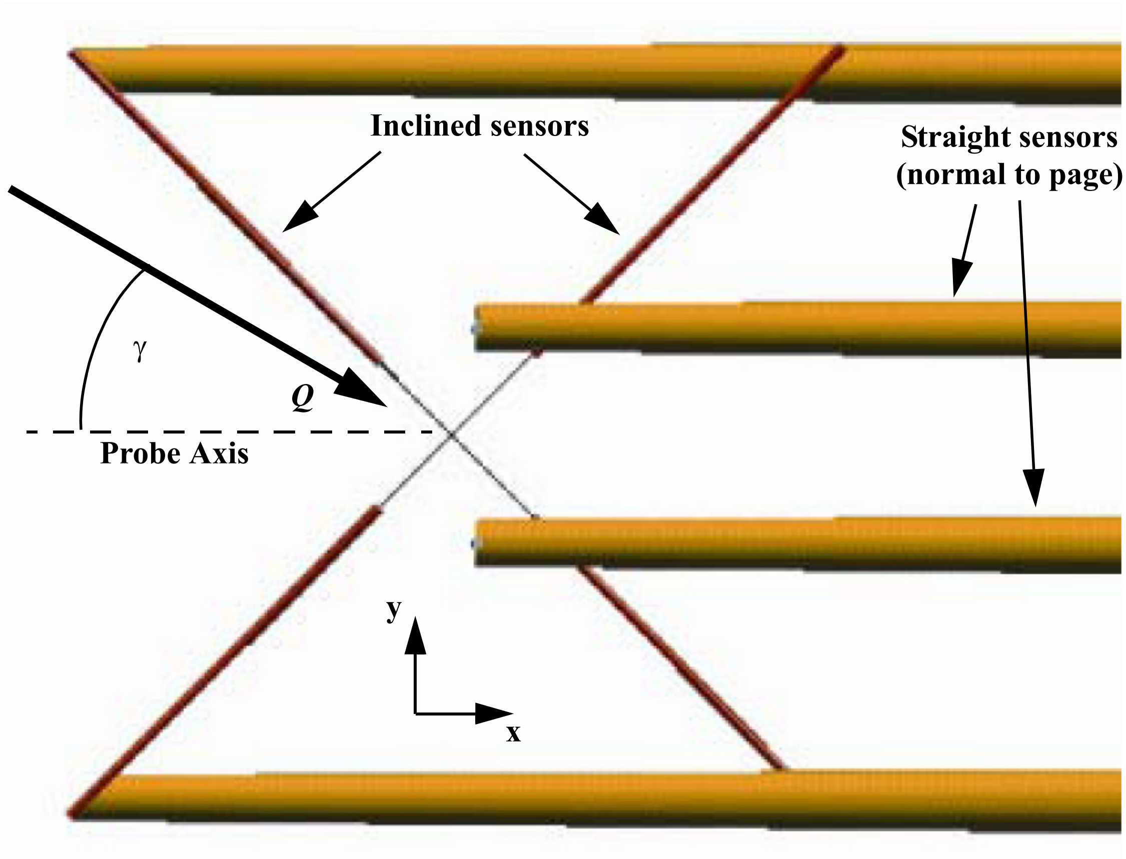

Figure 2.9 View of vorticity probe showing the inclined sensors of the x-array. Inclined sensors are approximately 1 mm apart in the *z*-direction (normal to the page). The velocity component and angle in the plane of the page are measured.

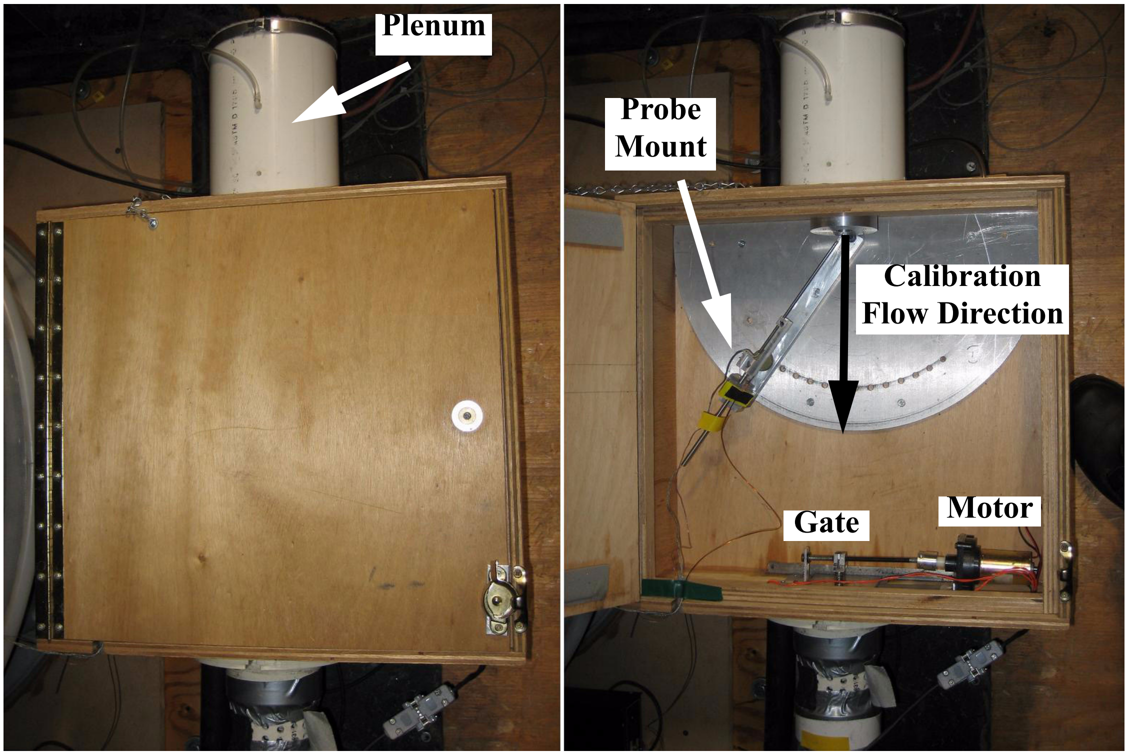

Figure 2.10 Hot-wire calibration facility, closed (left) and open. Note that in this image, the probe is angled with respect to the flow direction.

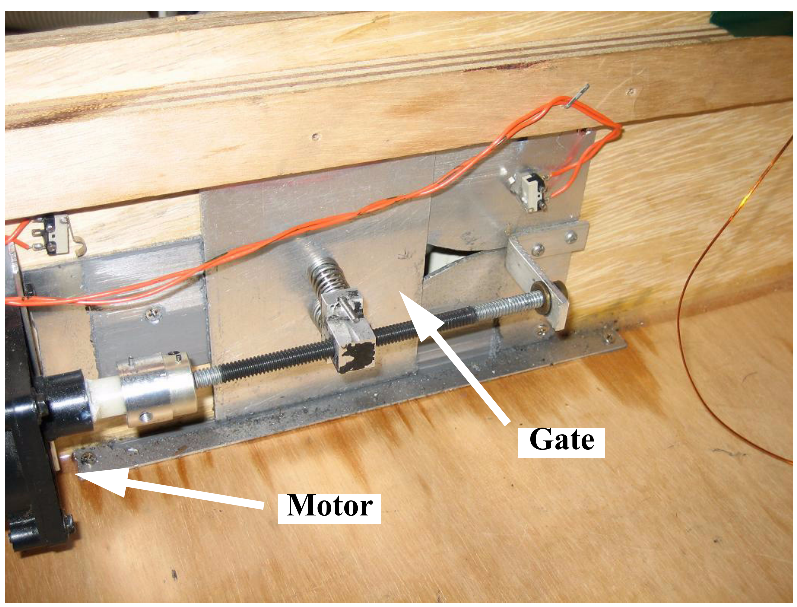

Figure 2.11 Close-up of motor and gate assembly to continuously vary calibration speed.

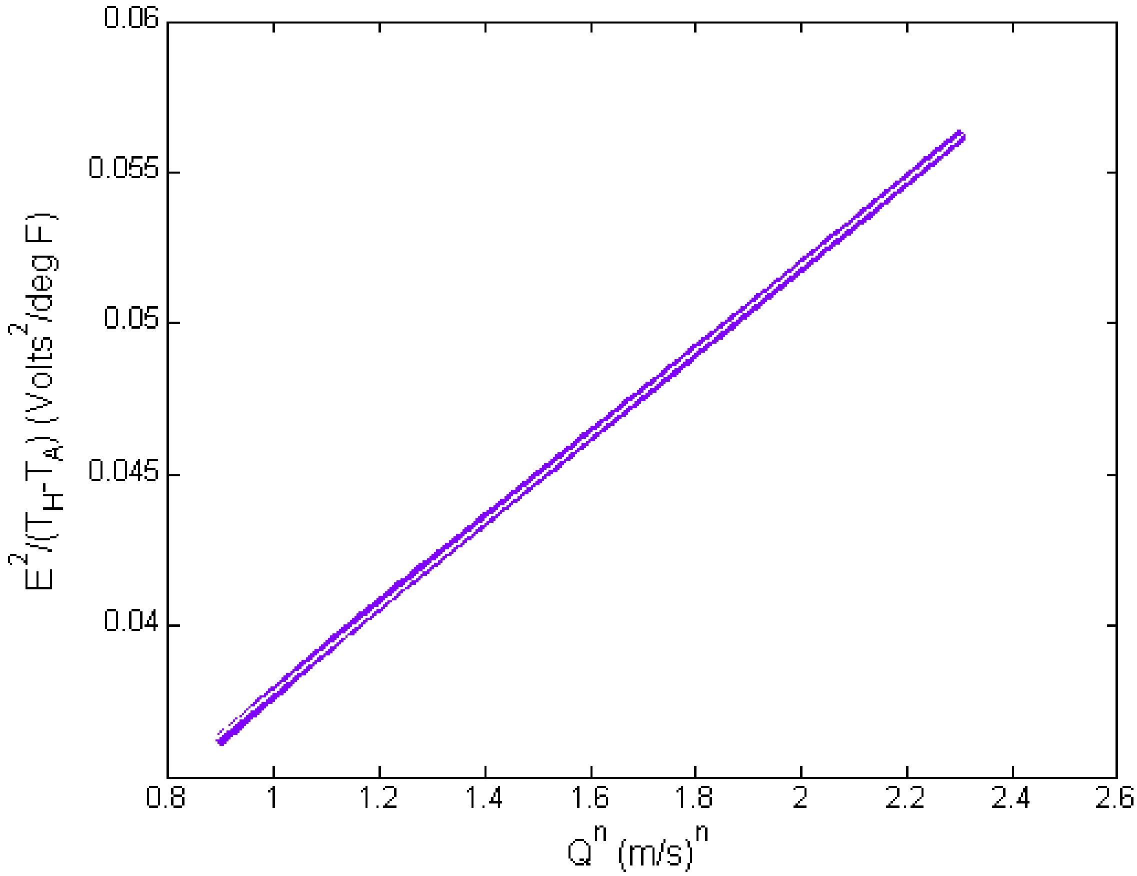

Figure 2.12 Typical inclined-wire calibration data and best fit linear function.

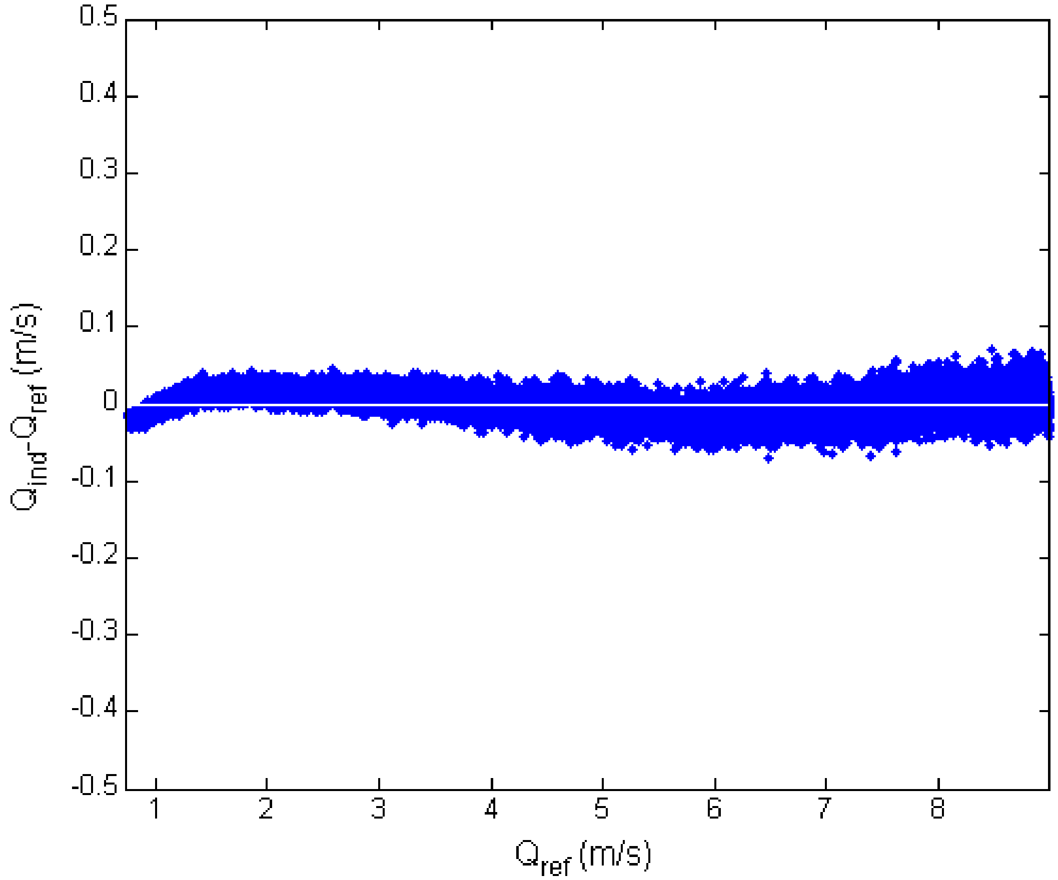

Figure 2.13 Difference between calibration reference velocities and values predicted by best fit linear function from Figure 2.12.

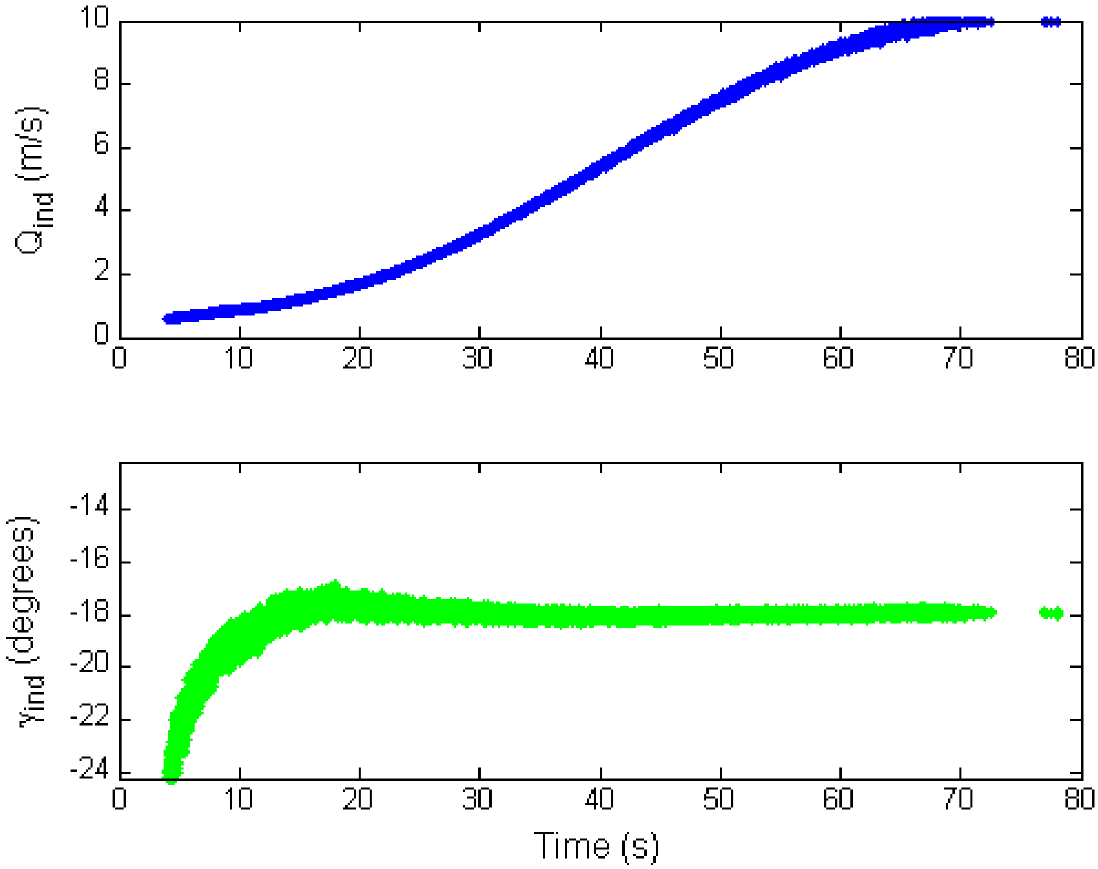

Figure 2.14 Time series of calibration data, processed using best fit linear function from Figure 2.12. Actual flow angle is -18°.

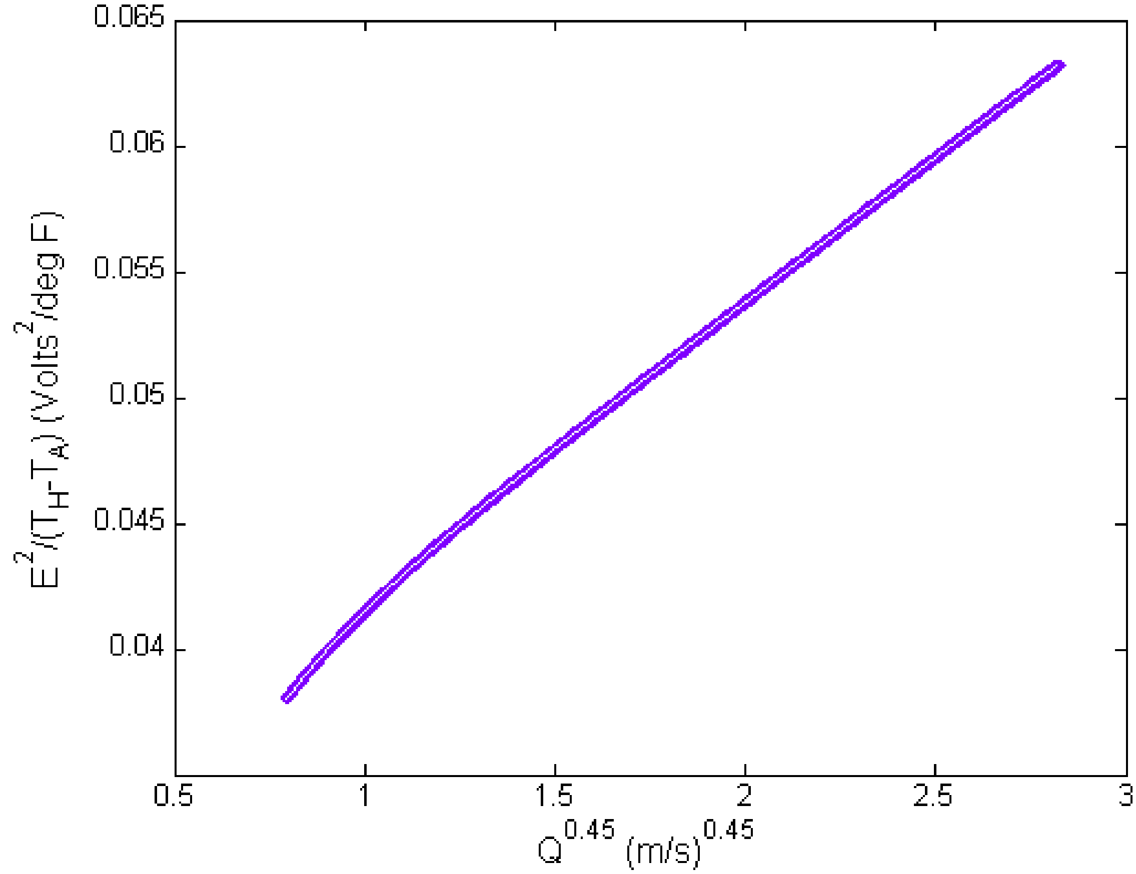

Figure 2.15 Inclined-wire calibration data from Figure 2.12 and best fit polynomial function.

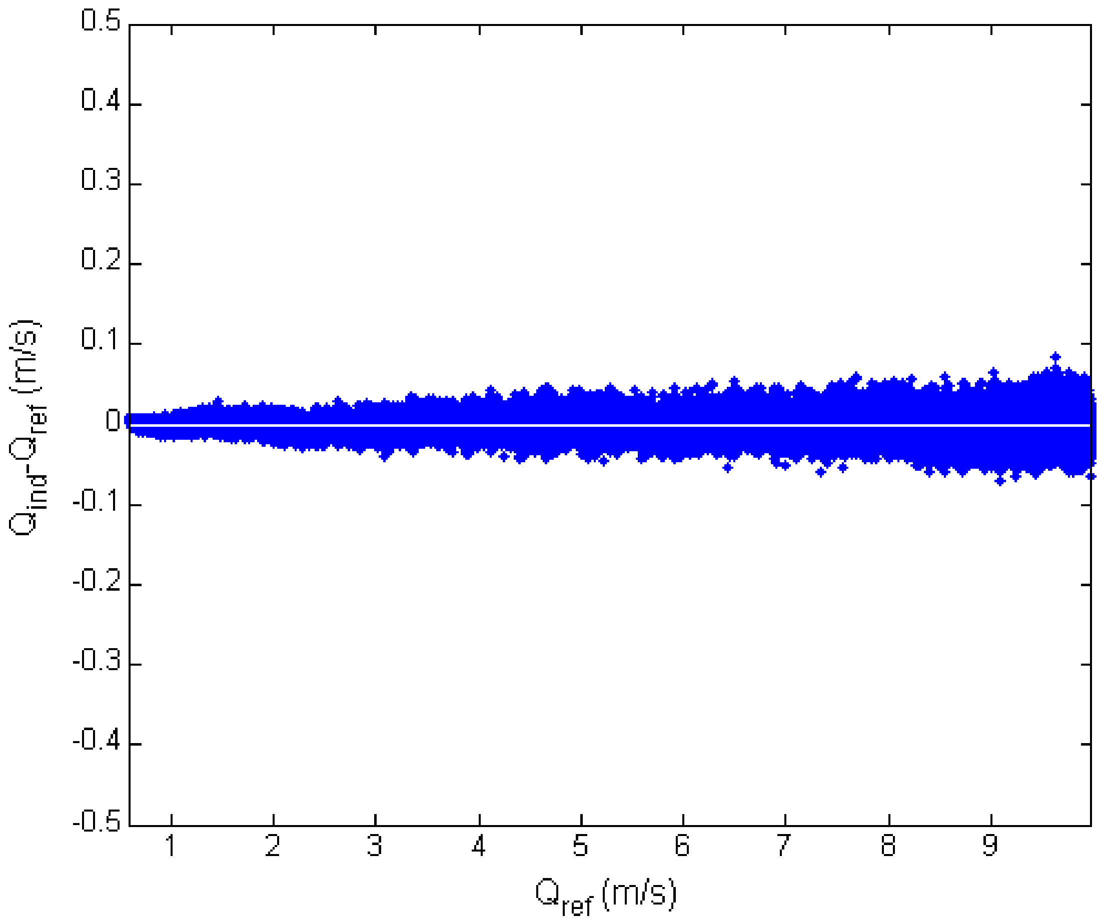

Figure 2.16 Difference between calibration reference velocities and values predicted by best fit polynomial function from Figure 2.15.

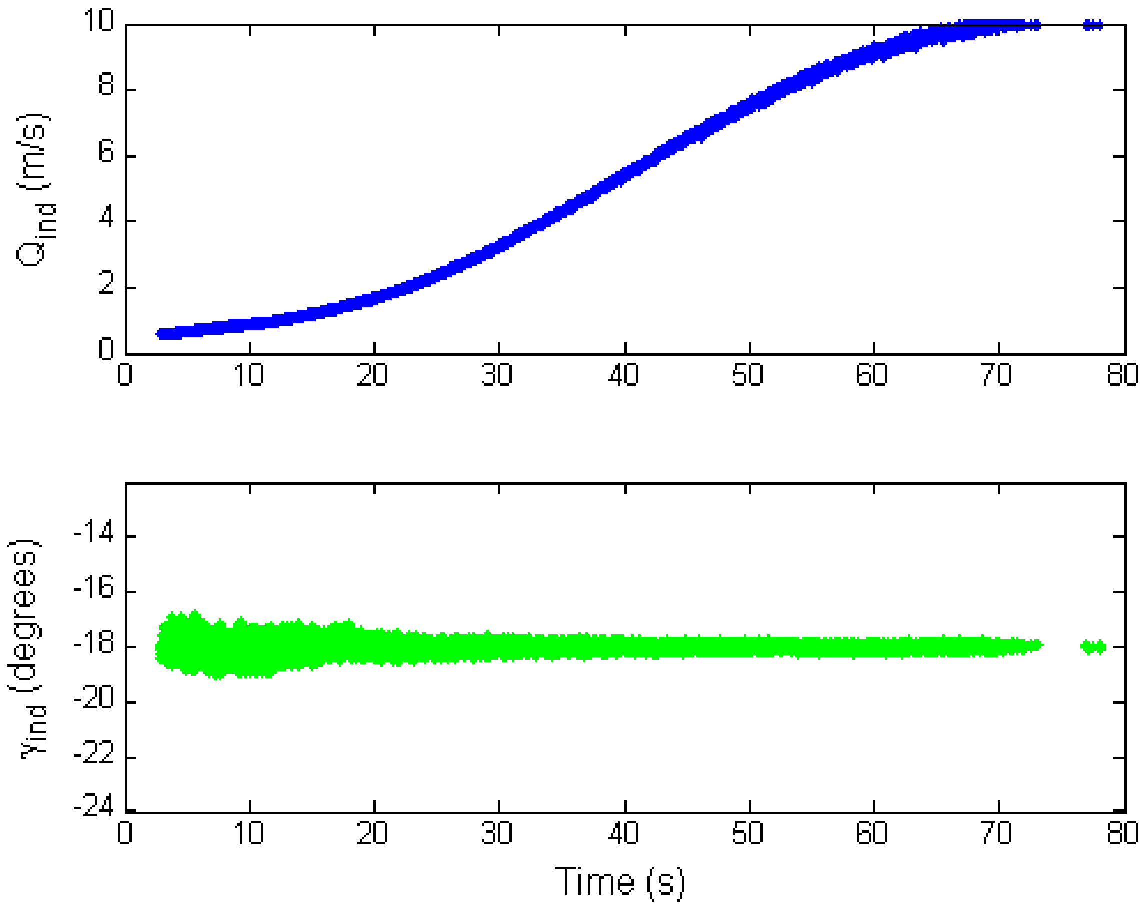

Figure 2.17 Time series of calibration data, processed using best fit polynomial function from Figure 2.15.

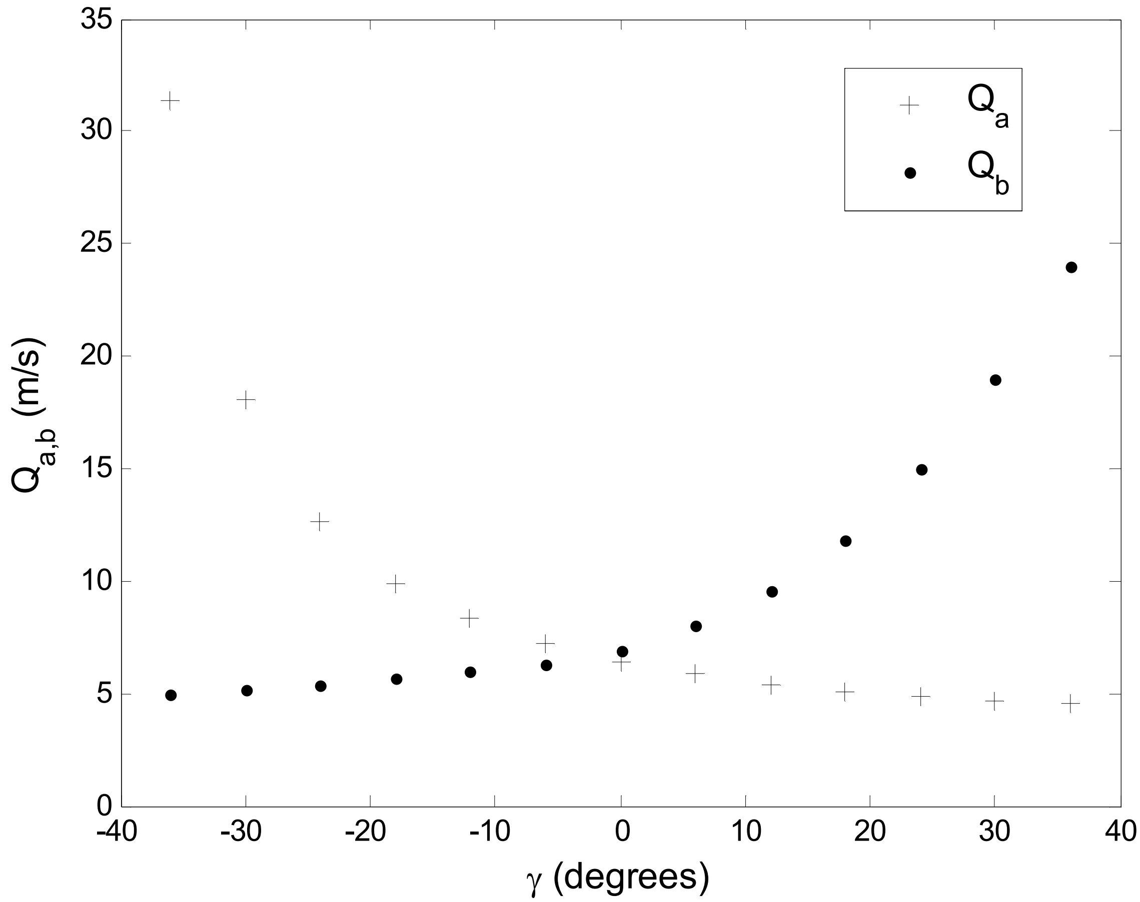

Figure 2.18 Velocities, $Q_{a,b}$, predicted by inclined sensors of x-array at different calibration angles (γ)

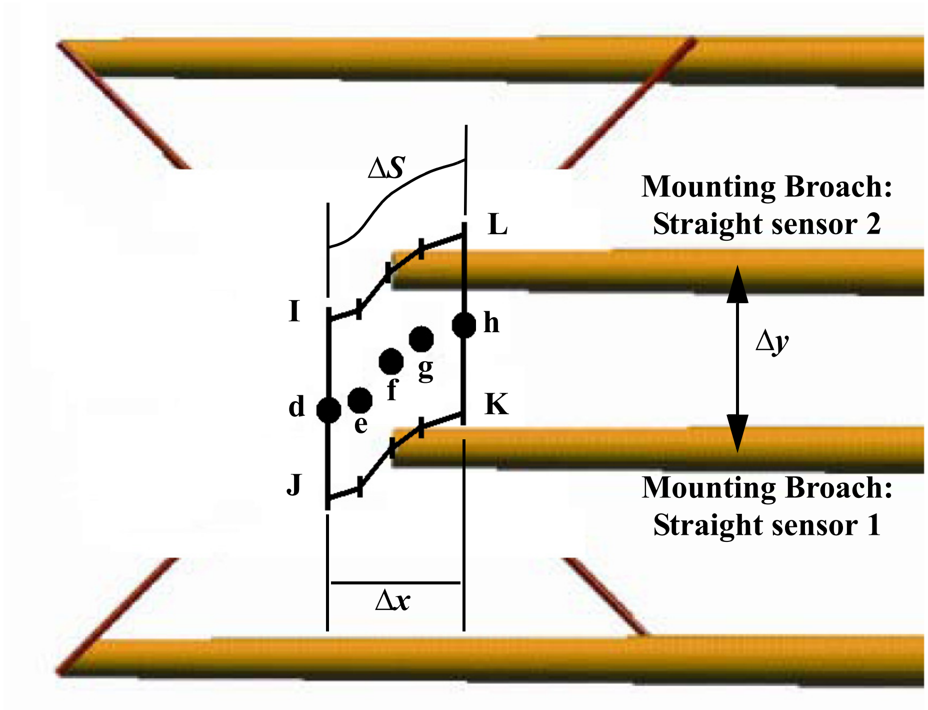

Figure 2.19 Micro-circulation domain for which $N = 2$ (5 time series points define the domain). Inclined sensors have been removed for clarity.

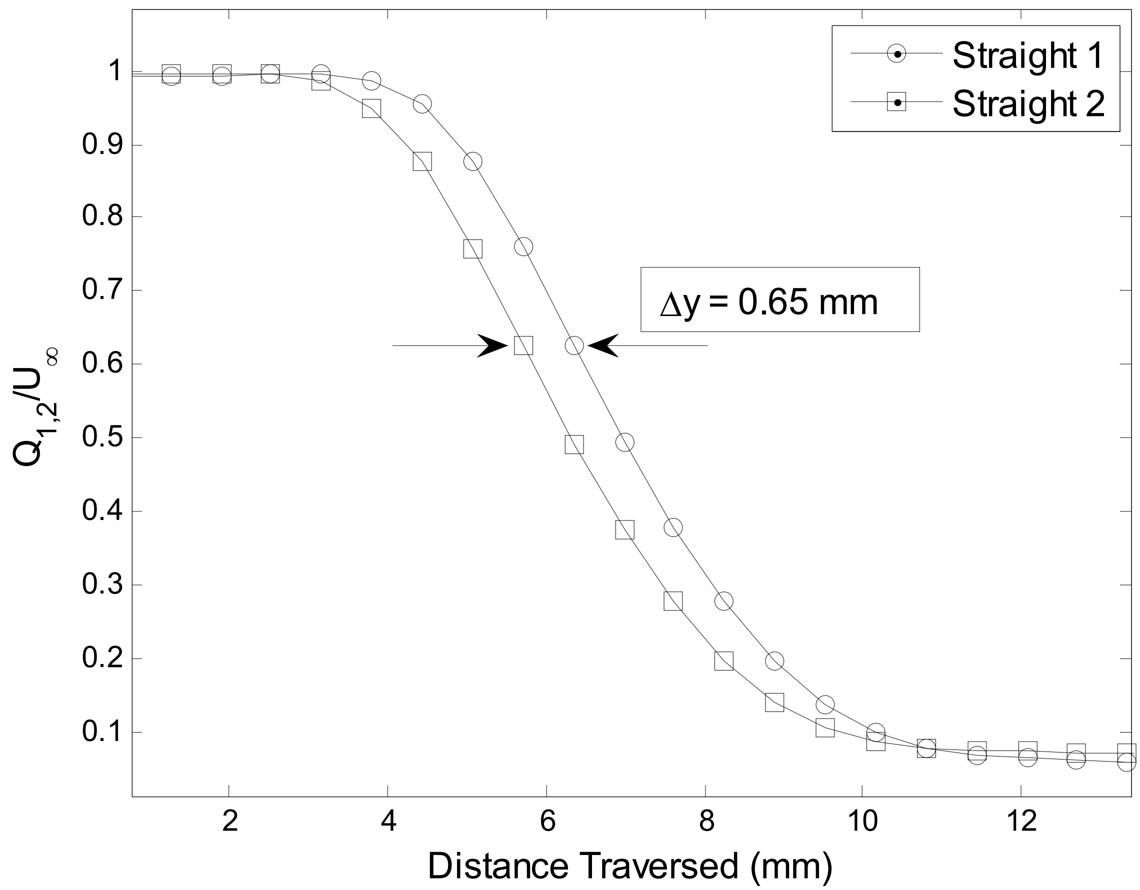

Figure 2.20 Example plot showing inference of Δy from mean velocity profiles measured in the "high mean shear" region of a slit-jet.

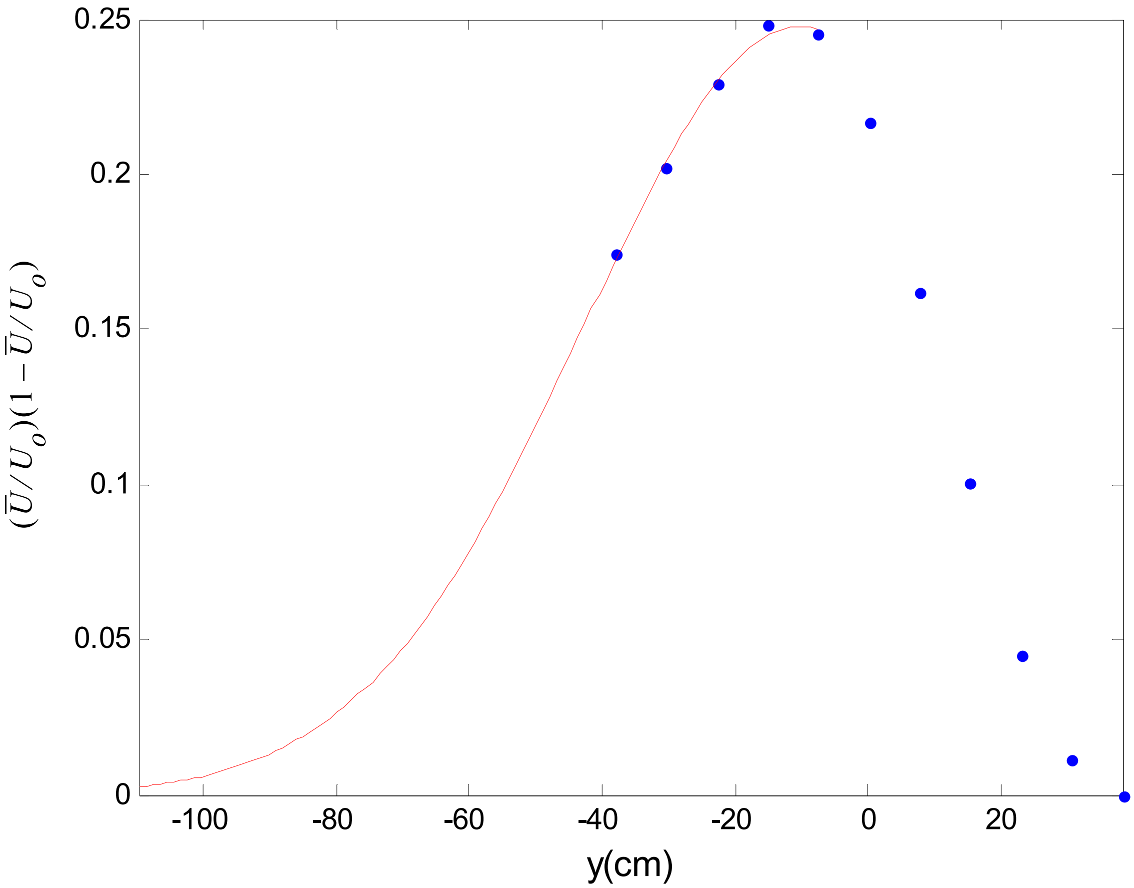

Figure 2.21 Gaussian fit to momentum-thickness integrand on low-speed side of shear layer.

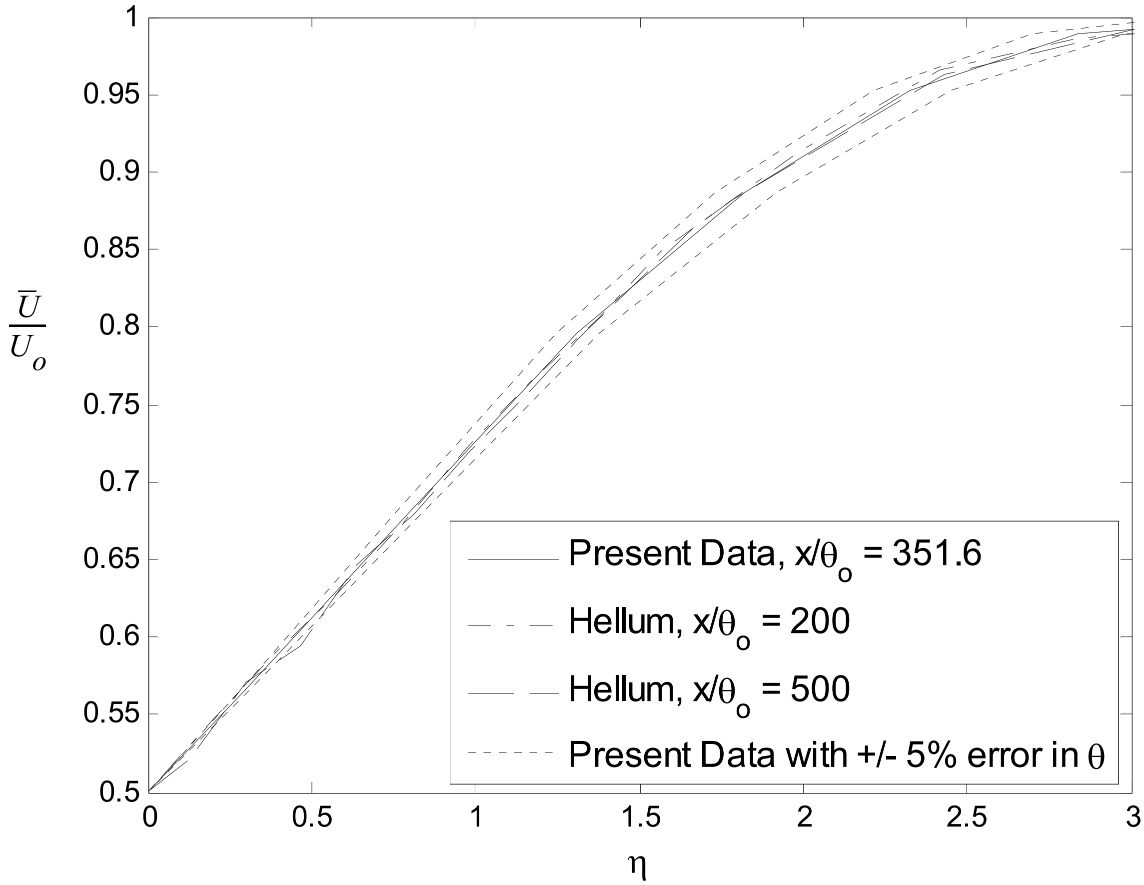

Figure 2.22 Comparison of scaled velocity profiles with one another and with profiles using a known variation in θ, suggesting good consistency between different sets of data for the method used to determine θ.

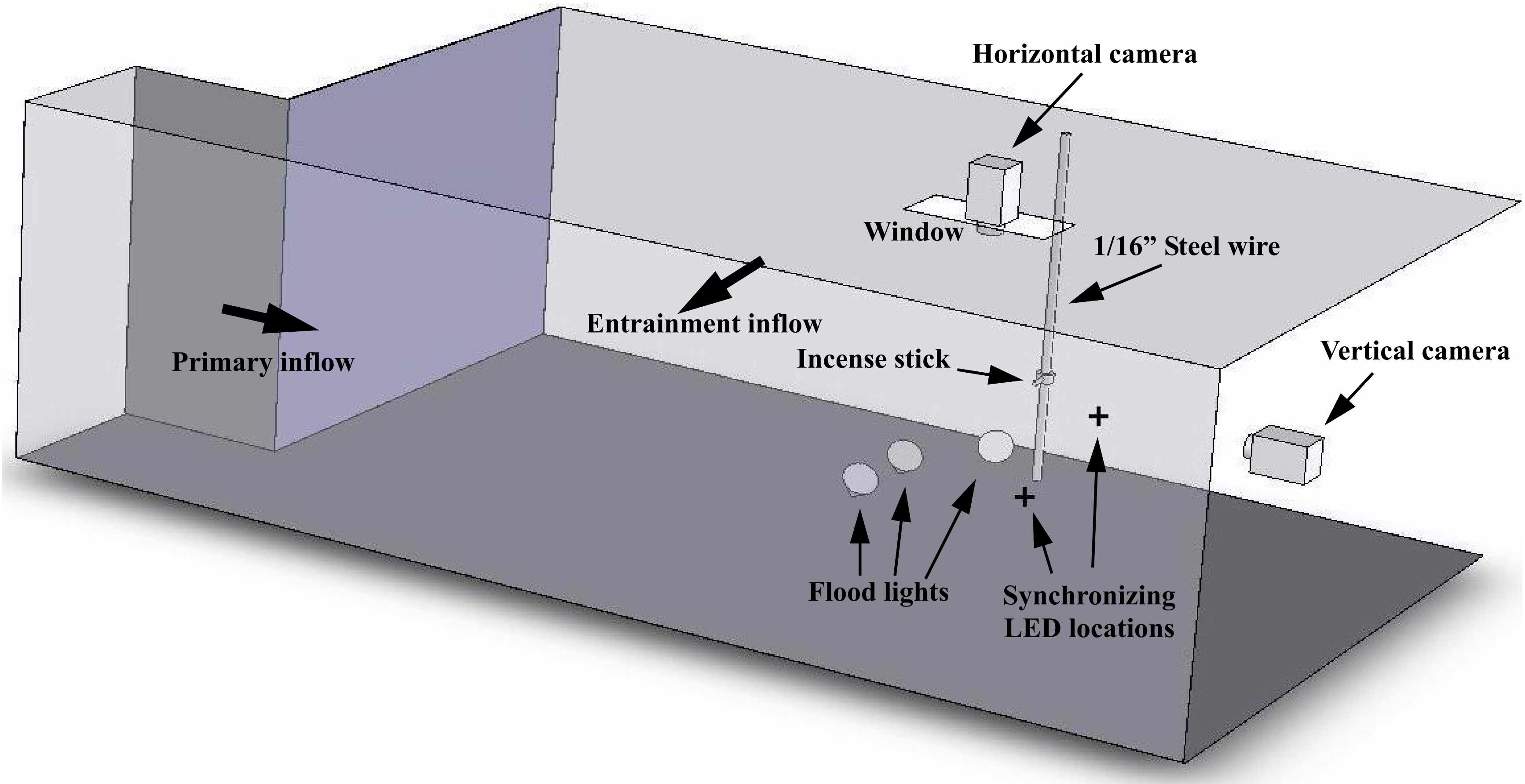

Figure 2.23 Computer model of SSSL facility, showing image acquisition setup.

Figure 2.24 Typical image pairs used to infer success of camera synchronization.

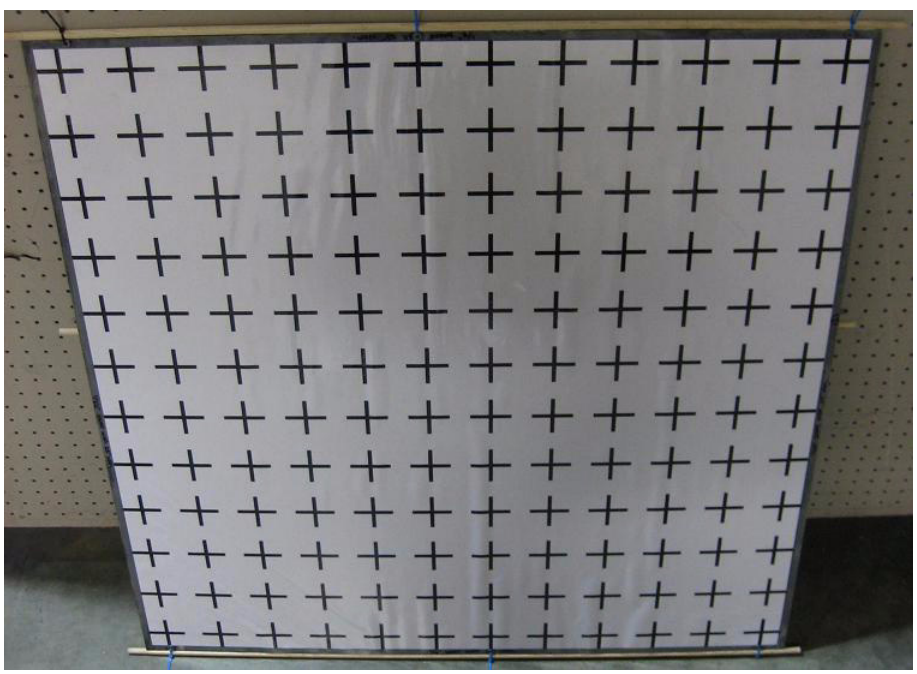

Figure 2.25 2-D image calibration grid.

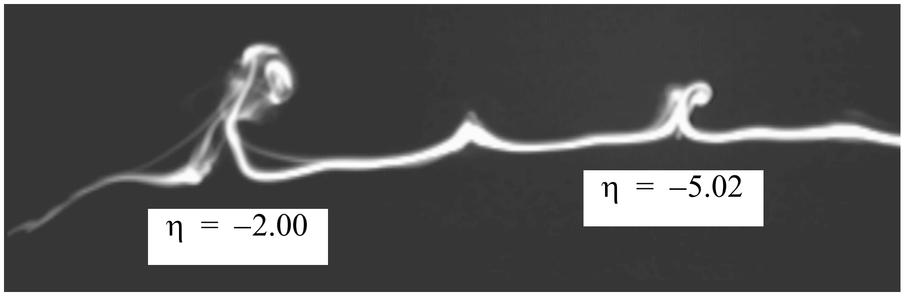

Figure 2.26 Portion of image from horizontal camera, demonstrating thermal plumes resulting from non-uniform heating of streakline fluid due to entrainment fluid "buffeting."

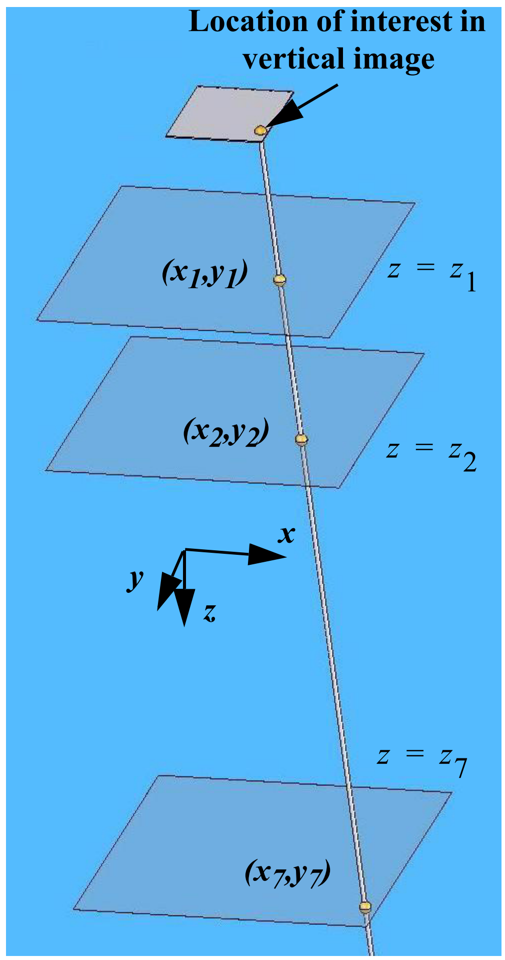

Figure 2.27 Schematic showing mapping of vertical image to various *z*-planes.

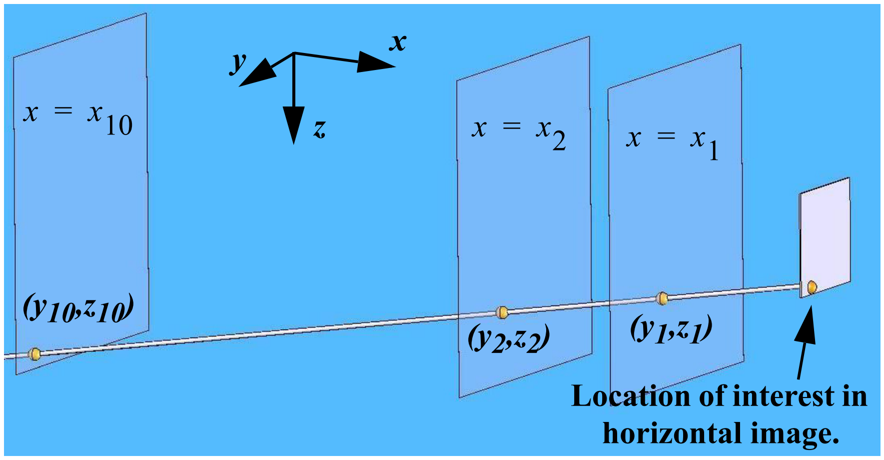

Figure 2.28 Schematic showing mapping of horizontal image to various *x*-planes.

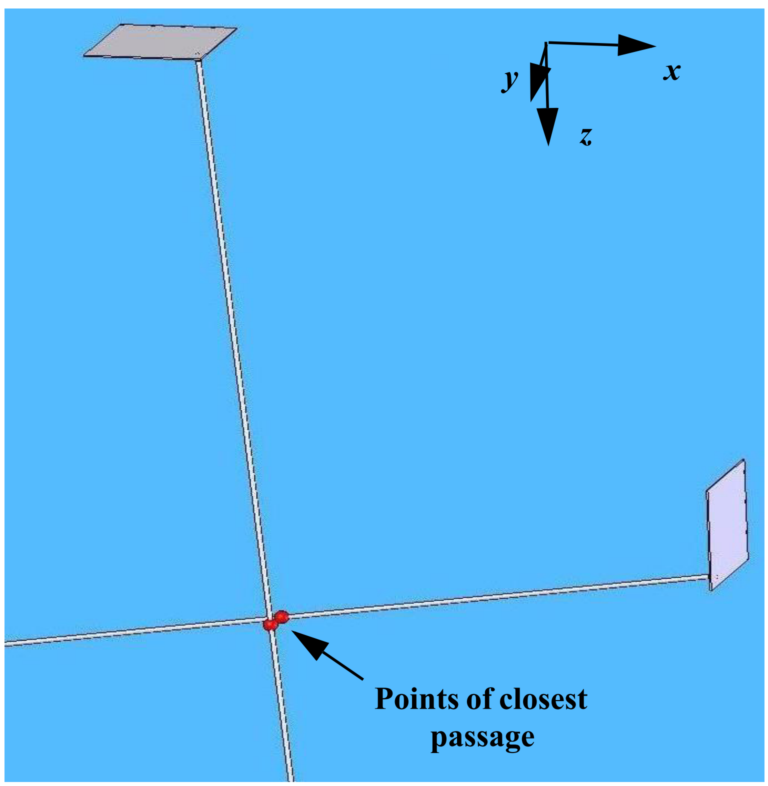

Figure 2.29 Schematic of "intersecting" rays, corresponding to distinct image locations.

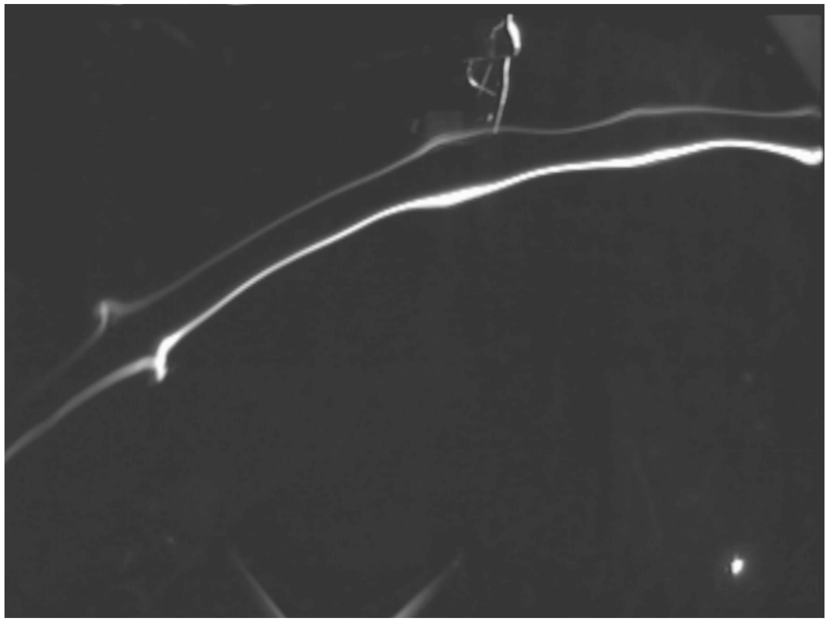

Figure 2.30 Vertical camera image showing streakline stretched across field of view; no termination is apparent. Note the illuminated synchronizing LED in the lower right-hand side of the image.

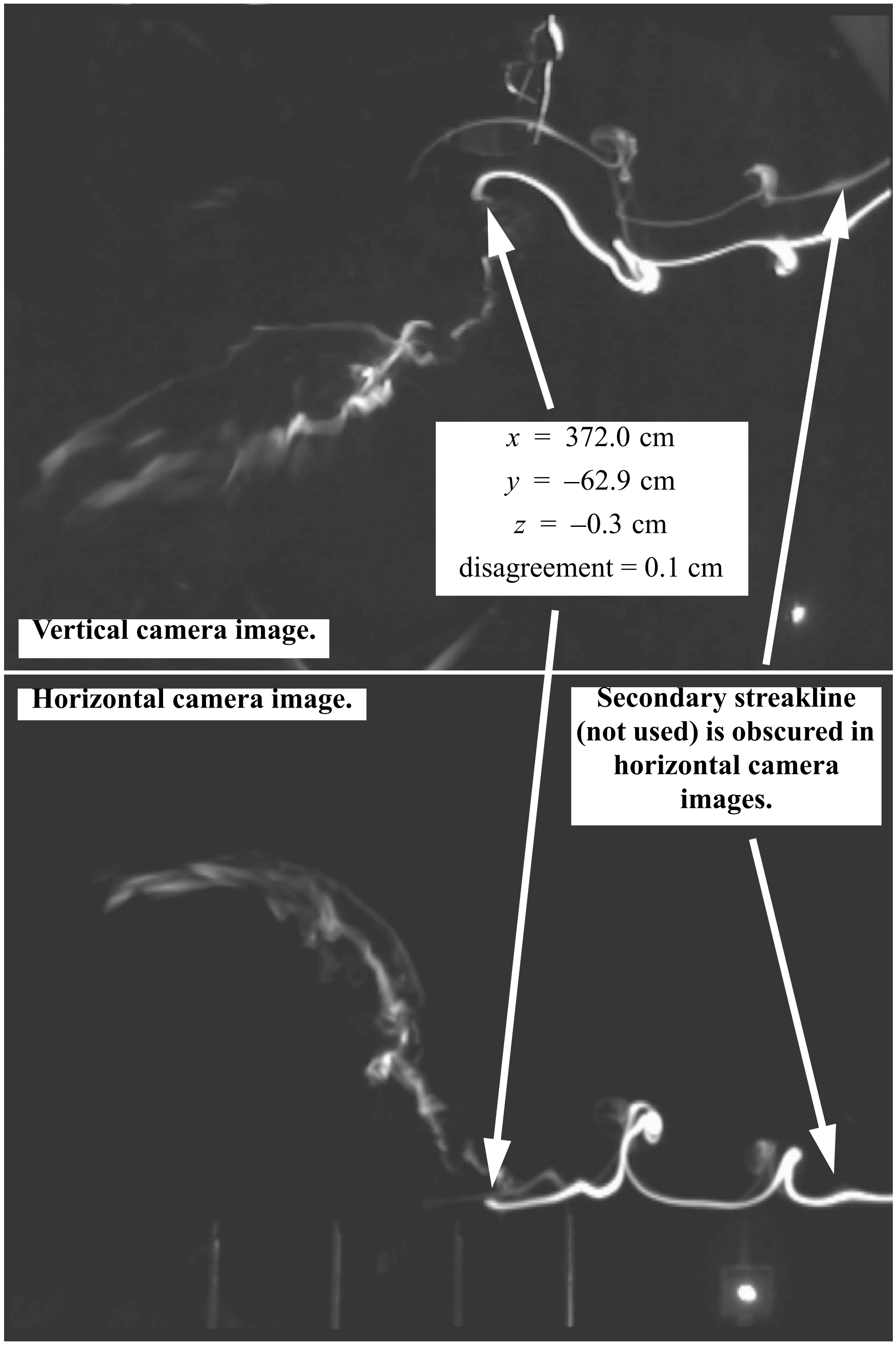

Figure 2.31 Simultaneous image pair demonstrating obvious streakline termination. Note the illuminated synchronizing LEDs in the lower right-hand side of each image.

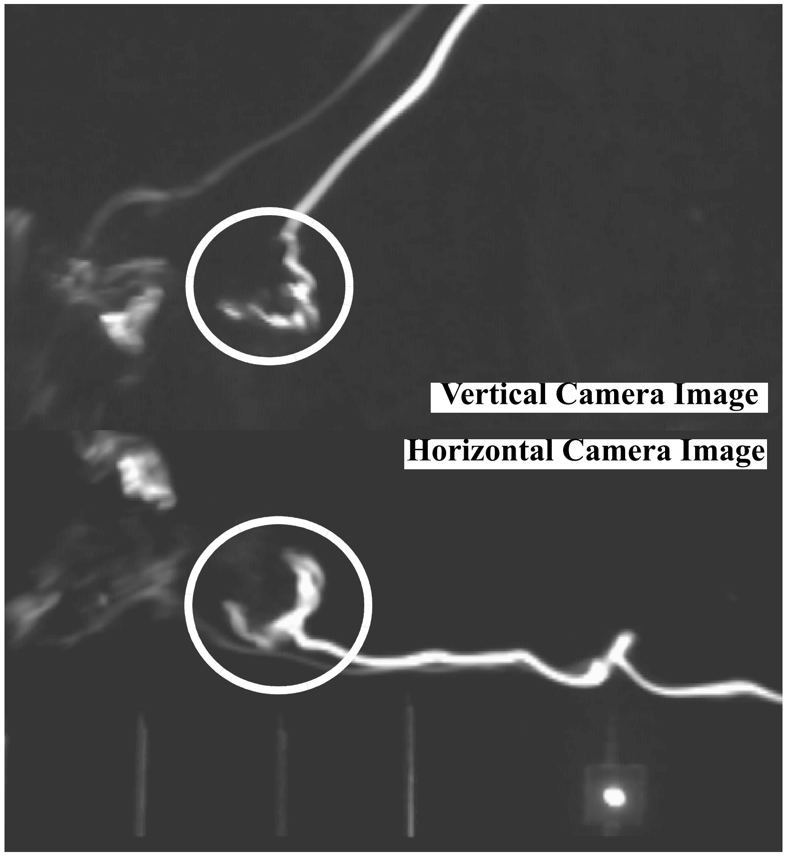

Figure 2.32 Image pair demonstrating ambiguous appearance of "kinked" streakline fluid in vertical camera image. No VSL locations were identified in this image pair.

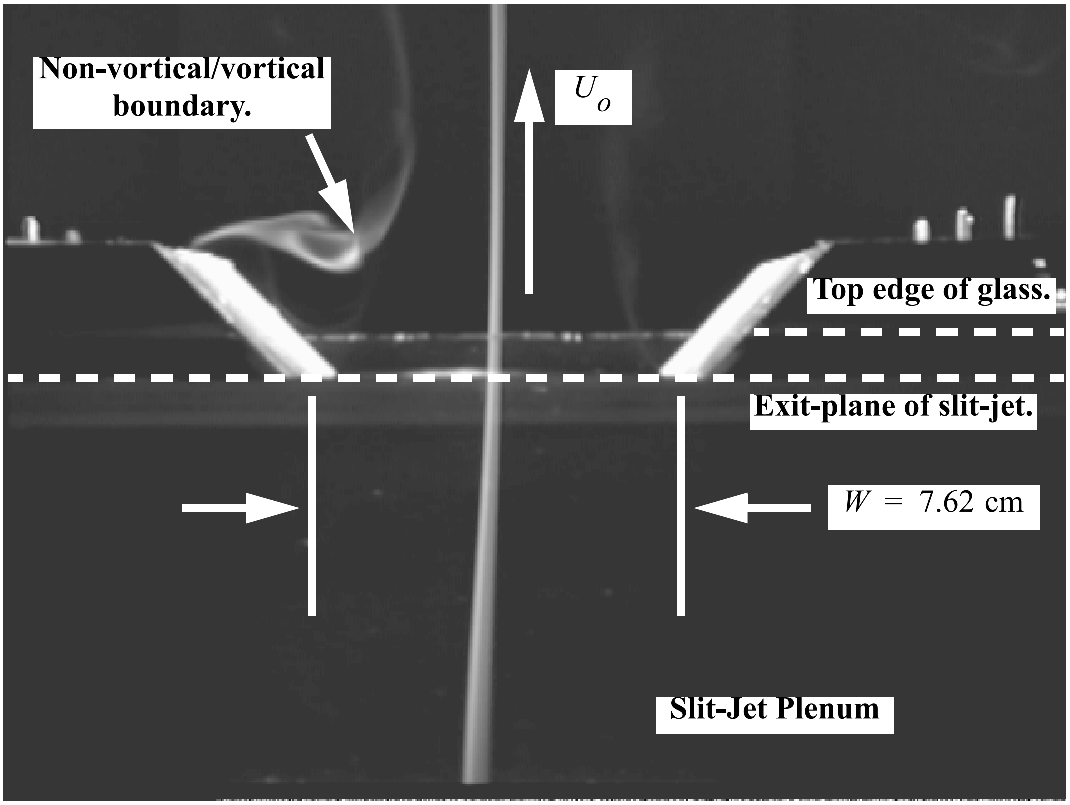

Figure 2.33 "Training" image acquired to allow observation of streakline behavior at the non-vortical/vortical boundary in "controlled" conditions. Note that two streaklines are introduced in this image: centerline and on top of the LHS nozzle block.

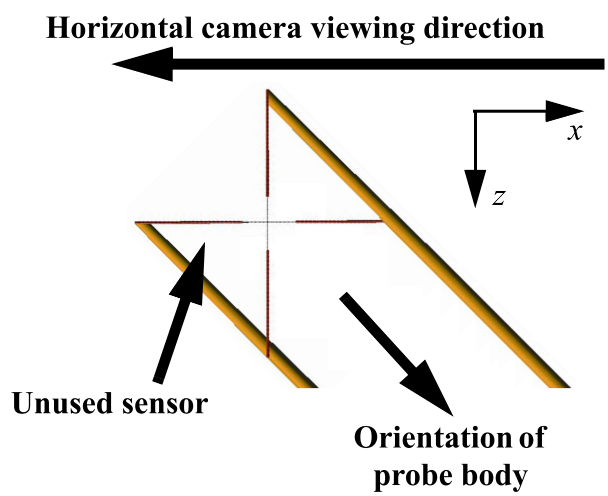

Figure 2.34 Method of preventing probe body from obscuring horizontal camera images.

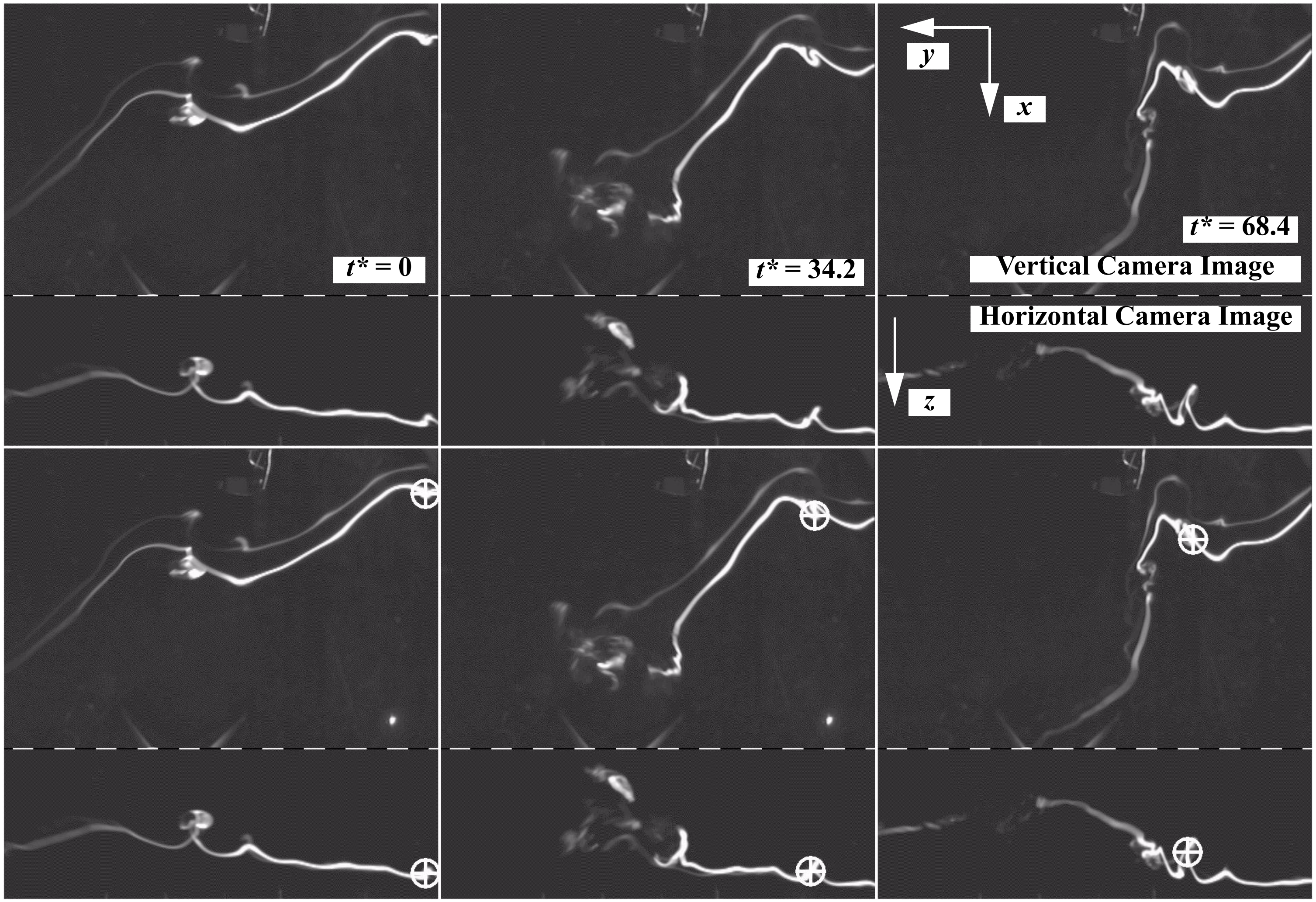

Figure 2.35 Series of image pairs showing a tracked plume approaching the shear layer. The cross-hairs in the bottom row indicate the plume locations as selected by the user. Note that the relative time, $t^* = t(U_o/\theta)$, is also indicated.

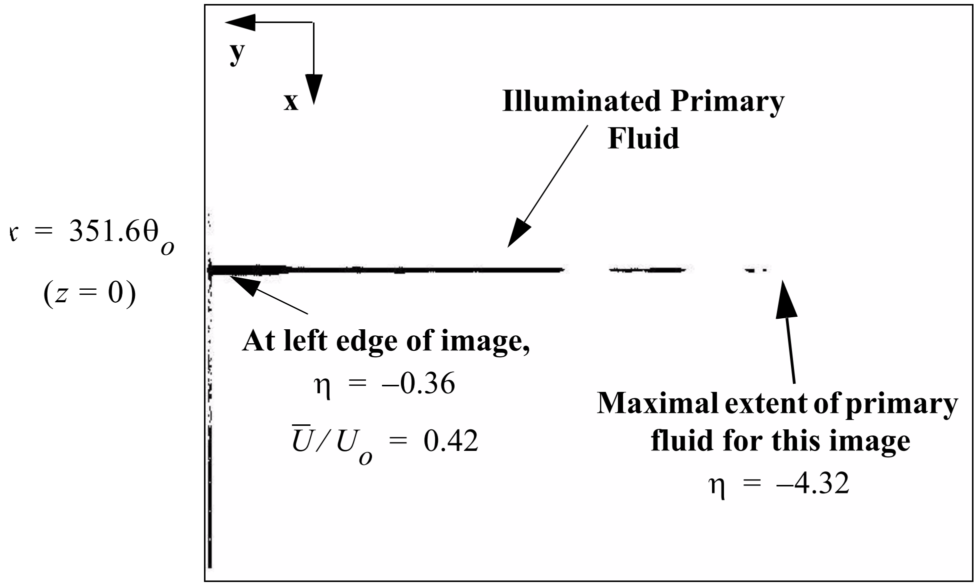

Figure 2.36 Vertical camera image of laser beam being used to illuminate primary fluid (colors have been inverted).

3.0 Experimental Results and Discussion

3.1 Intermittency on the High Speed Side

Figure 3.1 shows the mean value of intermittency, or "intermittency factor" $\bar{I}$, obtained from the ω_z traverse. The present data agree well with the data of Hellum and Foss (2007) for $x = 500\theta_o$ over the high-speed side of the shear layer, and with their data for $x = 200\theta_o$ near the low-speed side: $-1.22 < \eta < -0.72$. The difference in the present data towards the low-speed side may be related to the fact that, in the present experiment, the entrainment fans were operated at a lower drive frequency than in the 2007 experiment. Note that Hellum used a different method to fix the entrainment flow. For the present study, only data obtained at $\eta \geq -1.22$ were used, corresponding to time series for which fewer than 20% of the data points were flagged as "bad;" see Figure 3.2. The practice of flagging such points was discussed in Section 2.3.3.1.

Wygnanski and Fiedler (1970) used a similarity coordinate that will be defined here as $\eta_{WF} \equiv \frac{y - y_{1/2}}{x - x_o}$, where x_o is the "apparent origin" of their shear layer. Data points taken from a scanned image of their $\bar{U}/U_o$ distribution allowed their momentum thickness to be determined as $\theta = 0.045\eta_{WF}$. With this information their data could be scaled in the same manner as the present data. Note that 0.045 is identical to the growth rate, $\frac{d\theta}{dx}$, of their shear layer and that it is substantially larger than the present (nominal) value of 0.035. This was shown to be a result of the trip wire in their boundary layer just upstream of separation.

Figure 3.3 shows that Wygnanski and Fiedler's estimate of the intermittency factor is shifted towards the high-speed side compared to the present data, although the shapes are generally the same. This may be another effect of the trip wire mentioned above, or it may be due to the different criterion function and methodology that they applied in their determination of the intermittency function. They found that an error function with a mean value of 2.4 and standard deviation of 0.80 provided a good fit to the profile of the intermittency factor on the high-speed side. For the present data, the high speed side was well-fit by error functions with a mean of 2.1 and standard deviation 0.84.

3.2 VSL Position Data on the Low Speed Side

A histogram of the observed VSL positions is shown in Figure 3.4. The histogram has a single central "hump," but is decidedly "sharper" in appearance than a Gaussian function. The CDF, shown in Figure 3.5, represents the proportion of observed VSL locations that are equal to or below a given value. The CDF was plotted by first sorting the 492 observed values of η_{VSL} from low to high. The corresponding probabilities were formed as the series of values: $1/492$ to 1, in increments of $1/492$. These probabilities were then scaled as described in Section 2.4.4 to account for streakline terminations that existed off-screen; note that the CDF does not go to 1 at the edge of the visual image $(\eta \approx -0.47)$. The $P(\eta_{VSL} < \eta)$ value of 0.93 at this location represents the fact that the highest 7% of transverse VSL locations were considered to have occurred off-screen.

Corrsin and Kistler (1955) claim that the CDF of the transverse VSL position is equivalent to the intermittency factor, however this is only true for a simplified representation of the VSL that does not include multiple VSL locations at a given (x, z) location;

see the schematic representation on the left side of Figure 3.6. Roshko (1976) argued for the importance of organized, large-scale motions within even high Reynolds number, fully-developed shear layers. As the movement of the VSL is greatly influenced by large motions within the vortical fluid, it is suggested that the schematic representation on the right side of Figure 3.6 provides a more appropriate image of the vortical fluid in the shear layer. In this depiction, it is recognized that the transverse position of the VSL may instantaneously be a multi-valued function of x and z. For this reason, an equivalency between the CDF of the transverse VSL position and the intermittency factor cannot be made.

The CDF of the "measurement disagreements" for these VSL position measurements is shown in Figure 3.7. As discussed in Section 2.4.3, the "measurement disagreement" refers to the spatial distance between the closest points-of-passage of the two lines generated by the vertical and horizontal camera image calibrations. It can be seen that for approximately 90% of observations, the two lines pass within 1 cm of one another. This is about 1.1% of the shear layer width, defined as 6θ. This indicates that the VSL locations that were selected in the vertical camera images are consistent with their counterparts in the horizontal camera images, and lends confidence to the method that was used for identifying the VSL.

3.3 Maximal Extent of the Primary Fluid

Figure 3.8 shows the CDF of the primary-fluid-maximal-extent that was recorded for the the experiments in which the high speed approach flow was marked with an oil fog for each image. Also plotted is the CDF of the VSL-maximal-extent. Specifically, if multiple VSL locations could be observed in an image, only the one closest to the irrotational fluid was retained for that image. It can be seen that over most of the shear layer, the CDF of primary fluid maximal extent is significantly higher. Since the VSL marks the boundary between vortical and non-vortical fluid, and vorticity is diffusive while the seeded particles of the primary flow are not, the relative values of the CDFs for $\eta > -4.5$ were not expected. Note that the tail of the VSL position CDF ($\eta < -4.5$) does extend farther into the irrotational fluid than does the tail of the primary fluid CDF, which is an expected result.

The population of transverse VSL positions at a fixed streamwise location is a fundamentally different statistical quantity from that provided by the streakline method used in this investigation. The streakline method provides a population of transverse locations at which a fluid element originating at some point in the irrotational fluid will be made vortical.

The unexpected comparative CDFs (see Figure 3.8) provide instructive information regarding the irrotational fluid motions that are induced by the vortically active fluid of the shear layer. The coupling between the two bodies of fluid is understood to be a result of the pressure field since the dynamic equation in the irrotational fluid is dominated by the leading terms:

$$\rho \frac{D\vec{U}}{Dt} = -\vec{\nabla} p + \text{negligible viscous terms} \qquad \mathbf{3.1}$$

Using the cartoons of Figure 3.6, the CDFs can be rationalized by noting that the bulge indicates the maximal extent of the primary fluid with the added assumption that the smoke-marked streakline preferentially follows the fluid of the wedge. This qualitative understanding is reinforced by the series of photographic images displayed in Figure 3.9.

These frames, separated by equal time steps, show the strong acceleration of the streak as it extends to relatively high η positions; see $t^* = 16.6$ to 33.3 in the image series. It is inferred that these distinctive motions coincide with the presence of the wedges whereas the dwell periods (see $t^* = 43.3$ to 56.6) indicate the bulges.

3.4 Concurrent VSL Position and Hot-Wire Data

For an arbitrary, time-dependent variable α, the autocorrelation function is defined as:

$$R_{\alpha\alpha}(\tau) \equiv \frac{\overline{\alpha(t)\alpha(t+\tau)}}{\overline{\alpha^2}}. \qquad \mathbf{3.2}$$

The autocorrelation was formed for the voltage from each of the two reference sensors that were placed up and downstream of the VSL position measurement domain. The location of the first peak in the autocorrelation provided an estimate of the "preferred period" of the large-scale motions at the location of the sensor; see Figure 3.10. The sensor located at $x/\theta_o = 306.6$ indicates its first peak at a value of $\tau_{peak}^{auto} = 0.66$ s, while the reference sensor located at $x/\theta_o = 382.7$ indicates its first peak at $\tau_{peak}^{auto} = 0.77$ s. A local Strouhal number can be defined based on the local momentum-thickness of the shear layer and the free-stream velocity as

$$St = \frac{f_m \theta}{U_o}, \qquad \mathbf{3.3}$$

where $f_m = 1/\tau_{peak}^{auto}$. The Strouhal numbers indicated at these two locations are respectively 0.027 and 0.028. These are slightly higher than the mean value of 0.024 reported by

Hussain and Zaman (1985) over several locations in their facility, but are still within the apparent scatter of their data. Morris (2002) additionally obtained a value of 0.026 in the fully-developed region of this facility at $x/\theta_o = 600$.

The cross-correlation of two arbitrary, time-dependent variables α and β is defined as:

$$R_{\alpha\beta}(\tau) \equiv \overline{\alpha(t)\beta(t+\tau)}. \qquad \textbf{3.4}$$

The cross-correlation of the voltages from the upstream and downstream reference sensors was formed. The location of the highest peak in the cross-correlation provided an estimate of the "convection time" for the large-scale motions; see Figure 3.11. For these two sensors, the peak in the cross correlation occurred at $\tau_{peak}^{cross} = 0.23\ \text{s}$. Given their locations at $x = 337.2\ \text{cm}$ and $x = 421.0\ \text{cm}$, this corresponds to a convection speed of $U_c = 3.59\ \text{m/s}$. This is close to the expected value of $U_c = U_o/2 = 3.75\ \text{m/s}$. The convection speed and the "preferred periods" that were obtained from the autocorrelation functions jointly imply a streamwise spacing of the large motions equal to $U_c\tau_{peak}^{auto}$. At $x/\theta_o = 306.6$ and $x/\theta_o = 387.7$ this quantity is equal to 2.38 m and 2.78 m, respectively. These values are respectively 2.98 and 2.86 times the local, nominal shear layer width of $6\theta(x)$. In terms of vorticity thickness they are equal to 4.06 and $3.90\delta_\omega$, and these are in good agreement with the value of $3.9\delta_\omega$ obtained by Koochesfahani et al. (1979) for the large structure spacing in their two-stream shear layer.

The interest in acquiring concurrent hot-wire data with the VSL positions was motivated by the desire to identify a representative "signature" for the passage of a billow or wedge, so that the behavior of the streakline could be observed. A qualitative examination of the time series for the sensors reveals some patterns.

Figure 3.12 shows a portion of the voltage time series for the upstream and downstream reference sensors. The mean values have been subtracted since the fluctuations are of interest. It is obvious that the signal from the upstream sensor is very similar to a shifted version of the signal from the downstream sensor.

The "swells" in the sensors' signals, during which the voltage increases to a local maximum and decreases again, appear to be more protracted than the local minima that separate them. Figure 3.6, introduced earlier, is again instructive; the advance of the streakline towards the shear layer is seen to be comprised of two distinct types of motion that can be intuitively associated with the swells and minima in the reference sensor signals: 1) The streakline is accelerated towards the higher speed fluid, and undergoes significant axial strain in the y-direction. Typically this motion is accompanied by a positive x-velocity. It was during events such as this that the streakline would occasionally extend beyond the cameras' field of view, as in Figure 2.30. 2) The advance of the streakline to higher (x, η) values would then stop abruptly, and a negative x-velocity might be briefly observed until the first motion (1) was again initiated.

It is considered to be apparent that the "swells" in the voltage time series of the reference sensors are associated with the first type of motion, which might be called an "ingestion" event. This was understood to indicate the passage of a wedge of irrotational fluid, as shown in the cartoon depiction of the VSL in Figure 3.6. The local minima separating these swells, and the abrupt halting of the streakline motion, were understood to be associated with the passage of large structures or “bulges” of vortical fluid.

This picture is reinforced by an examination of portions of the velocity time series from the calibrated sensors in the rake; see Section 2.4.6. These are shown in Figure 3.13 along with the (scaled and offset) voltage signals from the reference sensors. It can be seen that at the top of the downstream reference sensor’s swell, the velocities indicated by the three rake sensors enter a relatively long period of quiescent flow, typically with a decreasing velocity. One might associate this period of quiescent fluid with a wedge sweeping over the rake of three sensors.

An initial question was: “As a wedge is convected through the measurement domain, can the streakline be shown to follow it? An attempt was made to identify wedge-passing events in the time series as follows:

1) The passage of a wedge was inferred by observing the rake sensors. When the three rake sensors all became visibly quiescent, the signals from the reference sensors were examined.

2) The local maximum corresponding to the start of the quiescent period in the rake sensors was identified in the downstream reference sensor’s signal. As long as no pairing events or other irregularities were indicated between this maximum and the corresponding maximum in the upstream reference sensor’s signal, the time required for the event to travel from the upstream end of the measurement region was inferred as the elapsed time between these two maxima.

3) The end of the event was defined as the point in the time series at which all the rake sensors appeared to have entered the wedge. This was assumed to indicate that the wedge had begun to cross out of the field of view at the downstream end of the domain.

4) The beginning of the event was defined to precede the end of the event by the convection time obtained in step (2). This was assumed to roughly indicate the time at which the wedge would have been crossing into the field of view on the upstream side of the measurement region.

5) The camera images corresponding to the identified sections of time series were examined.

The 30 seconds of image data acquired corresponds to roughly 42 large structure cycles, based on the values of τ_{peak}^{auto}. From the procedure above, looking at the time series only provided 8 events, two of which are shown in Figure 3.14. However, the images associated with those 8 events all depicted the streakline in the process of being accelerated in the y-direction, corresponding to the motion that had been hypothesized as the result of a passing wedge. This provided confidence that the streakline behavior in the images could at least be correlated with a recognizable feature of the time series.

The process for identifying events was then performed "in reverse," i.e. the image record was examined, and ranges of images were identified in which it seemed that a wedge was passing through the measurement region. This was a more subjective assessment. Only events wherein the streakline was pulled all the way across the field of view were used, in the hopes that the associated features of the time series would be exaggerated. This yielded 18 events, for which the associated time series record was examined. Three of the eight events identified using the time series did not coincide with any of the events identified using the images. The events identified using the images were generally longer in duration, with a mean of $24\theta/U_o$, and exhibited a wider range of durations, with a standard deviation of $8\theta/U_o$. The events identified using the time series, by comparison, had a mean duration of $10.5\theta/U_o$ and standard deviation of $1.6\theta/U_o$. This should not be surprising since their durations were fixed using an inferred convection time that was quite consistent over the time record.

It was determined that the events identified using the image series had a generally consistent relation to the signals from the reference sensors, so that defining the passage of a wedge might best be done strictly in terms of these signals, without the rake sensors. This possibility is still being investigated.

3.5 Velocity Statistics from Tracking of Plumes

The record of 1800 images featured 42 unique plumes (note that this number is identical to the number of large structure cycles, 42, that was estimated above from the values of τ_{peak}^{auto}). This is expected since the formation of a plume is attributed to a large motion passing in the shear layer. On average, a plume would remain identifiable for ~103 images so that the 42 plumes provided 4,446 position values and 4,345 velocity values over the course of the image record.

PDFs and joint PDFs were calculated for various quantities by first forming their histogram (or joint histogram) using an appropriate number of “bins.” The histogram counts were then divided by the total number of samples to yield the fraction of observations in each bin. These fractions (nominal probabilities) were then divided by the bin spacing in order to approximate the probability density. Figure 3.15 shows a joint PDF of all the x and y locations that were occupied by plumes throughout the image record. For comparison, the joint PDF of the x and y-locations at which the VSL was observed are shown in Figure 3.16. The VSL locations obviously tend to occupy transverse locations that are closer to the high speed side than those of the plumes. Their streamwise extent is also significantly greater than that of the plumes. A slight positive correlation is apparent in both plots. Note that the x and y extents of both joint PDFs represent the x and y extents of the measurement region.

It is additionally revealing to view the x and y-locations of the plumes as a scatter plot instead, as shown in Figure 3.17. Plumes that are moving at lower velocities provide a greater number of observations per distance traversed, so that the character of the joint PDFs tends to be dominated by the large number of observations far from the active shear layer. In the scatterplot, the tendency of the plumes to move forward as they are accelerated towards the active shear layer is more apparent, and the trajectories of multiple individual plumes are suggested. The individual plume trajectories may be capable of providing additional information concerning the large motions in the active fluid, and this is currently being investigated.

Figures 3.18 and 3.19 show PDFs of the U and V velocity components obtained by tracking the plumes in the entrainment stream. $\langle W \rangle$ (not shown) is slightly negative, reflecting the plumes' tendency to continue rising, albeit slowly, throughout their lifetime. $\langle V \rangle / U_o$ is 0.037, which agrees reasonably well with the targeted condition: $V_e / U_o = 0.035$ that was used to set the entrainment fans. $\langle U \rangle$ is slightly positive, and the PDF of U exhibits a slight positive skewness. The joint PDF of U and V suggests no strong correlation between these two components.

Examination of the joint PDF for U and η, shown in Figure 3.21, indicates that this positive skewness of the PDF for U likely comes from the population close to the active shear layer $(-3 < \eta < -2.5)$. The scatterplot of these data, shown in Figure 3.22, is again more revealing. The apparent dramatic increase in U that plumes tend to experience close to the active shear layer is consistent with the character of the plume trajectories suggested by the scatterplot of their x and y locations in Figure 3.17. This provides another indication that the streakline is swept forward during “ingestion” events of the first type discussed above, so that observations of the VSL location preferentially occur in wedges.

Figure 3.23 contains the joint-PDF for V and η. It is perhaps surprising that the standard deviation of this population does not appear to increase more as the shear layer is approached.

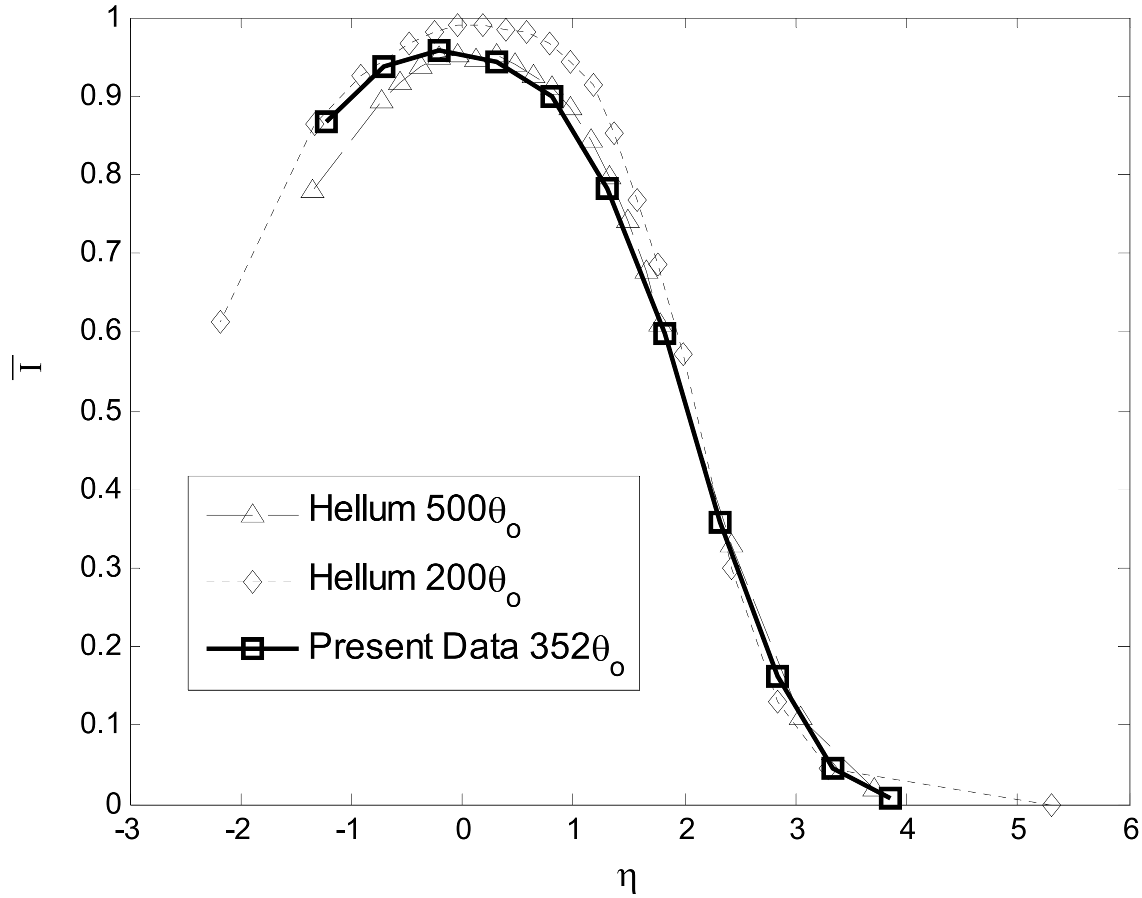

Figure 3.1 Comparison of intermittency factor for present data with those of Hellum and Foss (2007). Note the apparent decrease with streamwise distance near the shear layer center.

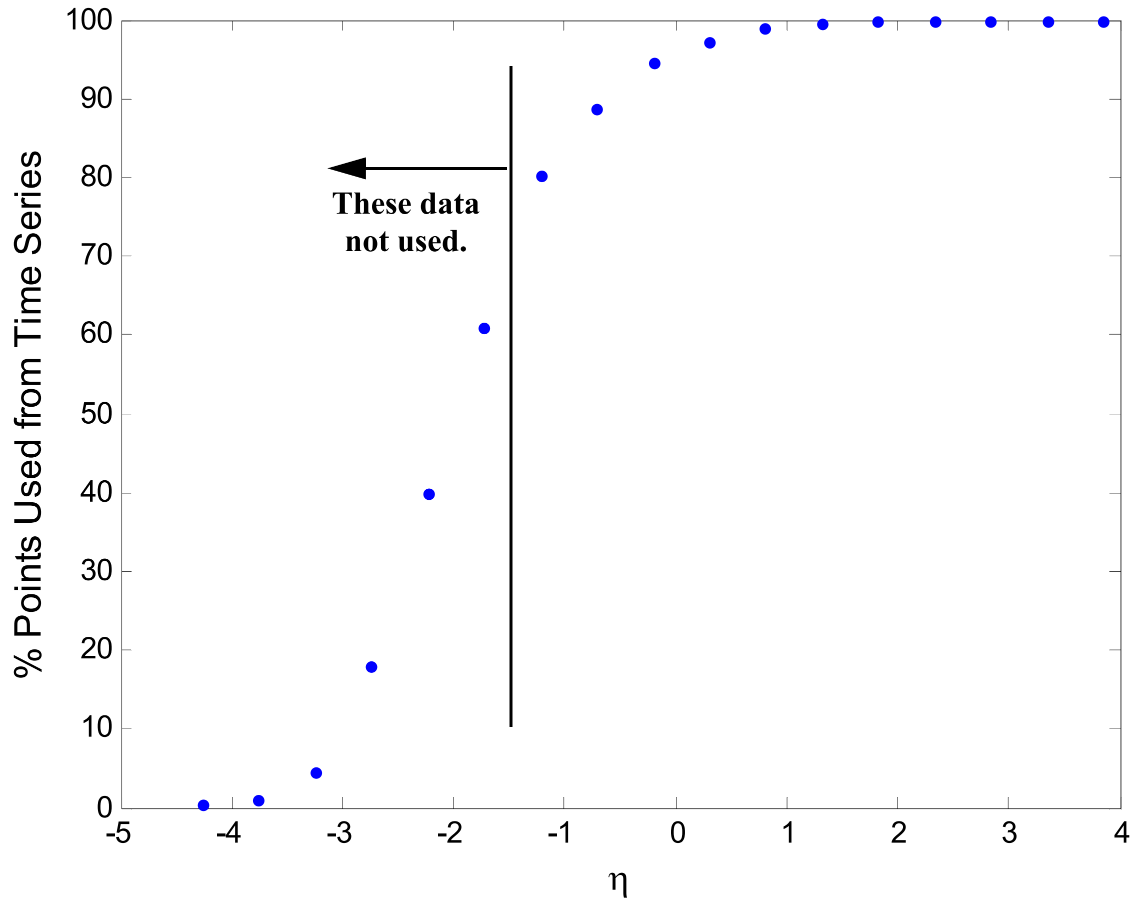

Figure 3.2 Percentage of hot-wire time series points that could be used at each transverse location.

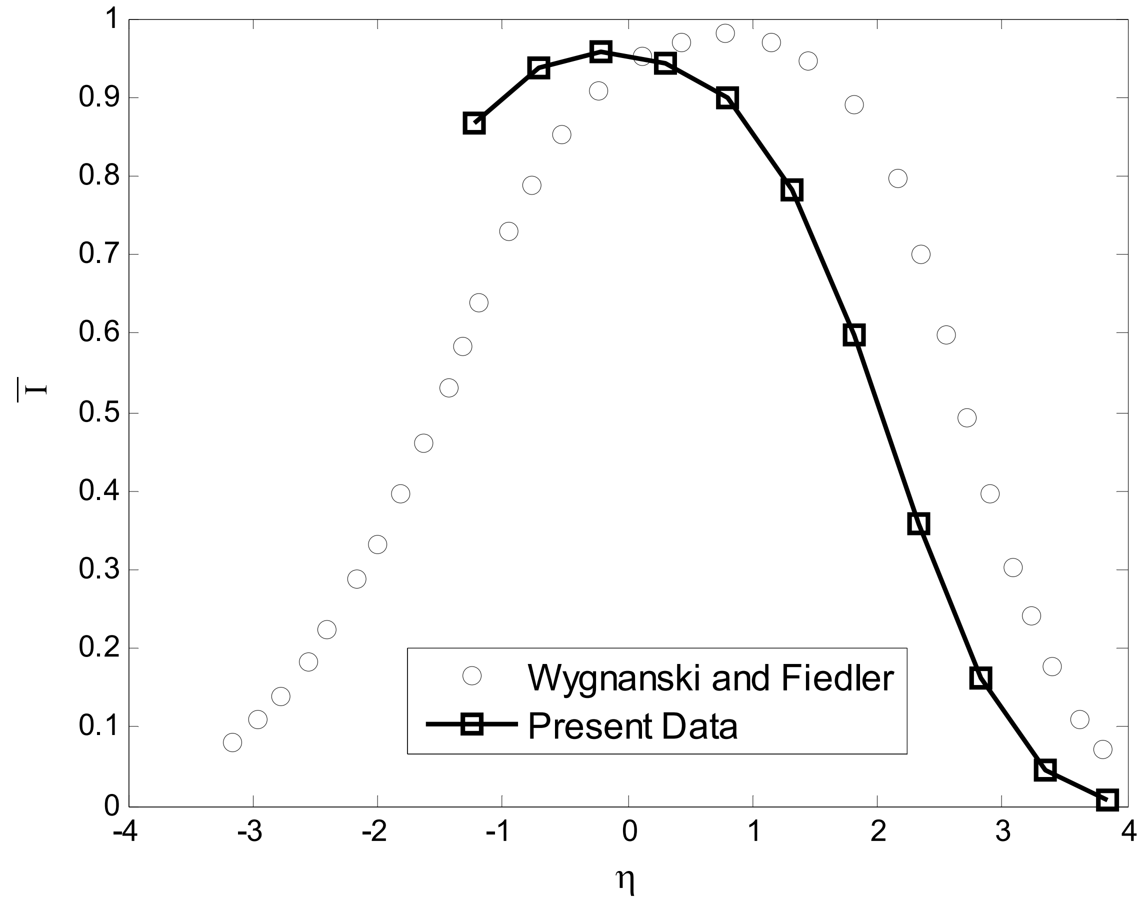

Figure 3.3 Comparison of hot-wire-based intermittency factor with that of Wygnanski and Fiedler (1970).

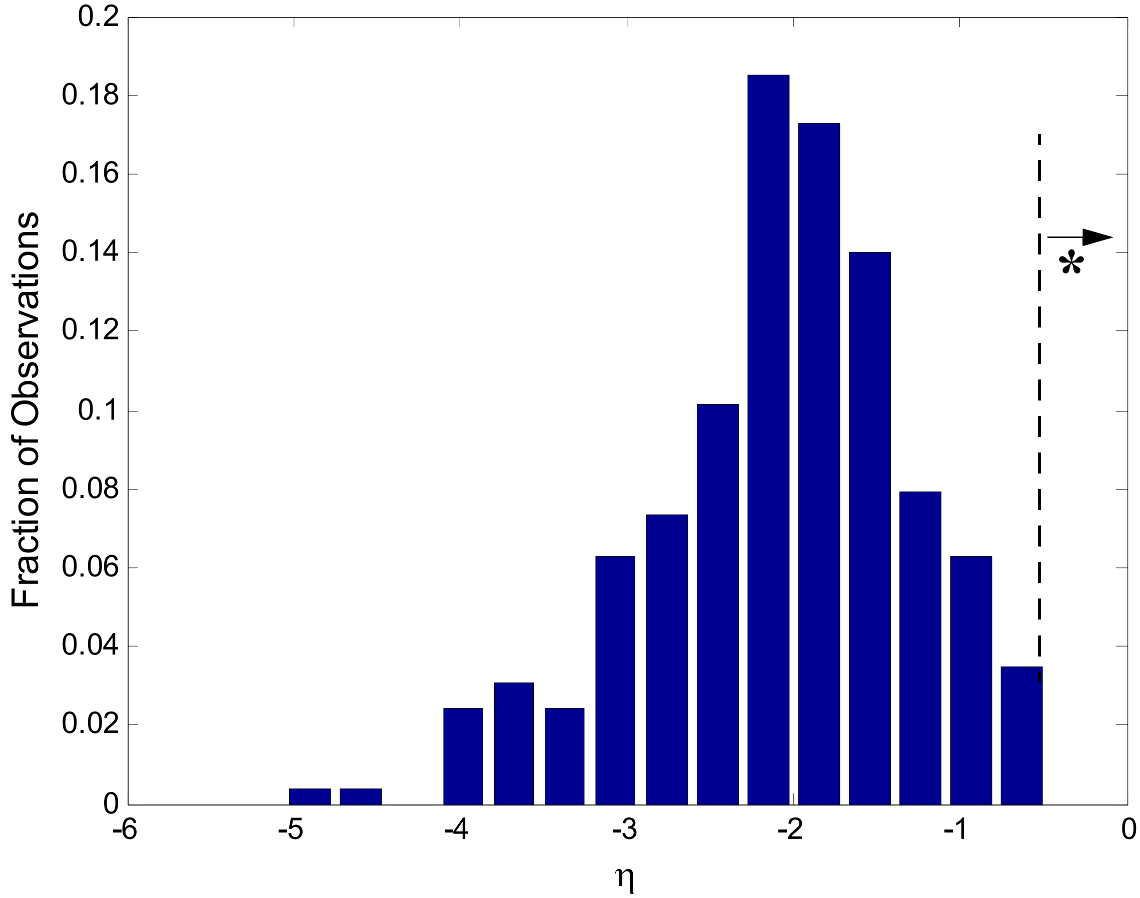

Figure 3.4 Histogram of VSL position from streakline measurements. Note * is beyond the fields of view of the cameras.

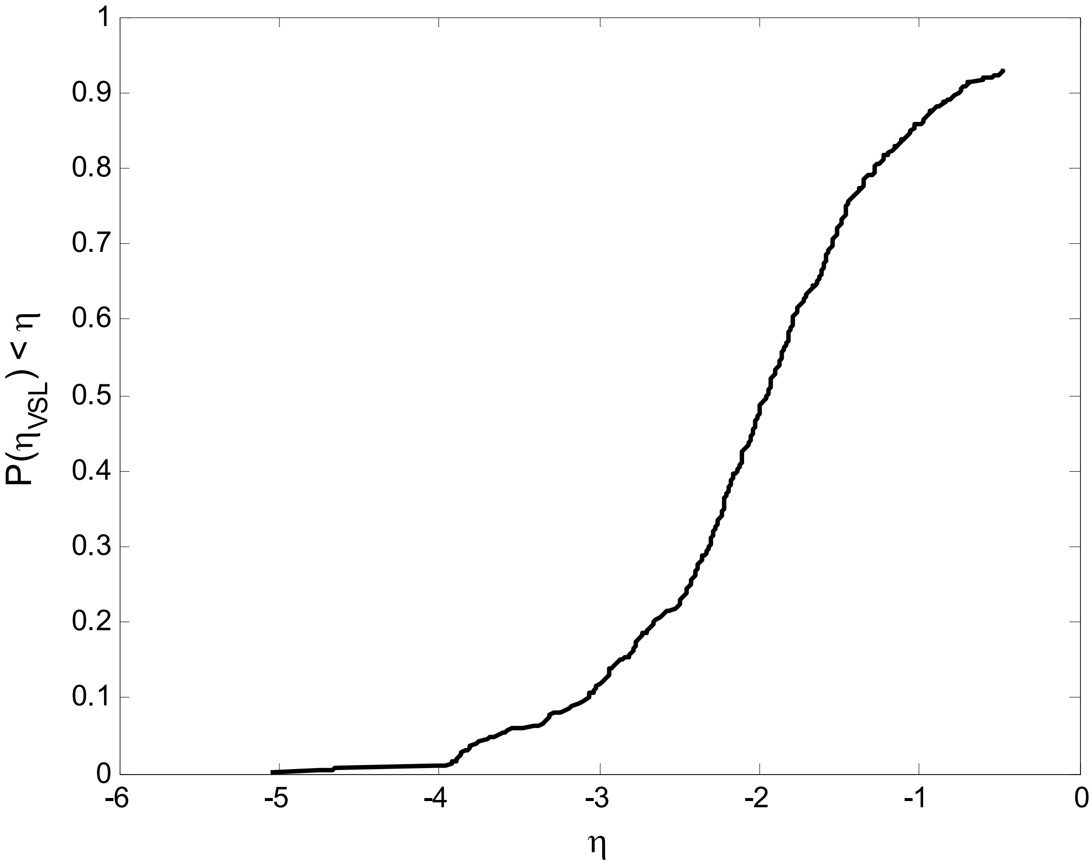

Figure 3.5 CDF of VSL position from streakline measurements. Note: see Section 2.4.4 regarding the peak value that is < 1.

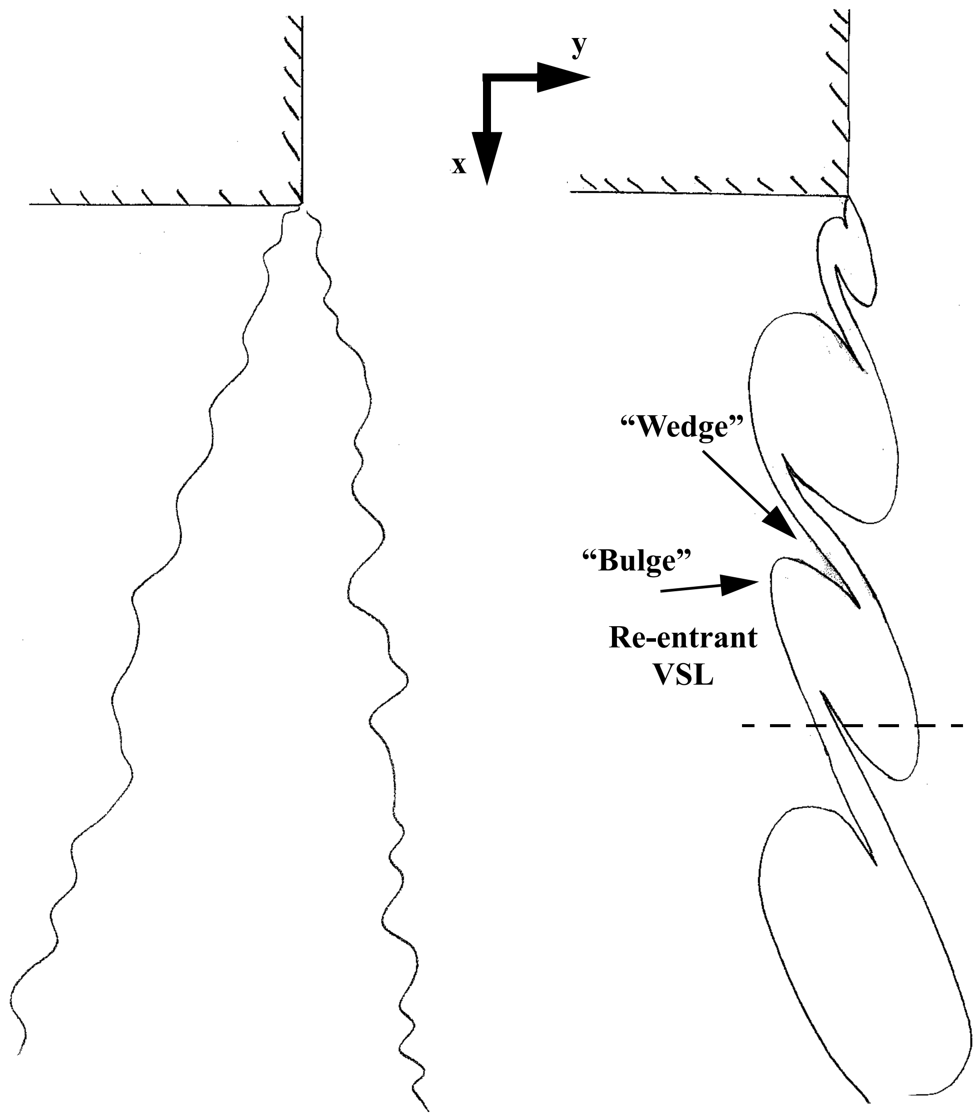

Figure 3.6 Illustrative cartoons of the shear layer depicting an older conception (left) and more modern conception (right).

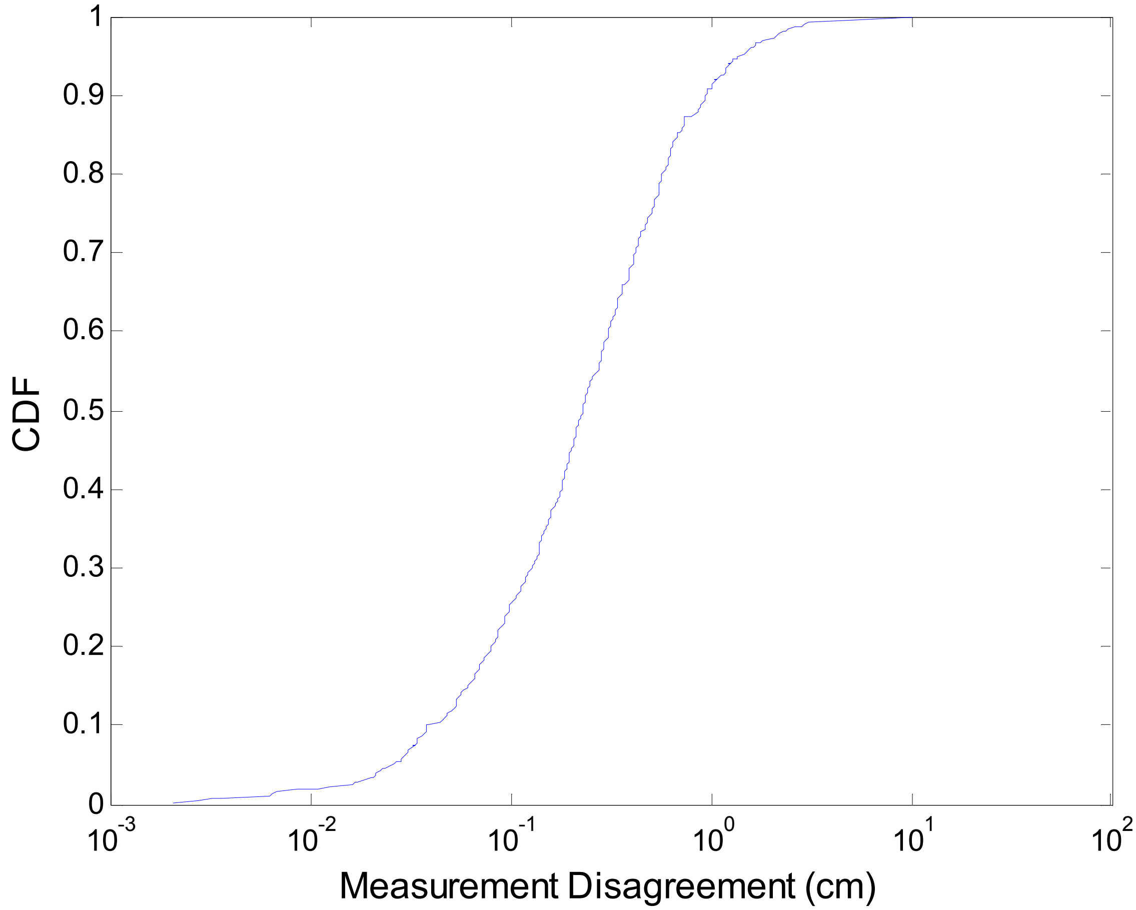

Figure 3.7 CDF of Measurement Disagreements for VSL position observations.

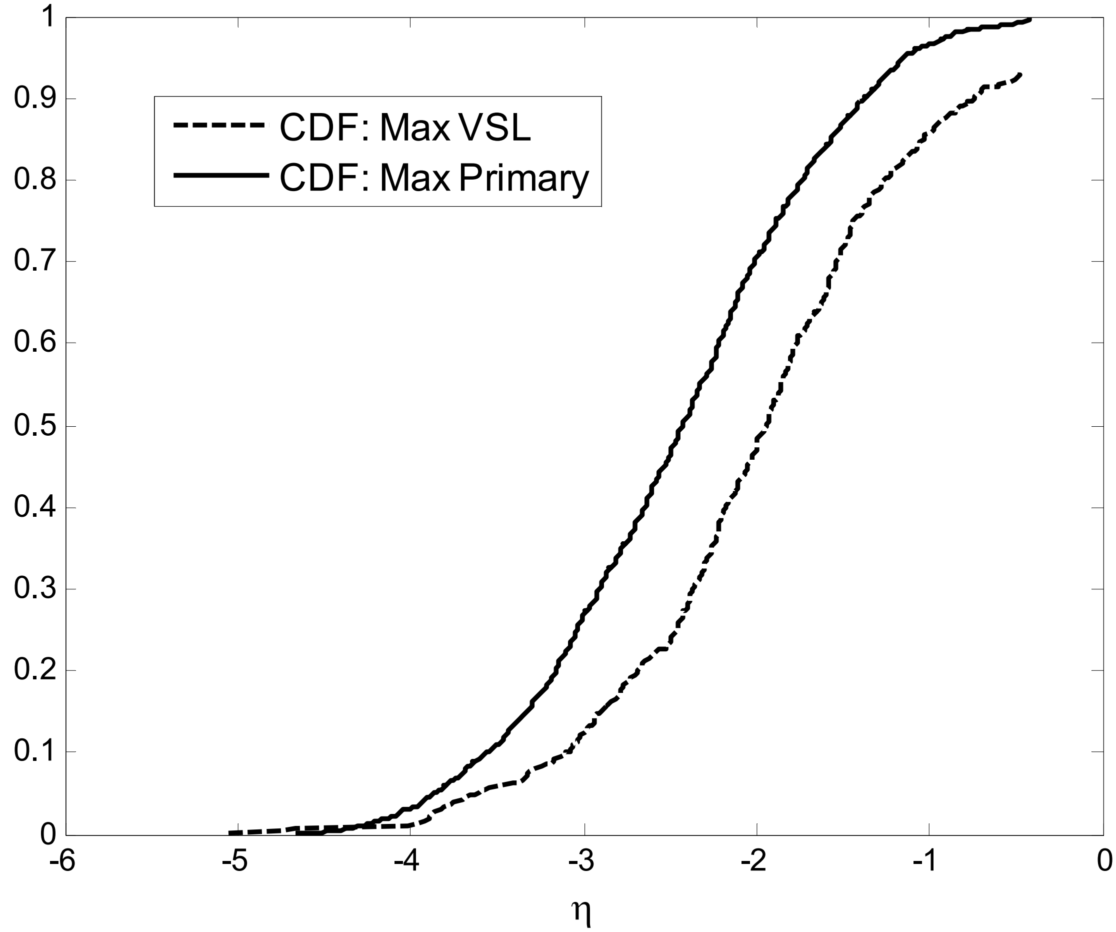

Figure 3.8 Comparison between CDFs of maximum primary extent towards the irrotational fluid, and maximum VSL extent

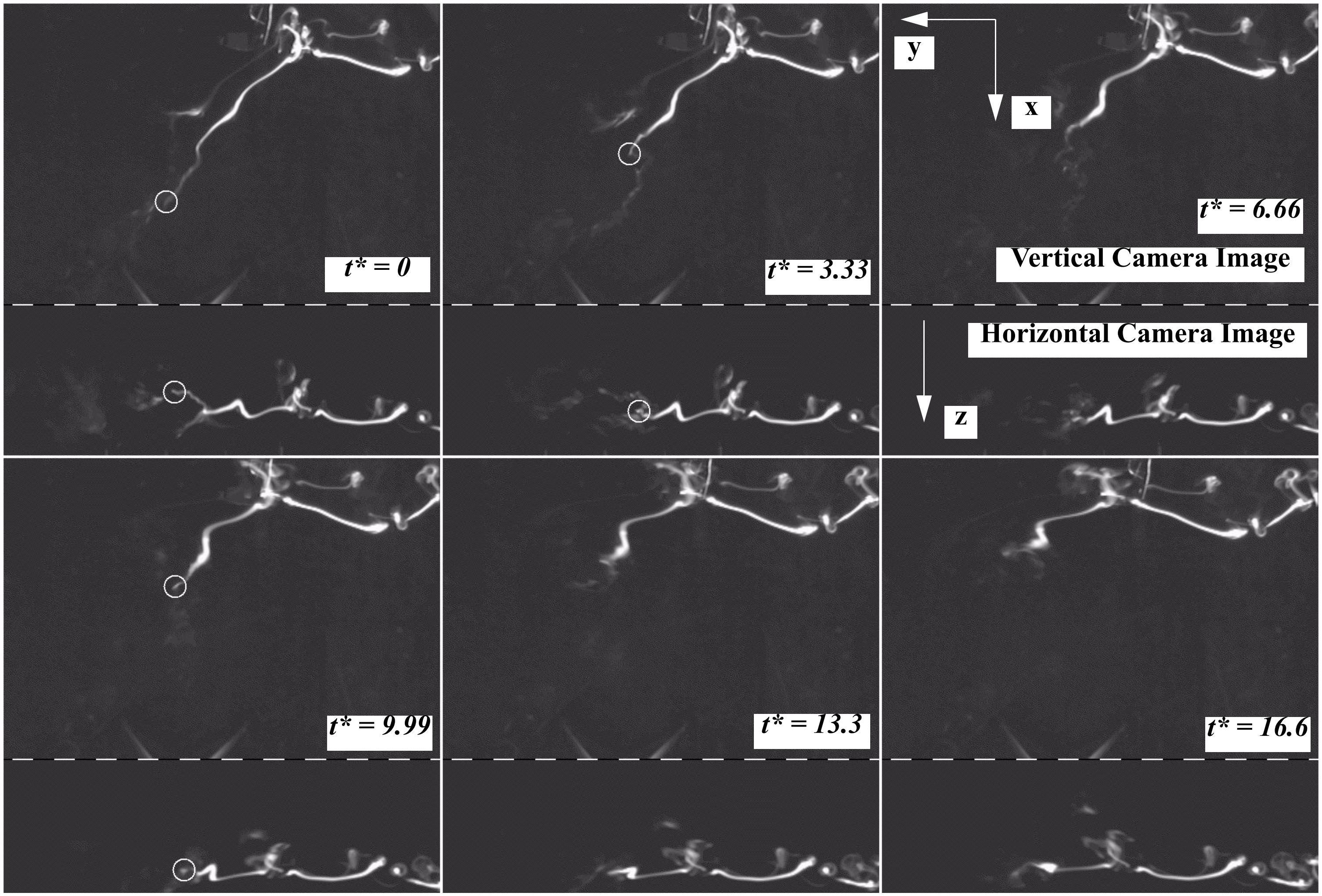

Figure 3.9 Motion of the streakline as described on page 80. The relative time, $t^* = tU_o/\theta$, of each frame is indicated. Inferred VSL locations are circled.

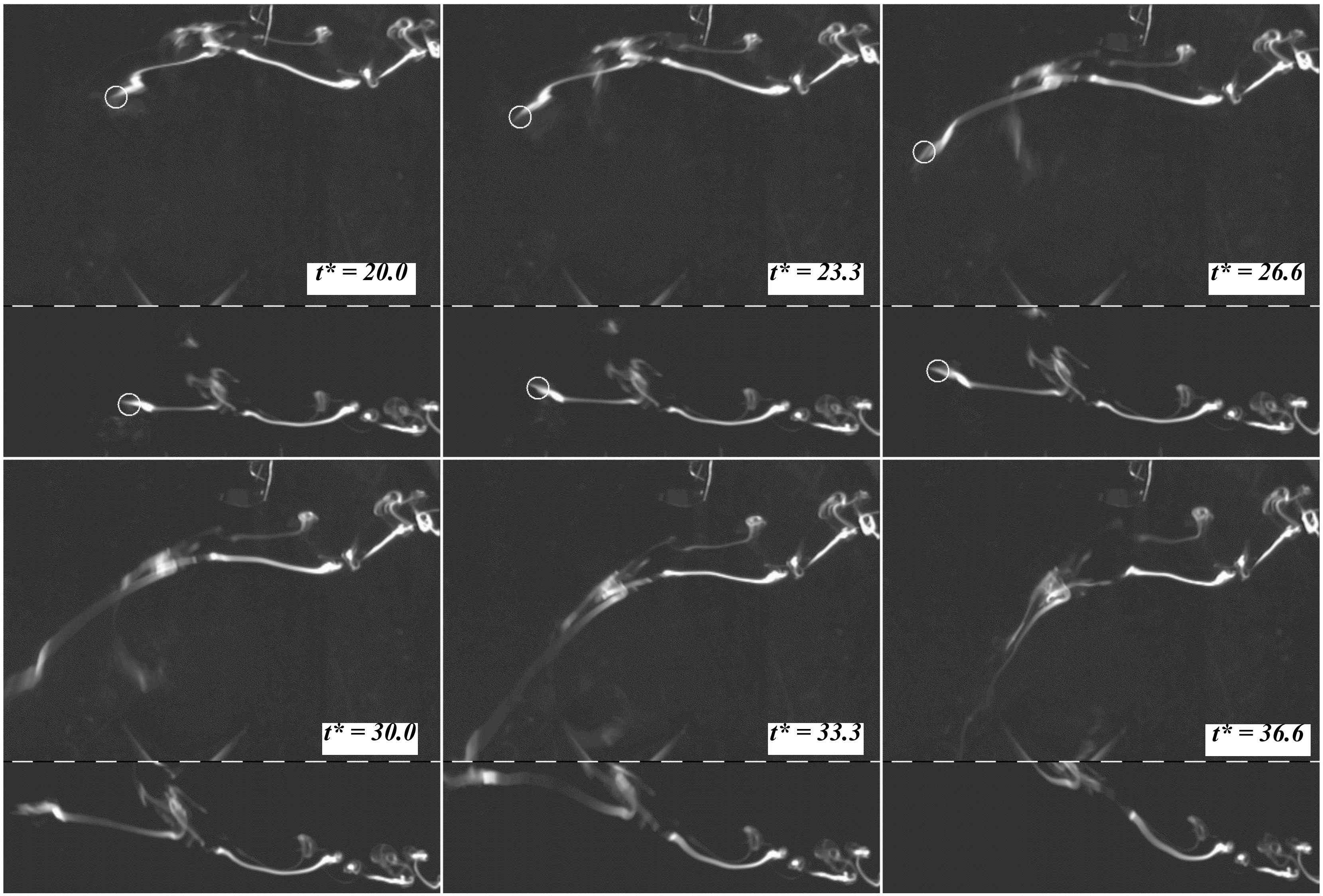

t* = 20.0
t* = 23.3
t* = 26.6
t* = 30.0
t* = 33.3
t* = 36.6

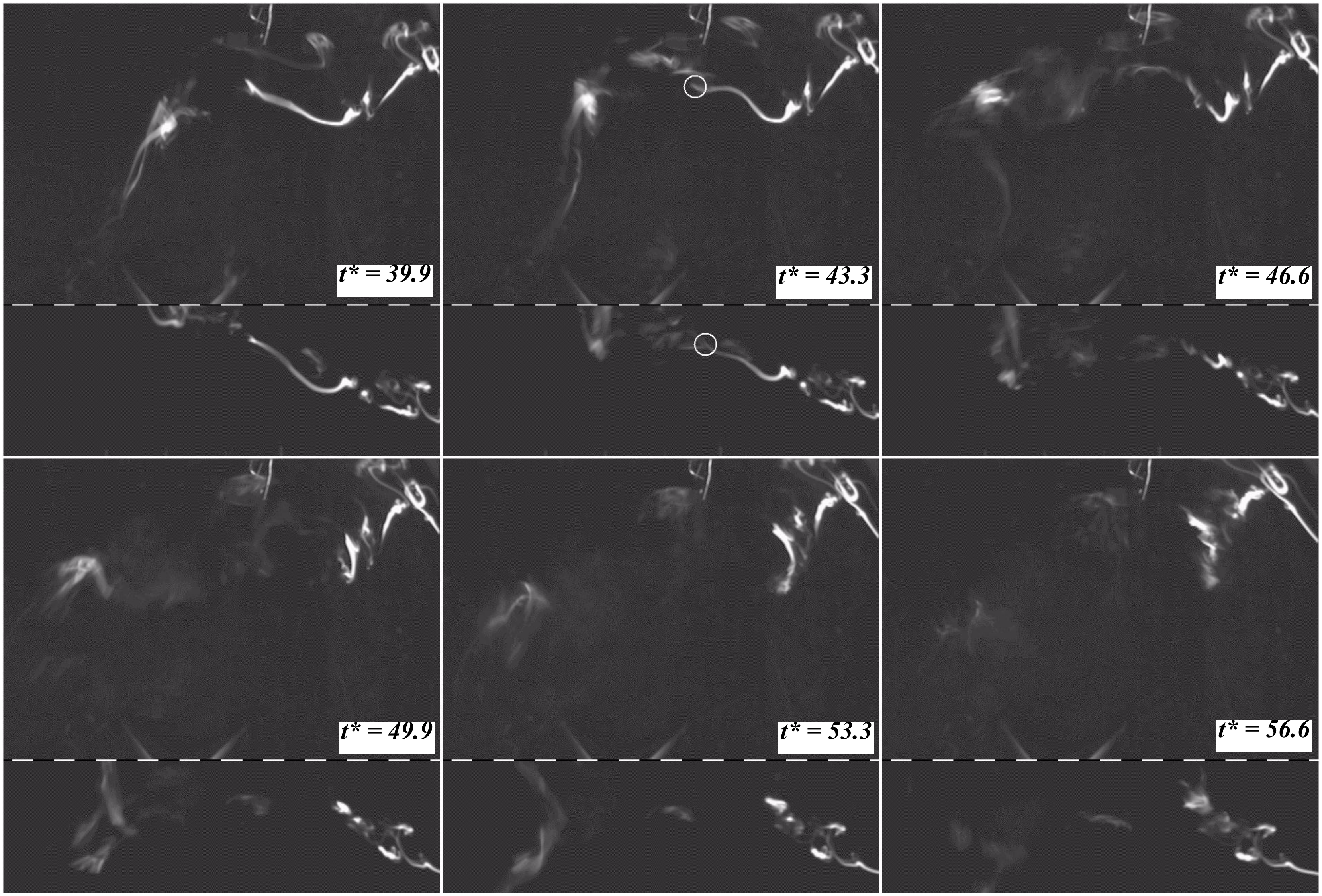
t* = 39.9
t* = 43.3
t* = 46.6
t* = 49.9
t* = 53.3
t* = 56.6

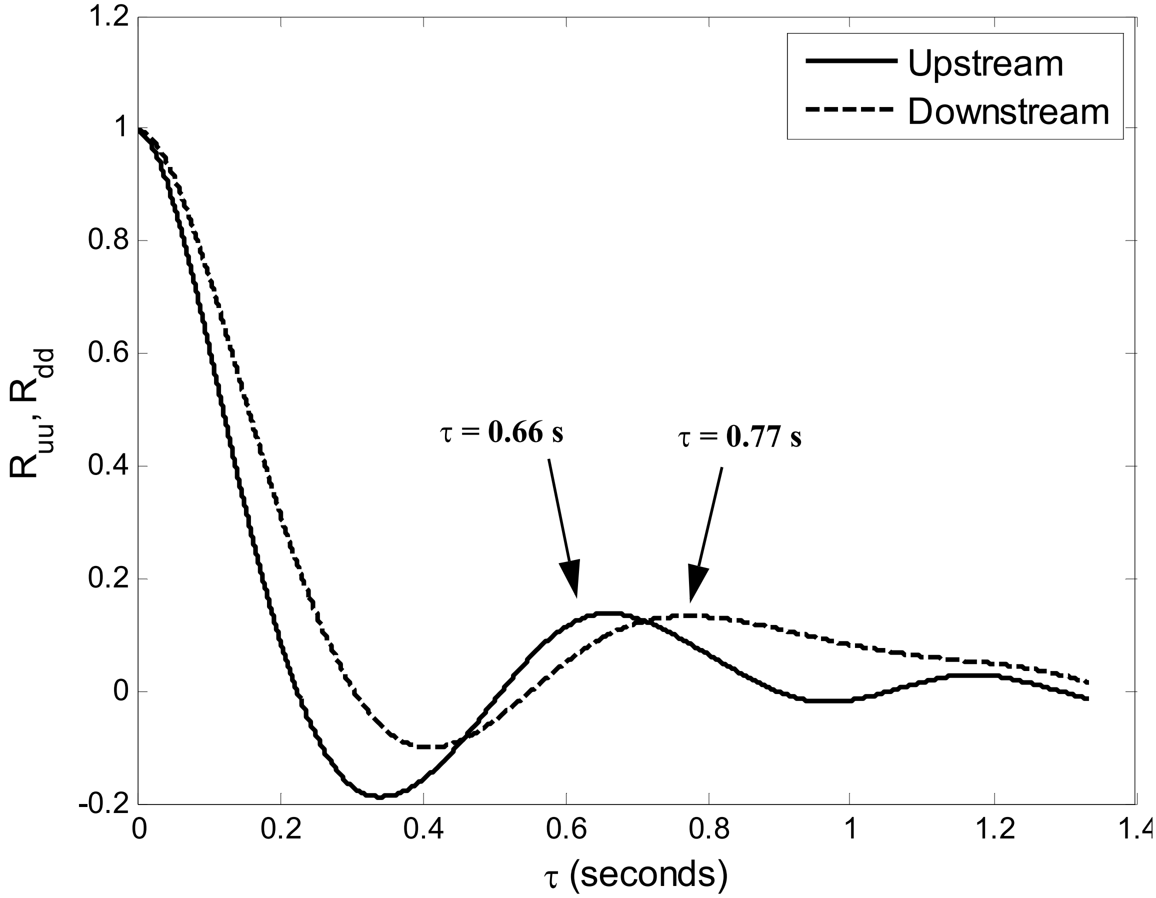

Figure 3.10 Autocorrelations of fluctuating voltage from upstream and downstream reference sensors.

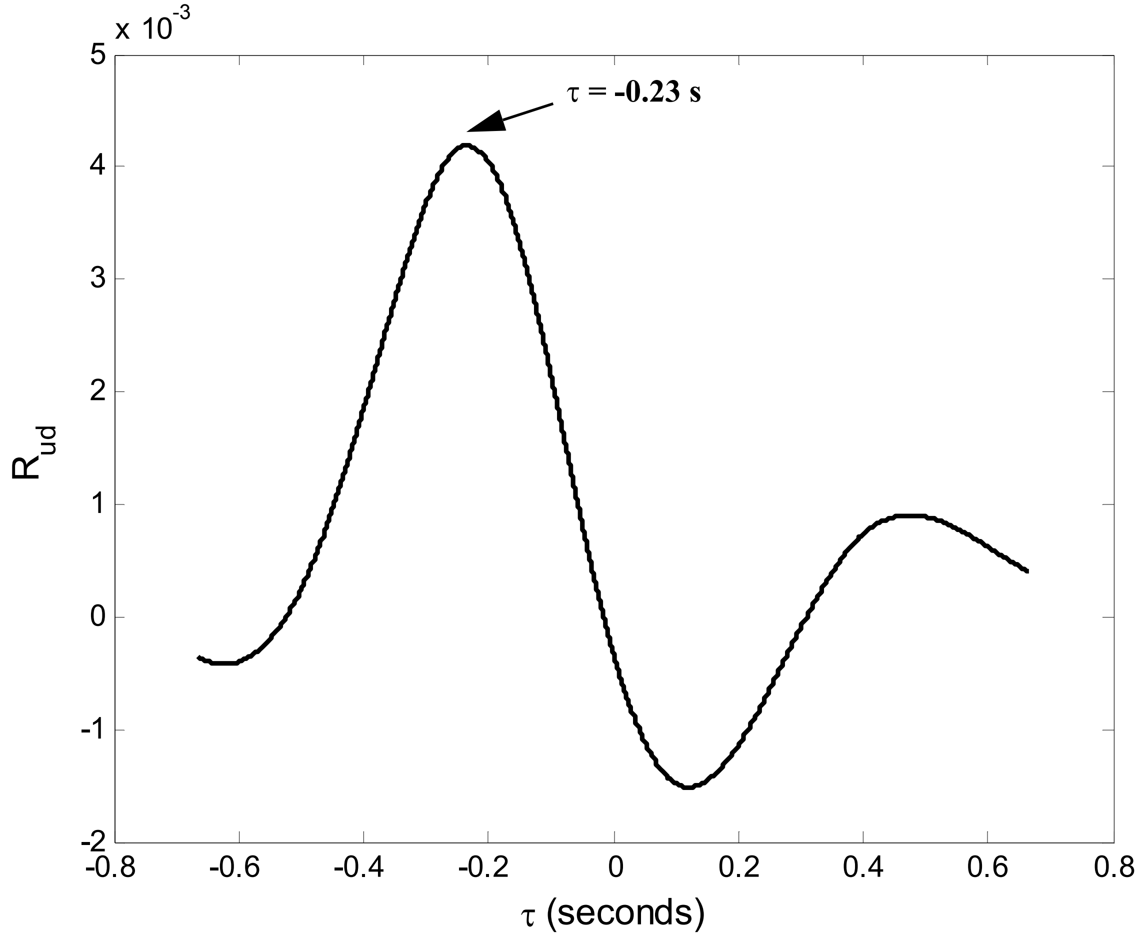

Figure 3.11 Cross-correlation of fluctuating voltages from upstream and downstream reference sensors.

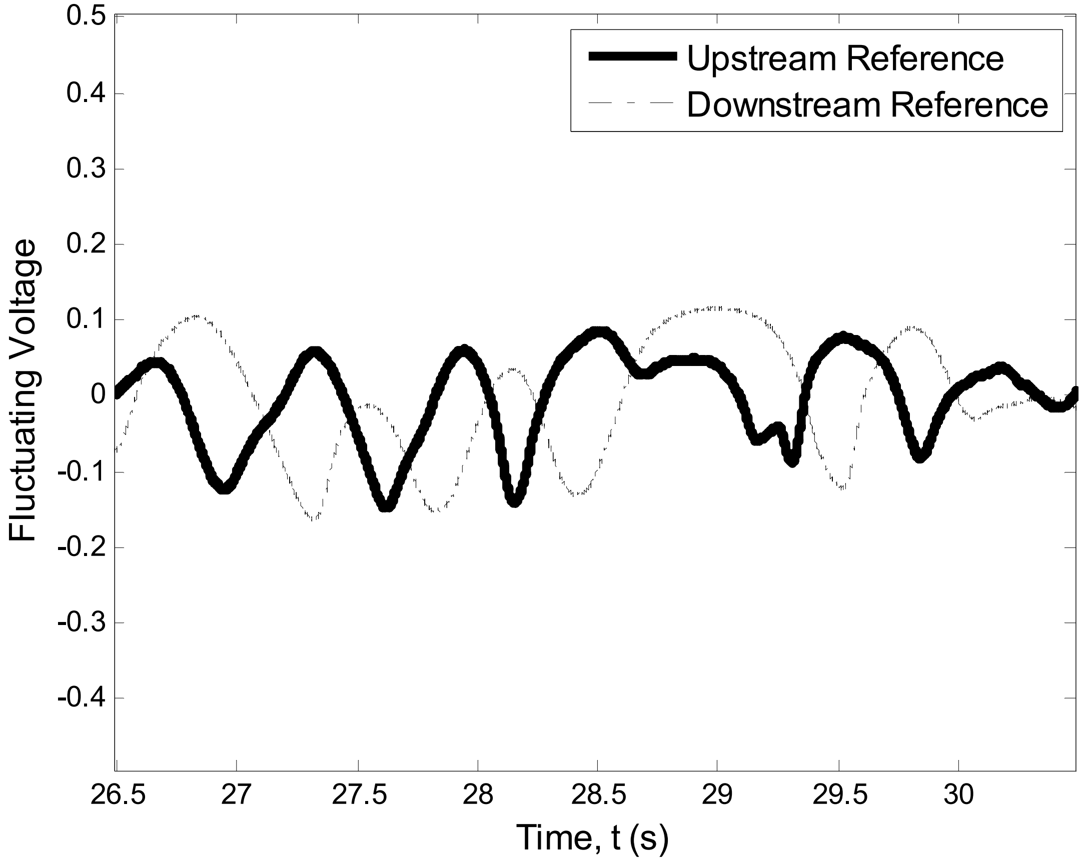

Figure 3.12 Fluctuating components of reference sensor signals.

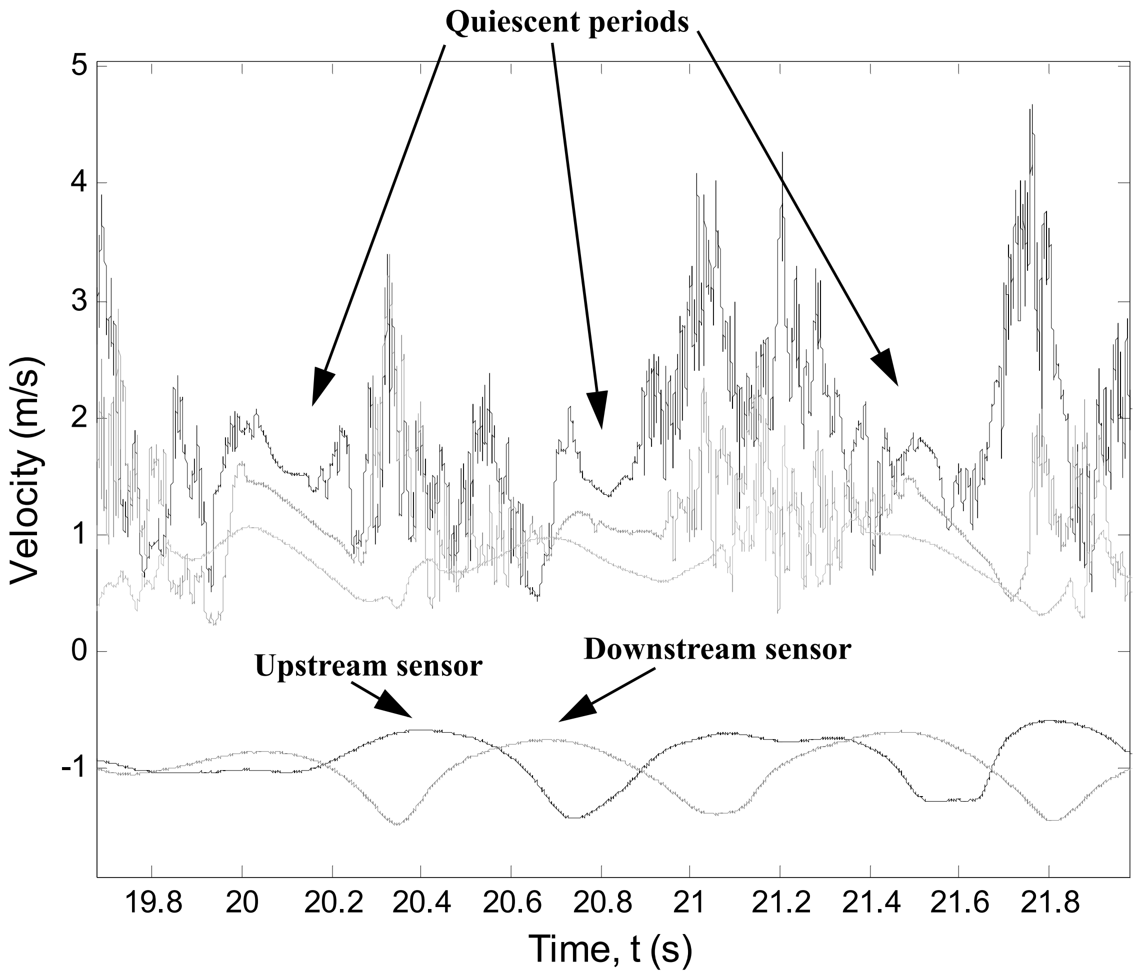

Figure 3.13 Portion of hot-wire time series demonstrating recognizable, somewhat repeating large-scale pattern. Note: The top three curves represent the velocity magnitudes measured by the calibrated rake wires, while the bottom two curves are simply the concurrent raw voltages of the reference wires, scaled and vertically offset.

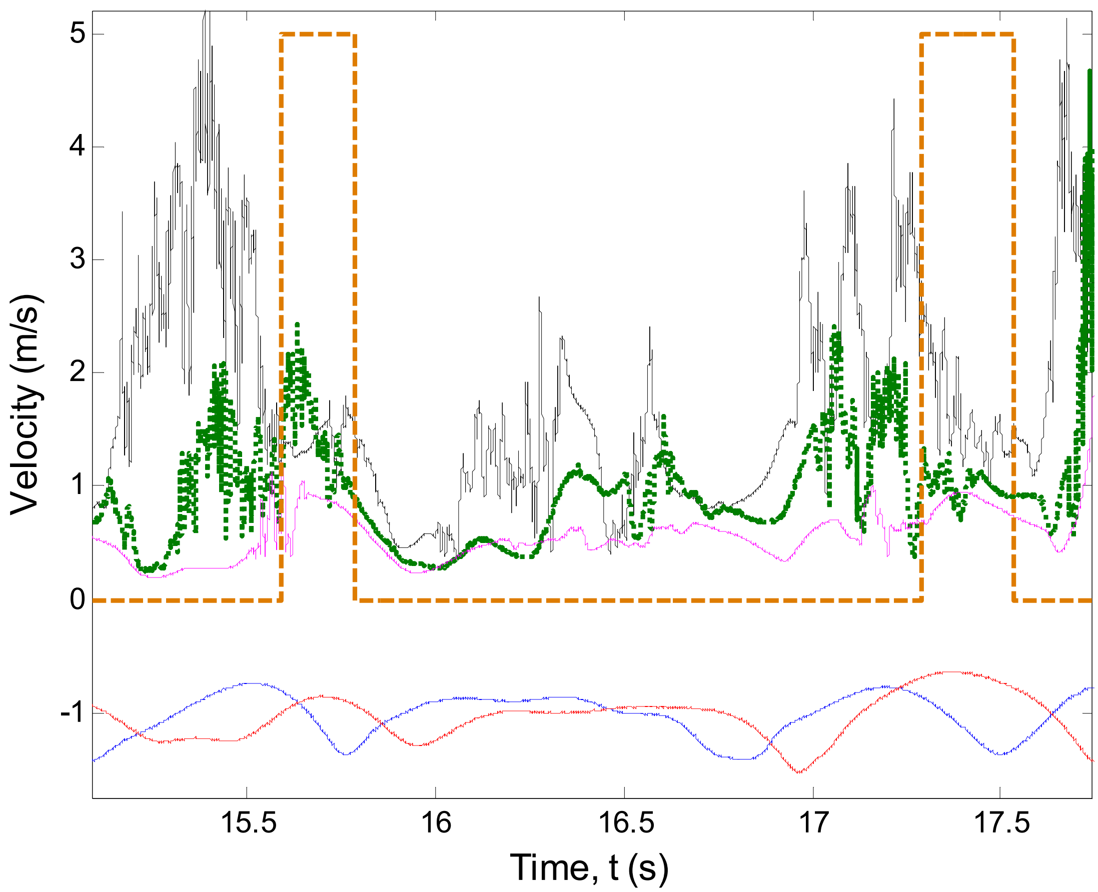

Figure 3.14 Portion of hot-wire time series showing wedge passage events inferred using the rake time series

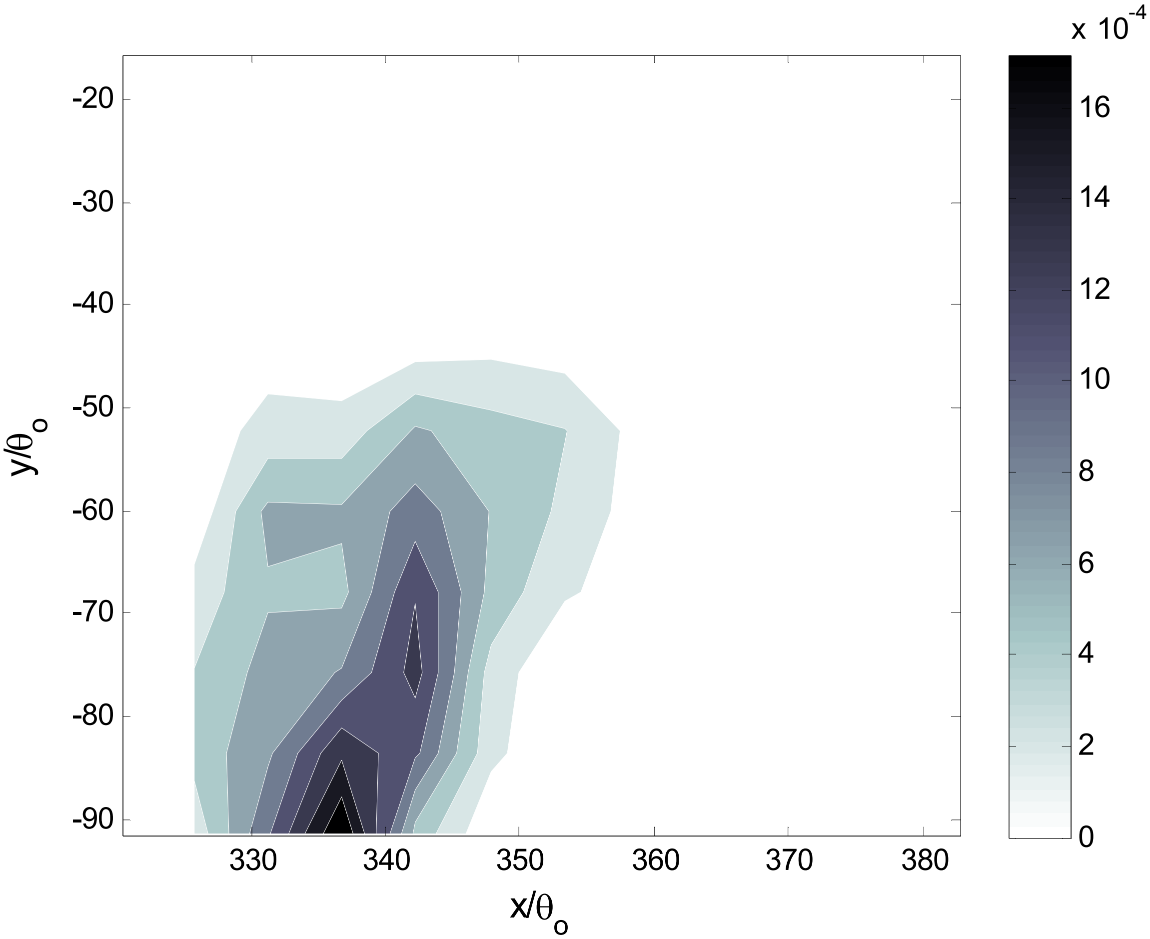

Figure 3.15 Joint PDF of plume x and y-positions. Note that incense coordinates are: $x/\theta_o = 335.1$, $y/\theta_o = -133.5$.

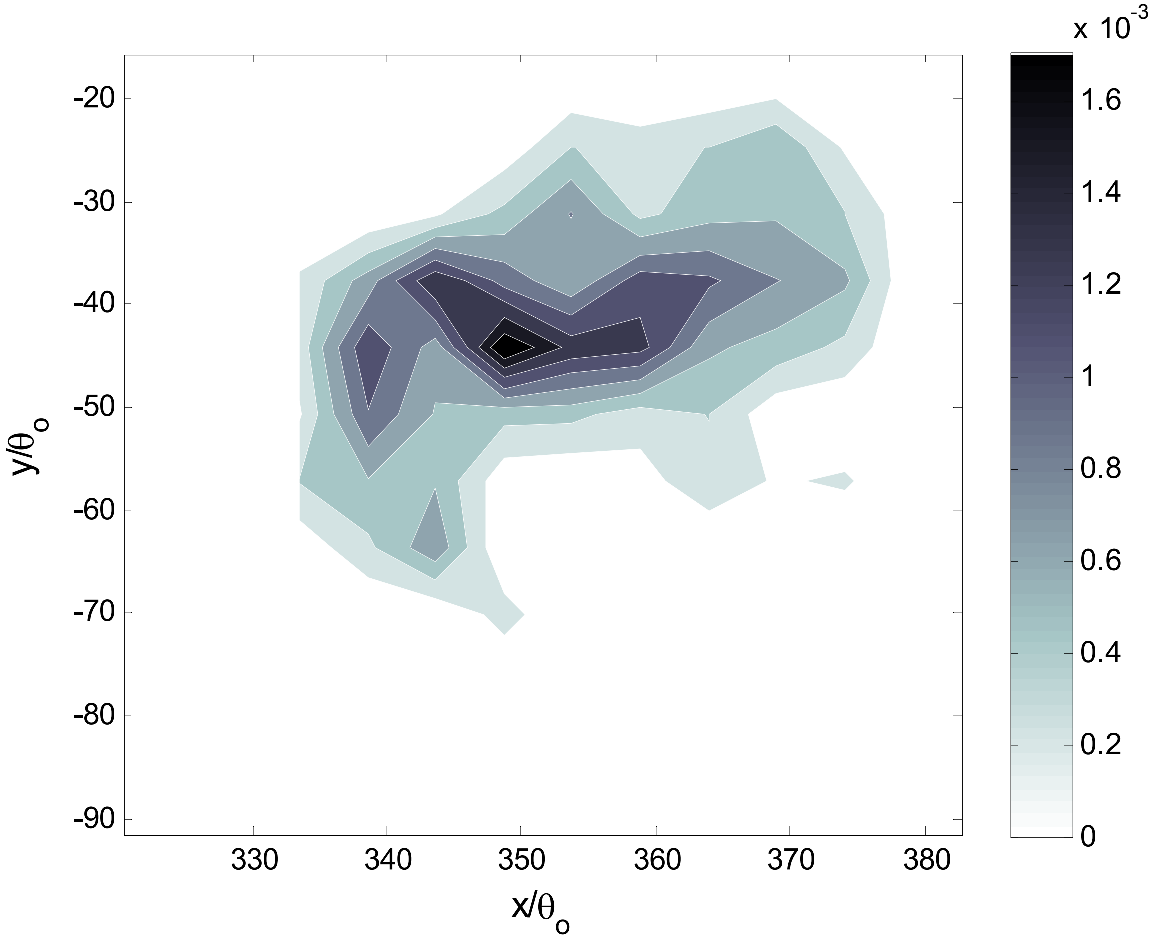

Figure 3.16 Joint PDF of VSL (streakline terminus) x and y-positions.

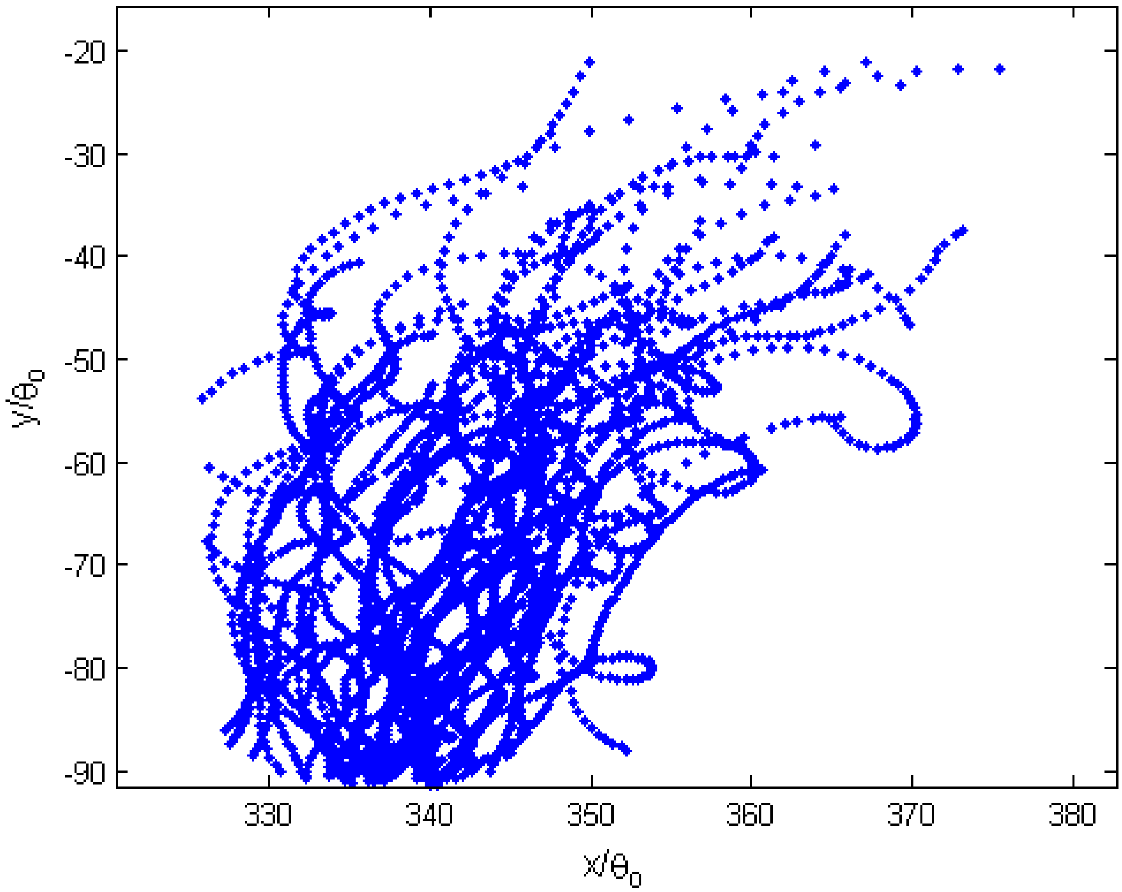

Figure 3.17 Scatter plot of plume locations.

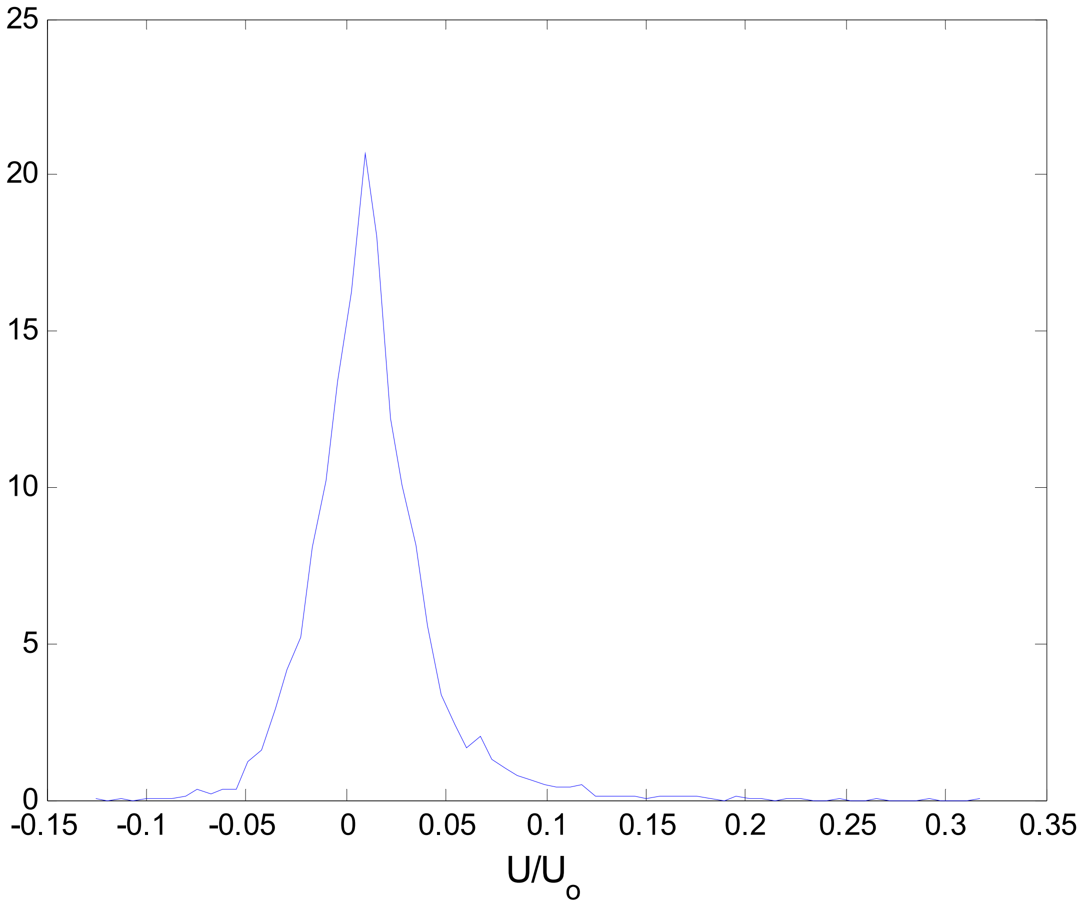

Figure 3.18 PDF of U from streakline plumes.

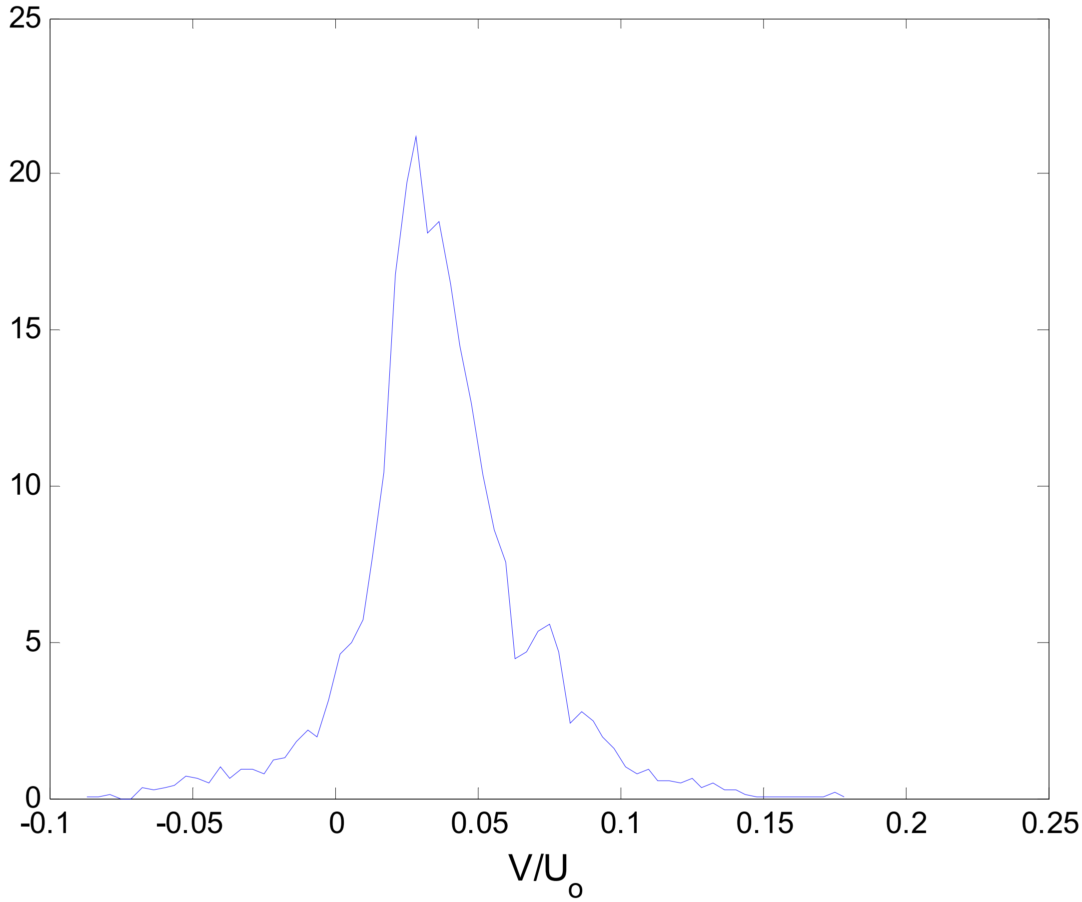

Figure 3.19 PDF of V from streakline plumes

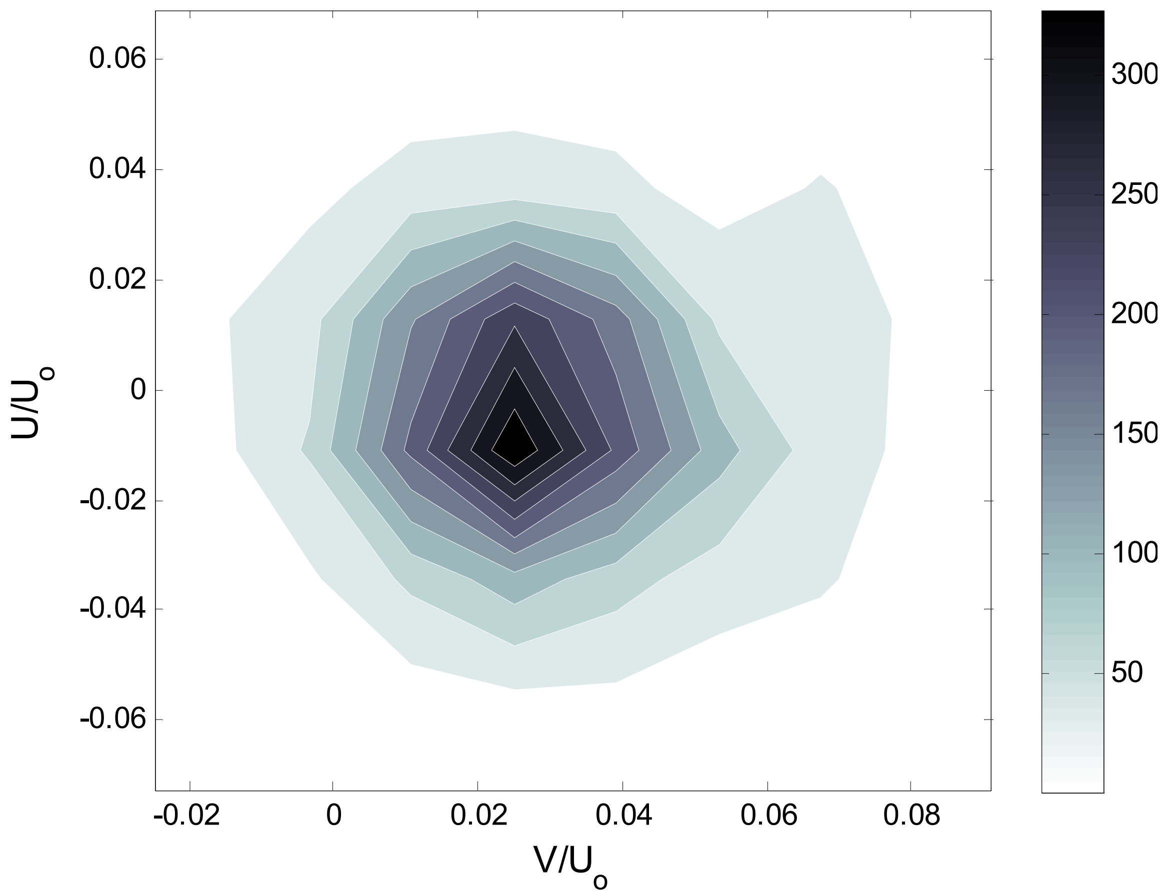

Figure 3.20 Joint PDF of U and V velocity components from streakline plumes.

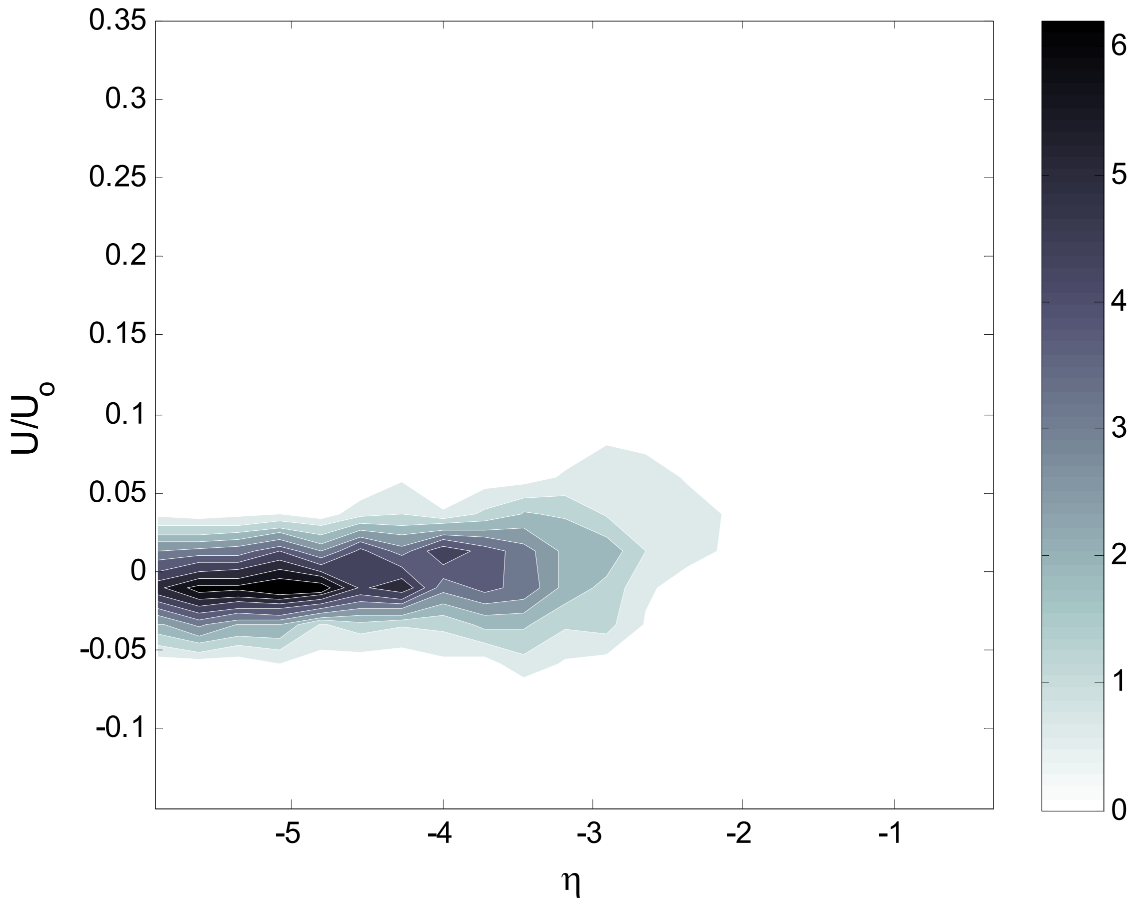

Figure 3.21 Joint PDF of U and η from streakline plumes.

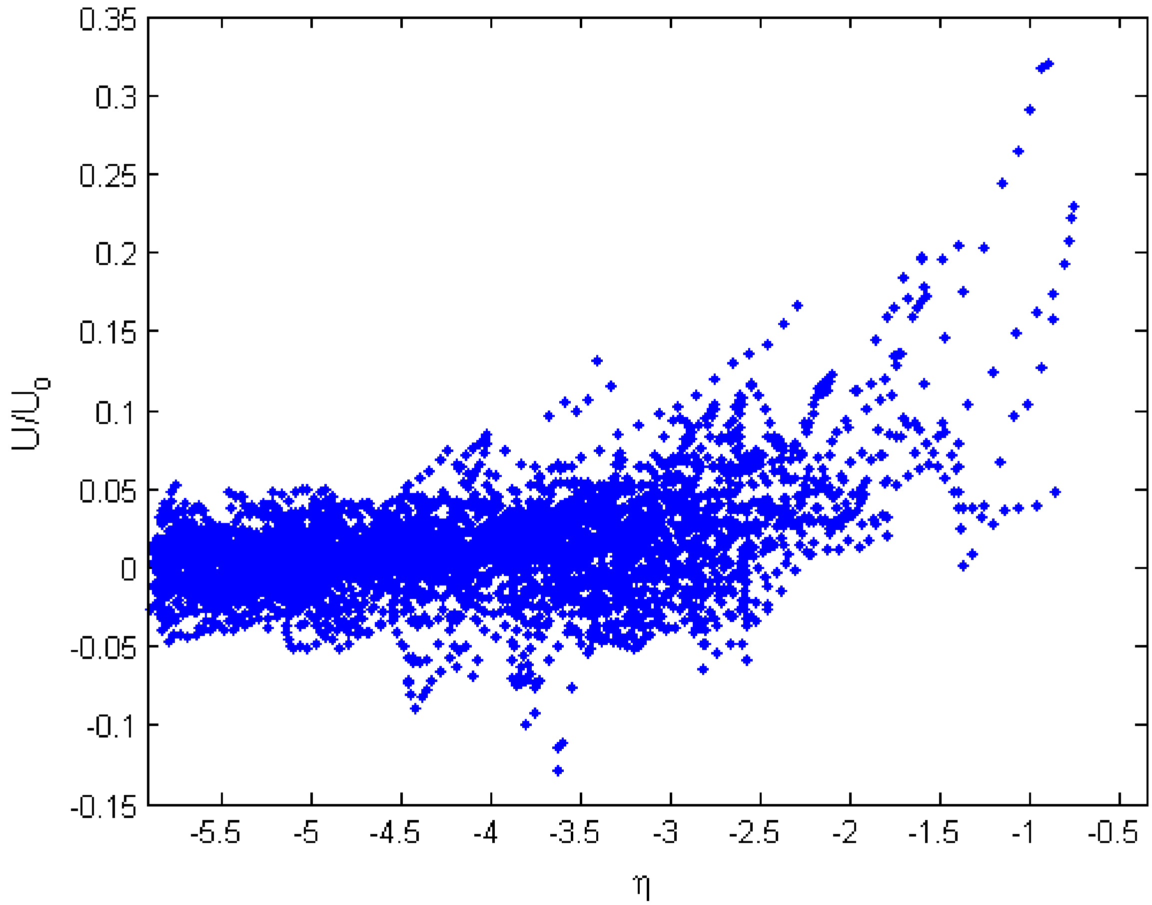

Figure 3.22 Scatter plot of U versus η from streakline plumes.

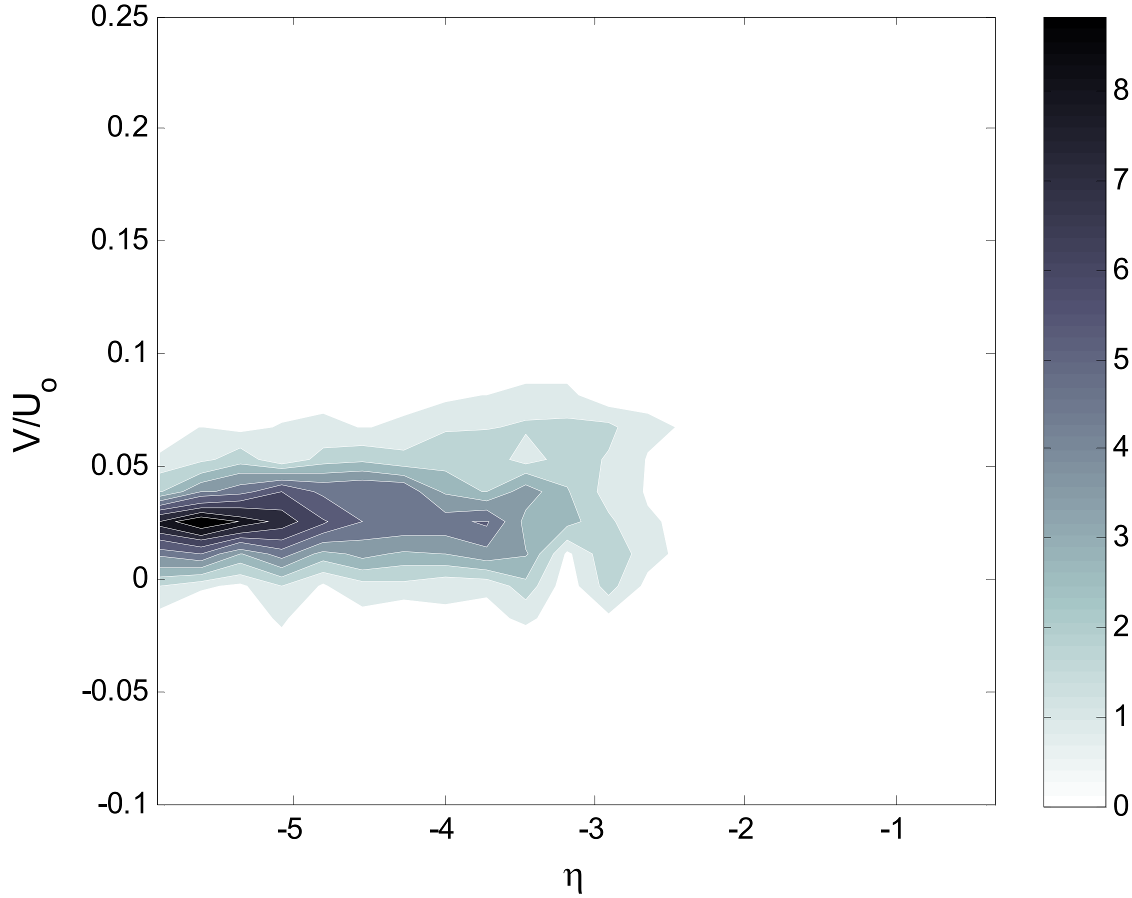

Figure 3.23 Joint PDF of V and η from streakline plumes.

4.0 Summary and Conclusions

A method for identifying the instantaneous position of the VSL on the low-speed side of a single stream shear layer using camera images of a smoke streakline was developed. 492 observations of the VSL location were obtained. Tracking of plumes along the streakline allowed for velocity statistics within the irrotational fluid to be recovered. Concurrently with these data, hot-wire time series were acquired at the edge and in the interior of the active shear layer. The extent to which fluid originating in the primary stream was transported towards the low-speed irrotational fluid was inferred by using a laser to illuminate the marked primary fluid in a series of camera images. The population of VSL locations lay unmistakeably closer to the active shear layer than the population of primary fluid extents, which was unexpected. This apparent bias could be explained in terms of assumed large-scale features of the VSL such as were described analytically by Phillips (1972). The description by Phillips assumed some inital contortion of the VSL by large vortical motions, such as those emphasized by Roshko (1976) and in subsequent research on turbulent shear layers.

The following conclusions are supported by the results of this study:

1) The intermittency factor measured on the high speed side, using the techniques of Hellum and Foss (2007), was found to be in good agreement with their results. Comparison was also made with the re-scaled data of Wygnanski and Fiedler (1970). A Gaussian distribution fit to the present data had a similar standard deviation to theirs, but a different mean value.

2) The histogram of VSL locations that were obtained from the streakline observations appears substantially non-Gaussian.

3) Fluid originating in the primary flow appeared to be transported farther into the entrainment region than the vorticity itself, with the exception of a short “tail” ($\eta \leq -4.5$). This apparent anomaly was resolved by further considerations. These are:

3a) The streakline terminus appears to follow regions of non-vortical fluid (termed wedges after Phillips) as they are ingested into the shear layer and convected downstream. This results in the terminus being preferentially observed within these wedges, which are characterized by relatively high values of η_{VSL}.

3b) The population of VSL locations that would be obtained by taking observations at a fixed streamwise location is a fundamentally different statistical quantity from the population that was obtained using the method in this communication. The streakline observations do not provide a population of η_{VSL} for a fixed streamwise location, but rather a population of η_{VSL} for the locus of material points that pass through the fixed location of the incense stick.

4) The Strouhal numbers of 0.027 and 0.028, based on the frequency of the large-scale motions that was inferred from the auto-correlation functions at $x/\theta_o = 306.6$ and $x/\theta_o = 382.7$, were found to be in reasonably good agreement with the value of 0.024 obtained in the fully-turbulent single

stream shear layer of Hussain and Zaman (1985) and the value of 0.026 obtained by Morris (2002). This provides an indication that the large scale features of the flow in the present study are similar to theirs.

5) Wedges can be identified in the hot-wire time series, and a correlation can be observed between these regions in the time series and observable "ingestion" events in the image series.

6) That the streakline follows the wedges downstream is additionally supported by the plume trajectories in the non-vortical fluid, which show evidence of substantial streamwise acceleration (to velocities as high as $0.35 U_o$) as fluid is brought deep within the active shear layer.

7) The accuracy of the velocity information recovered from tracking of the plumes is supported by the good agreement between the values: $V_e / U_o = 0.035$ as measured with hot-wires and $\langle V \rangle / U_o = 0.037$ as measured by tracking the plumes.

Appendix A : Two-Parameter Minimization to Determine Closest Points-of-Passage of Two Lines in 3-D Space

The closest points of passage of two lines in space can be determined by solving a two-parameter minimization problem. Consider a pair of equations which jointly describe a line in space:

$$x(z) = Az + B \qquad y(z) = Cz + D \tag{A.1}$$

The line described is parallel to the vector $\vec{Q} = A\,\hat{\mathbf{i}} + C\,\hat{\mathbf{j}} + 1\,\hat{\mathbf{k}}$ and also contains the point with position vector $\vec{Q}_O = B\,\hat{\mathbf{i}} + D\,\hat{\mathbf{j}} + 0\,\hat{\mathbf{k}}$. Points on this line may thus be represented by the parameter s in the following vector equation:

$$\vec{L}_1(s) = \vec{Q}s + \vec{Q}_O. \tag{A.2}$$

It is instructive to note that the form of Equations A.1 is the same that is used to describe the line associated with some chosen location in the camera image in the plane perpendicular to $\hat{\mathbf{k}}$. See Section 2.4.3 and Figure 2.27.

Another line in space might be described by:

$$y(x) = Ex + F \qquad z(x) = Gx + H \;. \tag{A.3}$$

Points on this line can be represented by the parameter t in the following vector equation:

$$\vec{L}_2(t) = \vec{R}t + \vec{R}_O, \tag{A.4}$$

where $\vec{R} = 1\,\hat{\mathbf{i}} + E\,\hat{\mathbf{j}} + G\,\hat{\mathbf{k}}$ and $\vec{R}_O = 0\,\hat{\mathbf{i}} + F\,\hat{\mathbf{j}} + H\,\hat{\mathbf{k}}$. Note also that the form of Equations A.3 is the same that is used to describe the line associated with some chosen location in the camera image in the plane perpendicular to $\hat{\mathbf{i}}$. See Section 2.4.3 and Figure 2.28.

The squared distance from a point on one line to a point on the other can be expressed as a function of s and t:

$$d^2 = \left|\vec{L}_1(s) - \vec{L}_2(t)\right|^2 = [\vec{L}_1(s) - \vec{L}_2(t)] \bullet [\vec{L}_1(s) - \vec{L}_2(t)]. \qquad \textbf{A.5}$$

Equation A.5 can be expanded and re-grouped as:

$$\begin{aligned} d^2 = {} & \left|\vec{R}\right|^2 t^2 + 2(\vec{R} \bullet \vec{R}_o - \vec{R} \bullet \vec{Q}_o)t - 2(\vec{R} \bullet \vec{Q})st + \\ & 2(\vec{Q} \bullet \vec{Q}_o - \vec{Q} \bullet \vec{R}_o)s + \left|\vec{Q}\right|^2 s^2 + \left|\vec{R}_o\right|^2 + \left|\vec{Q}_o\right|^2 \end{aligned}. \qquad \textbf{A.6}$$

Since the vectors $\vec{Q}$, $\vec{Q}_o$, $\vec{R}$ and $\vec{R}_o$ are known, Equation A.6 is a quadratic function of s and t. The minimum value of d^2 and the corresponding values of s and t are easily determined from calculus. The values of s and t are inserted into Equations A.2 and A.4 to return the spatial coordinates of the lines' closest points-of-passage.

Appendix B : Parasitic Effects in the Four-Sensor Vorticity Probe

The following discussion will make use of the coordinate system depicted in Figure 2.9 relative to the probe.

B.1 X-Array

As discussed in Section 2.3.2.1, the x-array is calibrated to provide $Q \equiv \sqrt{U^2 + V^2}$ and $\gamma \equiv \mathrm{atan}(V/U)$ in an environment where W, the z-direction velocity component, equals zero. If the fluid velocity vector assumes a non-zero value of W during the measurement, then the value of Q will be over-predicted by the array.

This can be explained as follows: Given a velocity vector with fixed components U and V, the rate of convective heat transfer from one of the inclined wires will always be greater if $W \neq 0$ than if $W = 0$. The wire will thus exhibit a higher bridge voltage, E, for the case where $W \neq 0$, even though $Q \equiv \sqrt{U^2 + V^2}$ is the same for the two cases. The bridge voltage is calibrated in an environment where W is nominally equal to zero, so that for a measurement condition where $W \neq 0$ the velocity values that are used to form $Q(\gamma)$ for each wire will be erroneously high. Therefore, the final predicted value of Q will be erroneously high as well. This has been noted already by Foss and Haw (1990).

This was observed by calibrating the x-array of a four-sensor vorticity probe in the usual manner, as described in Section 2.3.2. Note that in this orientation, the probe experiences $W = 0$ and the angle adjustment of the calibration facility provides $\gamma \neq 0$. After calibration, the probe body was rotated $90°$ about its axis (the x-axis). In this new orientation, the probe experiences $V = \gamma = 0$ and the angle adjustment of the calibration facility provides $W \neq 0$. Time series data were then acquired for $\phi \equiv \operatorname{atan}\left(\frac{W}{Q}\right) = -36°$, $-18°$, $0°$ and $+18°$ as the flow velocity was "spun-down" over a period of roughly 60 seconds. Q and γ were evaluated using the measured voltages from the x-array wires in this new configuration and compared with the known conditions of the calibration facility: $Q = V_B \cos\phi$ and $\gamma = 0$. Recall that V_B is the "Bernoulli velocity" obtained from the measurement of Δp across the nozzle.

The time series of Q_x are shown in Figure B.1. As expected, Q_x is in excellent agreement with the actual value, $Q = V_B \cos\phi$, for the case where $\phi = \gamma = 0$. However Q_x is substantially higher than the actual value of Q for both positive and negative values of ϕ. Additionally, though it is not shown, Q_x was found to be higher than even the total velocity magnitude, V_B, for $\phi \neq 0$.

It is instructive to observe the time series data that were obtained in the shear layer facility. Figure B.2 shows a portion of the concurrent time series of Q_x, Q_1 and Q_2. It can be seen that the values of Q_1 and Q_2 remain relatively close to one another over the portion of the record that is displayed. This is expected, given the straight wires' close proximity ($\Delta y \approx 1$ mm) to one another. Note that a straight wire will measure, albeit roughly, the velocity component normal to its sensor axis. Since the straight wires are oriented with their sensor axes parallel to the z-direction, they are roughly insensitive to this velocity component and their measured velocity may be regarded as approximately equal to Q. Substantially higher values are indicated for Q_x for $t < 4.3$ s, which is unexpected as the x-array is located nominally in-between the two straight wires. This pattern is consistently observable over the entire time record, that is to say, Q_1 and Q_2 remain relatively close to one another while Q_x is never substantially less and often substantially greater.

This has an observable effect on the measured mean velocity profile, which is shown in Figure B.3. The time-mean values of Q_x are greater than the time-mean values of Q_1 and Q_2 in the interior of the shear layer, where the greater frequency and intensity of the velocity fluctuations can be expected to increase the influence of non-zero values of W on the x-array. For this reason, quantities such as the momentum thickness, θ and the location of $y_{1/2}$ were calculated using the mean velocity information from the straight wires.

The effect of non-zero values of W on the predicted value of γ is not as easily explained. The time series of γ as evaluated using the voltages from the x-array with $\phi = -36°$, $-18°$, $0°$ and $+18°$ are shown in Figure B.4. Recall that for these measurements, γ is known to equal 0 in the flow facility. For $\phi = 0$, the measured values of γ are close to this known condition. However, this is not the case for $\phi \neq 0$. With γ known to be 0, the two inclined wires should see similar increases in their cooling rates for a given value of W. It might be expected, then, that the erroneously-high values of $Q(\gamma)$ provided by each wire would still find an intersection, (Q_x, γ) somewhat close to the

$\gamma = 0$ condition. It is noteworthy that this is not found to be the case. The influence of $W \neq 0$ for the condition: $\gamma \neq 0$ was not investigated.

B.2 Straight Wires

The time series of spanwise vorticity, ω_z has been observed to assume substantially non-zero values in regions which nonetheless exhibit little of the high-frequency content expected within the vortical fluid; see Figure B.5. This "inactive" but apparently vortical fluid was first observed by Haw et. al (1989), but has also been observed by Hellum (2006) and others using this probe design. This behavior has prompted the "activity intermittency" designation described in Section 2.3.4, since it seems to preclude a simple magnitude-based intermittency designation. A suitable explanation for this behavior has not heretofore been advanced. Here it is proposed that it represents, at least in part, a "parasitic effect" of non-zero values of W acting on the straight wires in the array.

An initial observation that can be made is that when the vorticity signal is separated into its so-called $\frac{\partial U}{\partial y}$ and $\frac{\partial V}{\partial x}$ terms (see page 24 for clarification of these quantities), the inactive-but-vortical fluid is observed only in the $\frac{\partial U}{\partial y}$ term; see Figure B.5. This can also be observed in Figure 3 of Haw et. al, although it is not noted by them. The $\frac{\partial U}{\partial y}$ term is formed from the difference in velocities indicated by the two straight wires, whereas the $\frac{\partial V}{\partial x}$ term is formed by averaging these velocity signals at the upstream and downstream ends of the micro-circulation domain and taking that difference. This suggests that the substantially non-zero values of the $\frac{\partial U}{\partial y}$ term may be related to a difference in the way that that the straight wires' sensitivities depend on the local flow field.

More specifically, consider a scenario for which the two straight wires are exposed to a uniform velocity field, with $(W \neq 0)$. Since their sensor axes are nominally parallel to the z-direction, the velocity component normal to the wires is nominally $Q \equiv \sqrt{U^2 + V^2}$. The velocities that are measured are the wires' "effective cooling velocities," and these will be approximately equal to this normal component, Q, as described above in Section B.1. Therefore, the measured velocities should both exhibit a similar cosine dependence on the angle, ϕ, between the velocity vector and the x-y plane. However, tangential cooling effects also play some role in determining the effective cooling velocity of a wire, and these effects are strongly dependent on the unique shape of the wire, which is seldom perfectly straight. Additionally, the sensor axes of the straight wires are only nominally parallel to the z-direction. They may independently deviate from this orientation by several degrees as a consequence of the difficulty associated with mounting the sensors.

For this reason, when $W \neq 0$, the voltages from the two straight wires may indicate slightly different velocities when the wires' calibrations are applied, even in a uniform velocity field. This will result in a non-zero value for the $\frac{\partial U}{\partial y}$ term, and a non-zero value for ω_z. Since the velocity difference is divided by the "small" value, Δy, in the $\frac{\delta U}{\delta y}$ term, a small velocity disagreement can result in the indication of a substantial vorticity magnitude.

To demonstrate this, a four-sensor vorticity probe was calibrated in the usual manner; see Section 2.3.2. The probe body was then rotated $90°$ about its axis in the calibration facility, as described earlier in Section B.1. Time series data were again acquired for $\phi = -36°, -18°, 0°$ and $+18°$ as the flow velocity was “spun-down” over a period of roughly 60 seconds. Q_1 and Q_2 were evaluated using the measured voltages from the straight wires in this new configuration and compared with the known conditions of the facility: $Q = V_B \cos\phi$.

It can be seen in Figure B.6 that for $\phi = 0$, the time series are indistinguishable from one another. However, it is apparent that for $\phi \neq 0$ there is some disagreement between the values. Specifically, Q_1 exhibits a much greater sensitivity to ϕ than Q_2, which agrees well with the actual value of Q for all values of ϕ. Note that the discrepancy between Q_1 and Q_2 is approximately 1 m/s for $\phi = -36°$. With a nominal wire separation, Δy, of 1 mm the indicated vorticity magnitude would be approximately 1000 s^{-1}. The inactive but non-zero values of vorticity encountered in the shear layer are typically on the order of several hundred s^{-1}, which is well within this value.

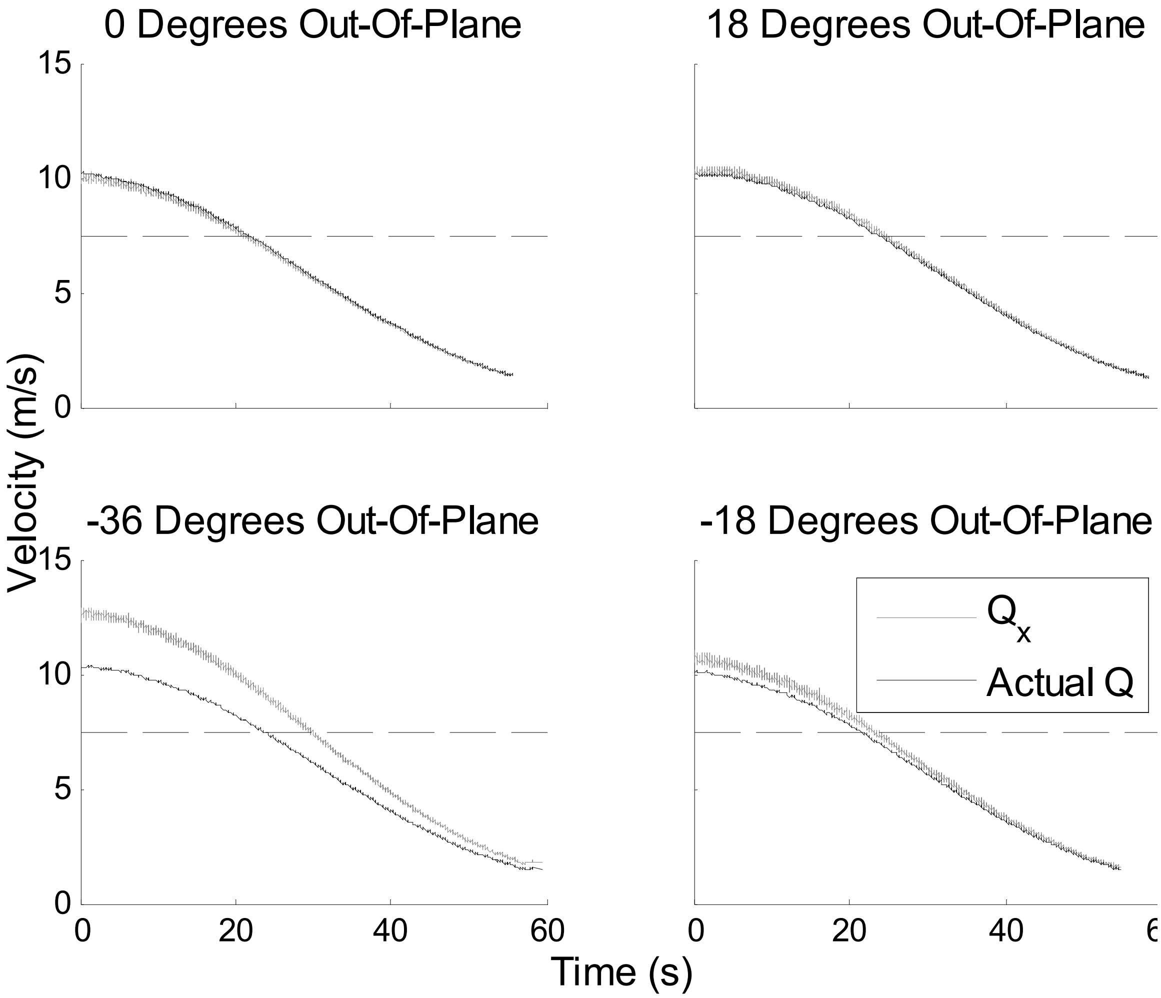

Figure B.1 "Spin-down" time series of x-y plane velocity, Q, as predicted by the x-array for various values of ϕ. Note: The "jitter" in the velocity magnitudes is intrinsic to the spin down method. Since these data are used to obtain calibration constants, the jitter is not important. The dashed lines indicate the value of $U_o = 7.5$ m/s used in the shear layer experiment.

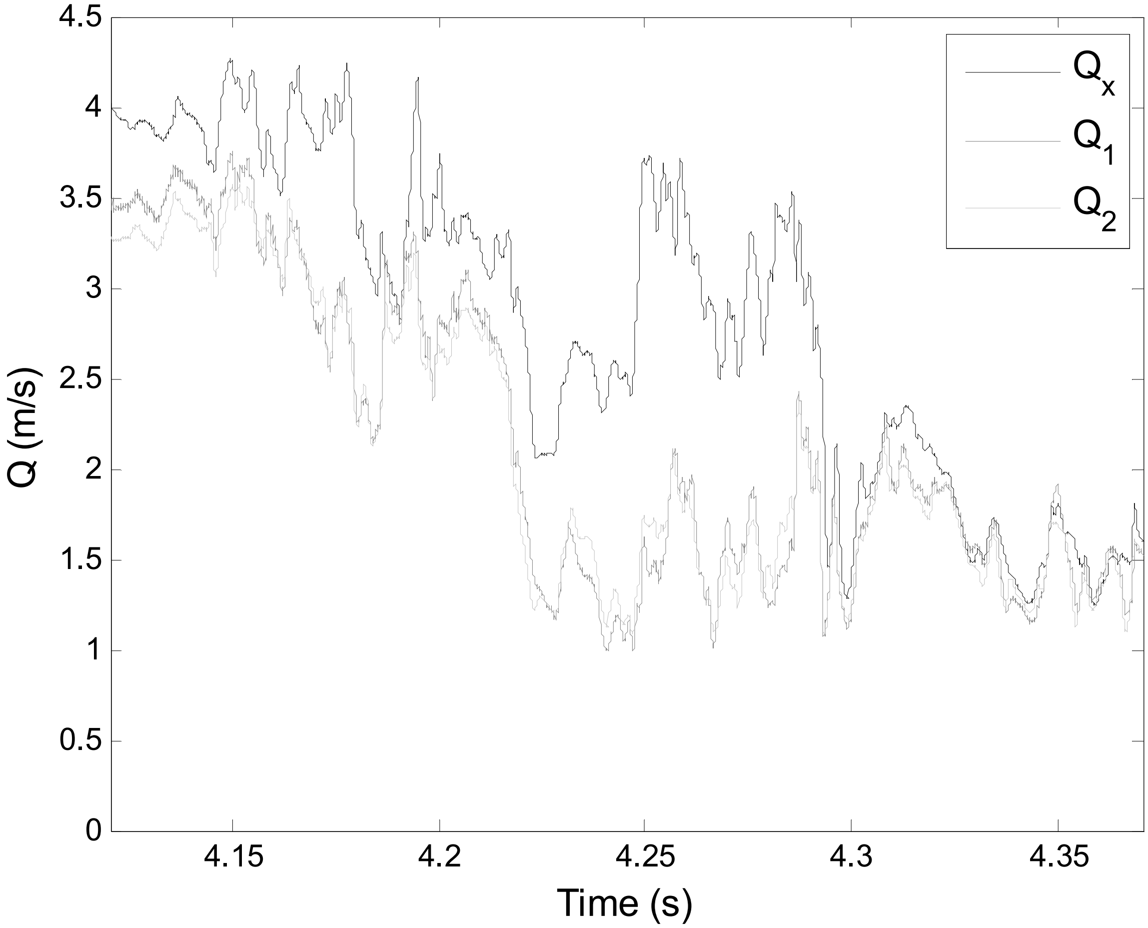

Figure B.2 Concurrent velocity time series measured in the shear layer at $\eta = -1.22$ using the x-array and the two straights. Note that over this portion of the time series, the mean values of Q_x and Q_1 are respectively 2.82 and 2.15 m/s, while their standard deviations are respectively 0.90 and 0.83 m/s.

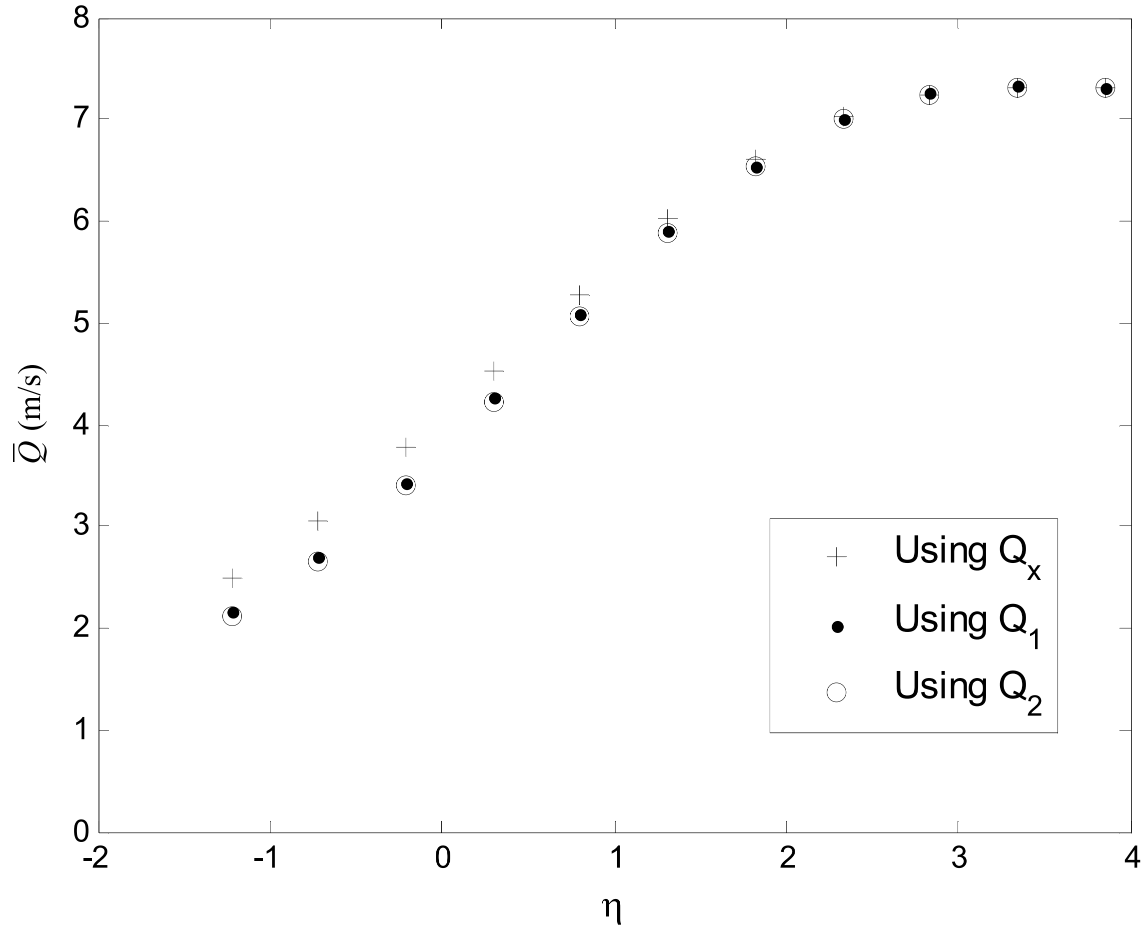

Figure B.3 Mean velocity profile in the SSSL facility as obtained using the x-array and the two straight wires.

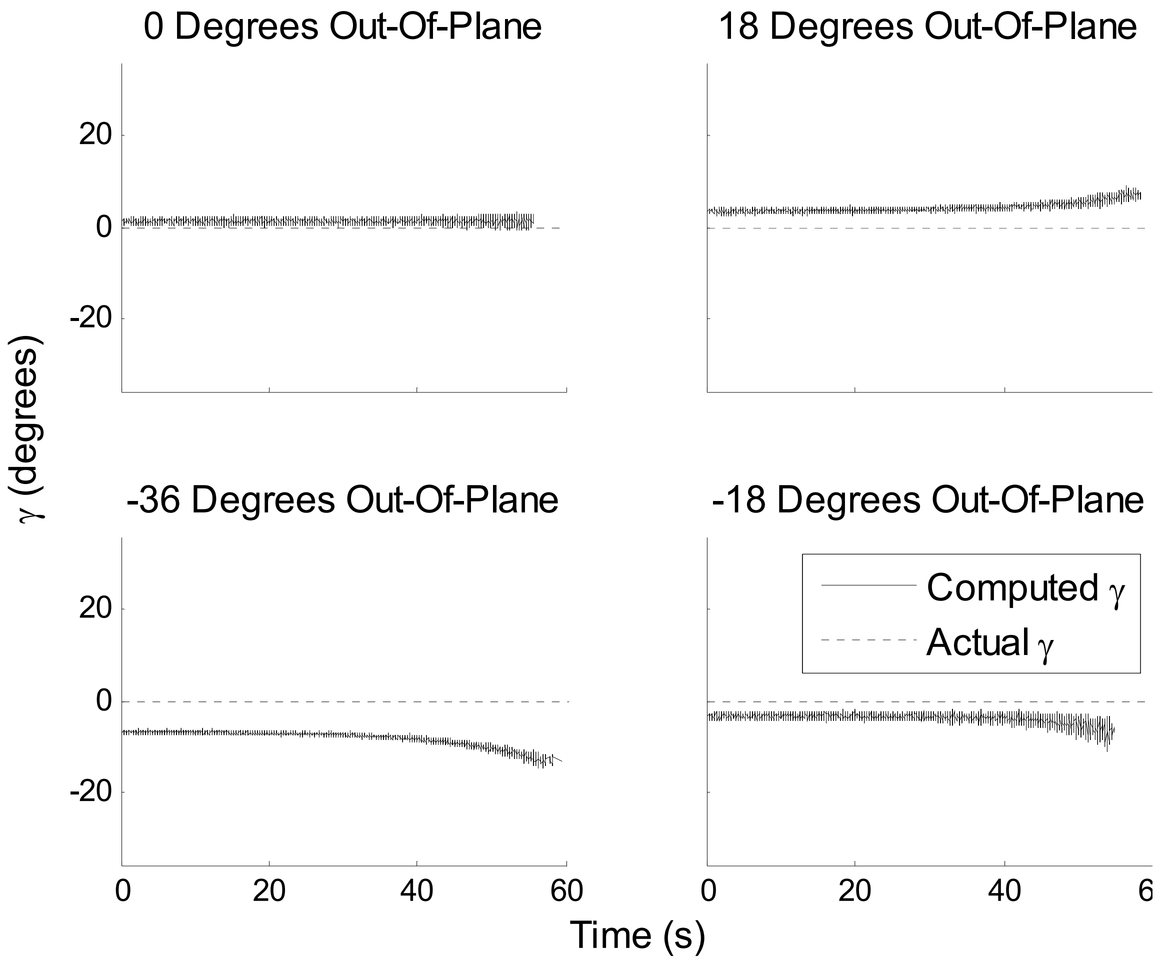

Figure B.4 "Spin-down" time series of x-y plane angle, γ, as predicted by the x-array for various values of ϕ. Note that the actual value of γ is zero for all cases.

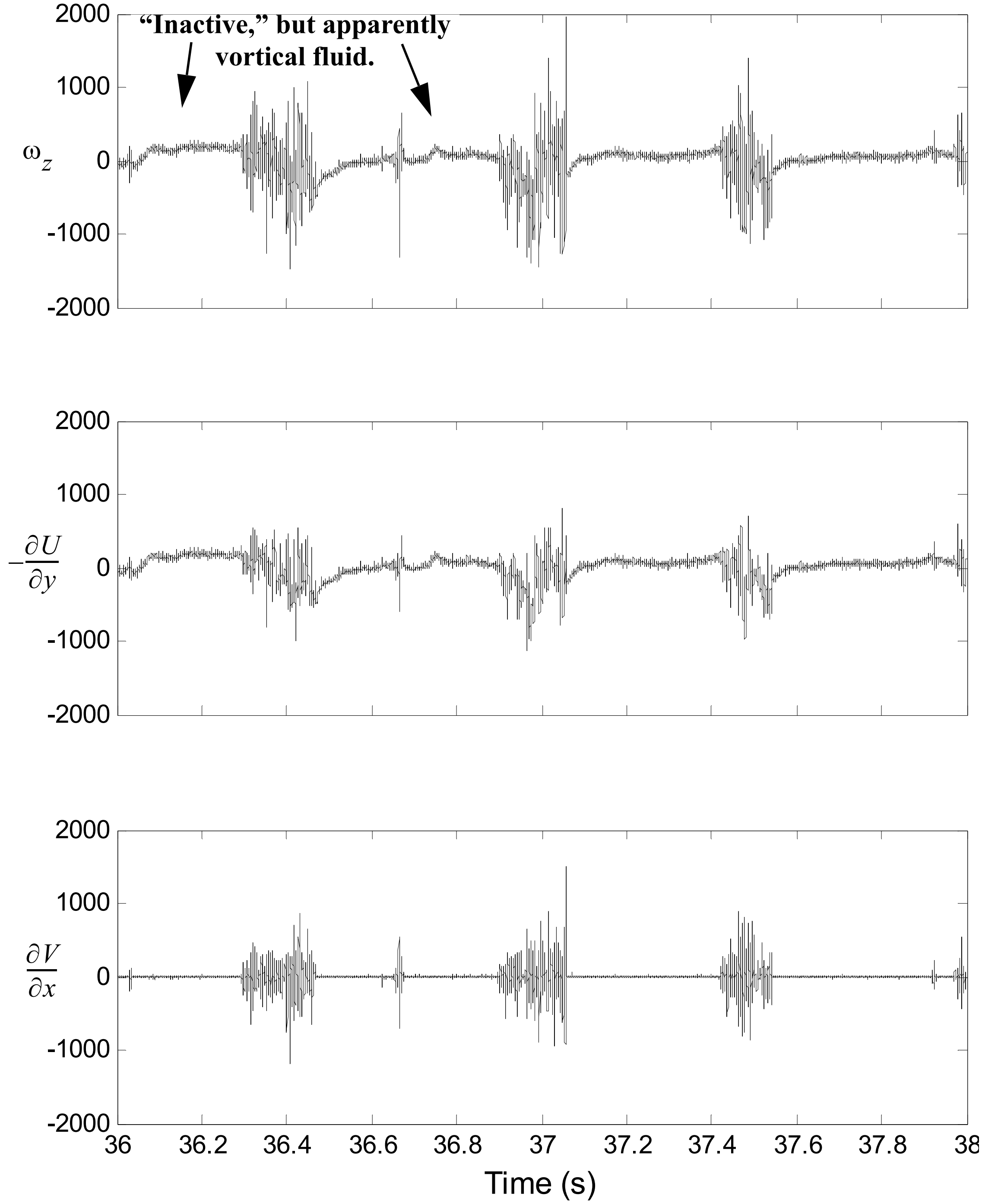

Figure B.5 Span-wise vorticity time series and its two contributing terms at $\eta = 2.33$. Note that the activity intermittency factor, $\overline{I}$, is equal to 0.36 at this location.

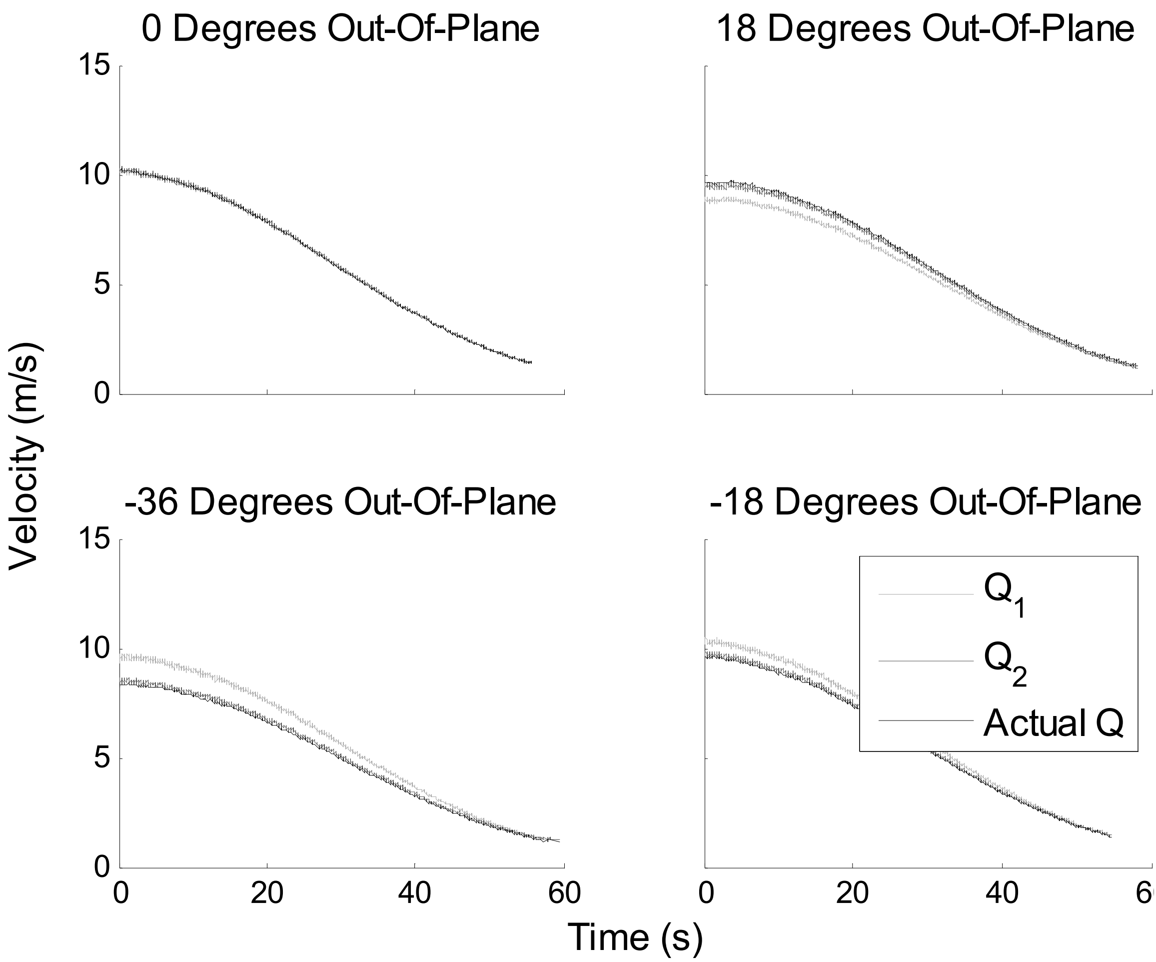

Figure B.6 “Spin-down” time series of x-y plane velocity, Q, as predicted by the straight wires for various values of ϕ. Note that the good agreement between Q_2 and the actual value makes them indistinguishable from one another.

REFERENCES

REFERENCES

1. Abdel Rahman, A., Tropea, C., Slawson, P. and Strong, A., (1987). "On Temperature Compensation in Hot-wire Anemometry", *Journal of Physics, E: Sci. Instrum.,* Vol 20, pp. 315-319.

2. Ali, S.K., Klewicki, C.L., Disimile, P.J., Lawson, I. and Foss, J.F. (1985). *Entrainment Region Phenomena in a Large Plane Shear Layer.* Fifth Symposium on Turbulent Shear Flows, Ithaca, NY, August 7-9, 1985, Proceedings (A86-30201 13-34). University Park, PA, Pennsylvania State University, pp. 3.7-3.12.

3. Bisset, D.K., Hunt, J.C.R., Rogers, M.M. (2002). "The Turbulent/Non-Turbulent Interface Bounding a Far Wake". *Journal of Fluid Mechanics,* Vol 451, pp. 383-410.

4. Browand, F.K. and Troutt, T.R. (1980). "A Note on Spanwise Structure in the Two-Dimensional Mixing Layer". *Journal of Fluid Mechanics,* Vol 917, pp. 771-781.

5. Brown, L.W.B., Antonia, R.A., and Chua, L.P. (1989). "Calibration of X-Probes for Turbulent Flow Measurement". *Experiments in Fluids,* Vol 7, pp. 201-208.

6. Champagne, F.H., Sleicher, C.A. and Wehrmann, O.H. (1967). "Turbulence Measurements With Inclined Hot-Wires". *Journal of Fluid Mechanics,* Vol 28, pp. 153-182.

7. Champagne, F.H., Pao, Y.H. and Wygnanski, I.J. (1976). "On the Two-Dimensional Mixing Region". *Journal of Fluid Mechanics,* Vol 74, pp. 209-250.

8. Collis, D.C. and Williams, M.J. (1959). "Two-Dimensional Convection From Heated Wires at Low Reynolds Number". *Journal of Fluid Mechanics,* Vol 6, pp. 357-384.

9. Corrsin, S. (1943). "Investigation of Flow in an Axially Symmetrical Heated Jet of Air". NACA WR W-94, NACA, Washington, D.C.

10. Corrsin, S., and Kistler, A.L. (1955). "Free-Stream Boundaries of Turbulent Flows". National Advisory Committee for Aeronautics, Report 1244.

11. Dimotakis, P.E. (1986). "Two-Dimensional Shear-Layer Entrainment". *AIAA Journal,* Vol 24, pp. 1791-1796.

12. Dimotakis, P.E. and Brown, G.L. (1976). "The Mixing Layer at High Reynolds Number: Large-Structure Dynamics and Entrainment." *Journal of Fluid Mechanics,* Vol 78 pp. 535-560.

13. Foss, J.F. and Haw, R.C. (1990). "Transverse Vorticity Measurements Using a Compact Array of Four Sensors". In The Heuristics of Thermal Anemometry, ed. DE Stock, SA Sherif, AJ Smits, ASME-FED 97: 71-76, pp 98.

14. Haw, R.C., Foss, J.K. and Foss, J.F. (1989). "Vorticity-Based Measurements in a Single-Stream Shear Layer". Advances in Turbulence 2, editors Fernholz, H.H. and Fiedler, H.E., Springer-Verlag Berlin.

15. Hellum, A. (2006). Intermittency and the Viscous Superlayer in a Single Stream Shear Layer. M.S. Thesis, Michigan State University.

16. Hellum, A. and Foss, J.F. (2007, August). *Effects of Flow Scale on the Intermittent Properties of a Single Stream Shear Layer.* Paper Presented at the Fifth International Symposium on Turbulence and Shear Flow Phenomena, Garching, Germany.

17. Holst, G.C. (1996). CCD Arrays, Cameras and Displays. JCD Publishing.

18. Hussain, A.K.M.F. and Zaman, K.B.M.Q. (1985). "An Experimental Study of Organized Motions in the Turbulent Plane Mixing Layer". *Journal of Fluid Mechanics,* Vol 159, pp. 85-104.

19. Koochesfahani, M.M., Catherasoo, C.J., Dimotakis, P.E., Gharib, M. and Lang, D.B. (1979). "Two-Point LDV Measurements in a Plane Mixing Layer". *AIAA Journal*, Vol 17, pp. 1347-1351.

20. Morris, S.C. (2002). The Velocity and Vorticity Fields of a Single Stream Shear Layer. Ph.D Thesis, Michigan State University.

21. Morris, S.C. and Foss, J.F. (2003a). "Turbulent Boundary Layer to Single Stream Shear Layer: The Transition Region". *Journal of Fluid Mechanics,* Vol 494, pp. 187-221.

22. Morris, S.C. and Foss, J.F. (2003b). "Transient Thermal Response of a Hot-Wire Anemometer". *Measurement Science and Technology,* Vol 14, pp. 251-259.

23. Phillips, O.M., (1955). "The Irrotational Motion Outside A Free Turbulent Boundary". *Mathematical Proceedings of the Cambridge Philosophical Society,* Vol 51, pp. 220-229 Cambridge University Press

24. Phillips, O.M., (1972). "The Entrainment Interface". *Journal of Fluid Mechanics,* Vol 51, pp. 97-128.

25. Roshko, A., (1976). "Structure of Turbulent Shear Flows: A New Look." *AIAA Journal*, Vol 14, pp. 1349-1357.

26. Wygnanski, I. and Fiedler, H.E., (1970). "The Two-Dimensional Mixing Region". *Journal of Fluid Mechanics,* Vol 41, pp. 327-361.